8^{th} Order Super-Structure Resonance driven by Space Charge

Dissertation

zur Erlangung des Doktorgrades

der Naturwissenschaften

vorgelegt beim Fachbereich Physik

der Johann Wolfgang Goethe-Universität

in Frankfurt am Main

von

Raymond Wasef

aus Alexandria, Ägypten

Frankfurt 2017

(D 30)

Vom Fachbereich Physik der

Johann Wolfgang Goethe-Universität als Dissertation angenommen.

Dekan:	Prof. Dr. Owe Philipsen
Gutachter:	PD. Dr. Giuliano Franchetti
	Prof. Dr. Ulrich Ratzinger
	Dr. Simone Gilardoni

Datum der Disputation:

Money may not buy happiness but it's better to cry in a Lamborghini...

Multiple Authors

Abstract

8^{th} Order Super-Structure Resonance driven by Space Charge

by Raymond WASEF

After the discovery of the Higgs boson, which completes the Standard Model, the research at CERN, The European Organization for Nuclear Research is now steered towards understanding the properties of the Higgs and simultaneously searching for new Physics beyond the frontiers of the currently known. Producing more data became a priority for CERN, therefore several projects were developed, targeting essentially the increase of the collision rate at the Large Hadron Collider (LHC). To achieve a higher collision rate, the accelerators should produce beams with higher brightness, which is limited particularly by the space charge in each of the LHC injector chain.

This thesis focuses on studing the space charge limitations in the CERN Proton Synchrotron (PS) and proposing solutions to the identified limitations.

In the first part of the thesis, the main space charge limitations are identified. The second part focuses on the limitation due the $Q_y = 6.25$ resonance line and its nature. In the third part, a mitigation to the $Q_y = 6.25$ resonance line is proposed, as well as mitigations to other observed limitations.

Contents

List of Figures

List of Tables

Zusammenfassung

0.1 Einleitung und Motivation

Eine höhere Luminosität wurde für den Large Hadron Collider (LHC) des CERN seit längerem gesucht und geplant [6]. Um die angestrebten Größenordnungen zu erreichen, müssen die jeweiligen Grenzen in der Strahlhelligkeit der einzelnen Maschinen der Injektorkette überwunden werden. Die Flaschenhälse sind hierbei, in Abhängigkeit vom LHC Füllschema, entweder Raumladungseffekte im Proton Synthrotron (PS) und dem Protron Synthrotron Booster oder die longitudinale Akzeptanz im Super Proton Synchrotron, wie im LHC Injector Upgrade Report dargelegt [7]. In dieser Publikation wird eine Studie der wesentlichen Grenzen solcher High-Brightness Strahlen des CERN PS diskutiert und ein Schema zu deren Abschwächung vorgeschlagen.

Die Wechselwirkung zwischen Raumladungs-Tuneshift und Resonanzen im Kontext der hohen Intensitäten des PS wurde bereits in einer früheren Arbeit studiert [8–10], wobei der Raumladungs-Tuneshift in der Größenordnung von 0.1 lag und dieser für Teilchen im Zentrum auf Grund der Gaußartigen Ladungsverteilung stets größer war (kleinerer inkohärenter Tune). Ein Oktupolmagnet wurde verwendet, um eine resonanztreibende Harmonische von 25 (=$4Q_x$) in der horizontalen Ebene zu erzeugen und die Strahlemittanz und die Strahlverluste wurden als Funktion des reinen Tunes (Bare-Tune) gemessen.

Eines der Ergebnisse dieser früheren Studie war, dass der Strahl sich innerhalb von zwei Bereichen verschieden verhält, je nachdem, ob das Zentrum oder der Rand der Teilchenverteilung eine Resonanz überdeckt. Wenn das Zentrum eine Resonanz überdeckt, so wächst die Emittanz ohne Strahlverluste an (solange die physikalische Apertur hinreichend groß ist). Wenn nur der Rand die Resonanz überdeckt und der Tune mit Synchrotronoszillationen moduliert wird, so werden Teilchen im Wechsel von den Resonanzinseln eingeschlossen und wieder freigegeben. Ihre jeweiligen Amplituden können so anwachsen und die physikalische Apertur treffen, was zu einem stetigen Strahlverlust führt.

Zur Produktion der üblichen operativen Strahlen wird das CERN PS derzeit bei Tunes betrieben, die bei Injektion zwischen 6.10 und 6.25 in jeweils horizontaler und vertikaler Ebene liegen. Eine experimentelle Studie hat gezeigt, dass die hauptsächlichen Grenzen in der Leistung des PS bezüglich künftiger High Luminosity (HL)-LHC Strahlen die ganzzahligen Resonanzen und die Q_y=6.25 Resonanz ist. Die Tune-Verteilung des Strahls ist hierbei zwischen diese Resonanzen beschränkt.

Obwohl die Intensität des LHC Strahles nicht so hoch ist wie in der früheren Studie [8–10], ist die Raumladungstuneverteilung auf Grund der kleineren Emittanz in der gleichen Größenordnung. Deshalb ist es sinnvoll anzunehmen, dass sich der Strahl ähnlich verhält. Das bedeutet, dass das Strahlzentrum beim Überdecken des ganzzahligen Tunes Q_y=6.00 Emittanzaufblähung verursacht. Auf der anderen Seite erfährt der Rand des Strahles den Effekt des Fangens und Befreiens an der Viertelresonanz Q_y=6.25, wie diskutiert. Zu beachten ist außerdem, dass es Resonanzlinien höherer Ordnung bei der Resonanzbedingung Q_y=6.00 gibt.

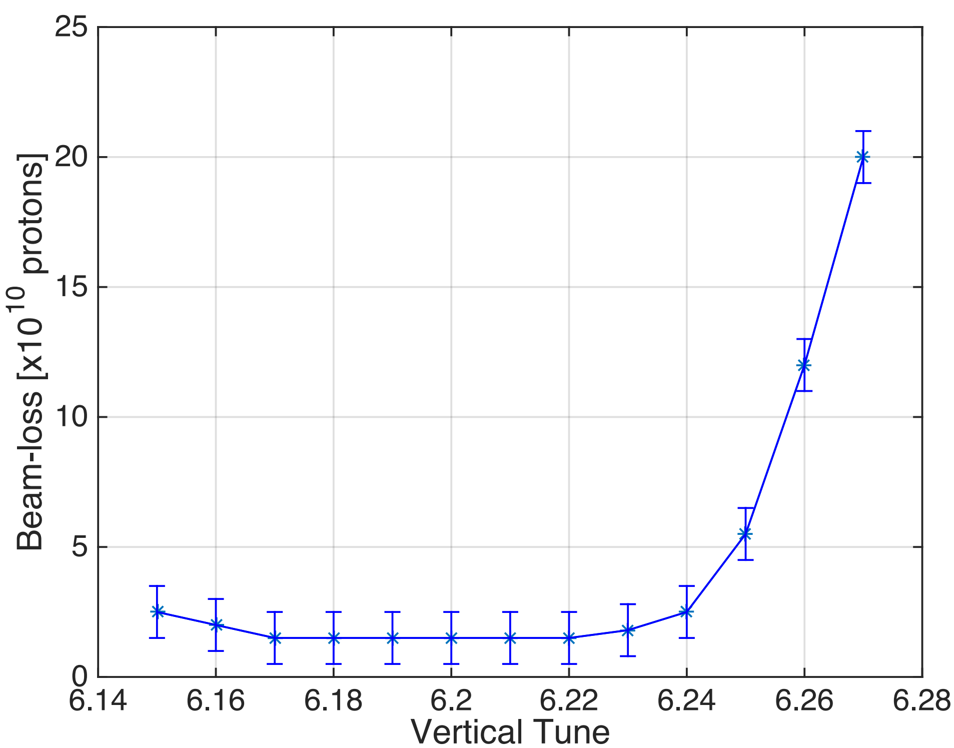

ABBILDUNG 1: Verluste bezüglich des vertikalen Arbeitspunktes bei konstantem horizontalem Tune 6.23.

Experimente mit hoher und niedriger Intensität liefern klare Indizien, dass die Resonanz im PS durch Raumladungseffekte getrieben wird. Mit einem Strahl hoher Intensität deuten Resultate von Experimenten, die bei einem festgehaltenen horizontalen Tune $Q_x = 6.23$ und einem Scan in einem Bereich vertikaler Tunes durchgeführt wurden, auf den im Folgenden abgebildeten resonanzbedingten Strahlverlust hin (Abb. 1). Im Gegenzug zeigen Experimente mit geringer Intensität, wo Raumladungseffekte nahezu vernachlässigbar sind, keinen Effekt um die Resonanzlinie Q_y=6.25 (Abb. 2). Die einzigen Unterschiede zwischen den beiden Experimenten sind die Intensität und die Strahlparameter. Im Folgenden soll versucht werden, die Aussage, dass die Resonanzen im PS durch Raumladung getrieben werden, zu erhärten, wobei die Argumente auf einer Kombination von Simulation und Experiment beruhen.

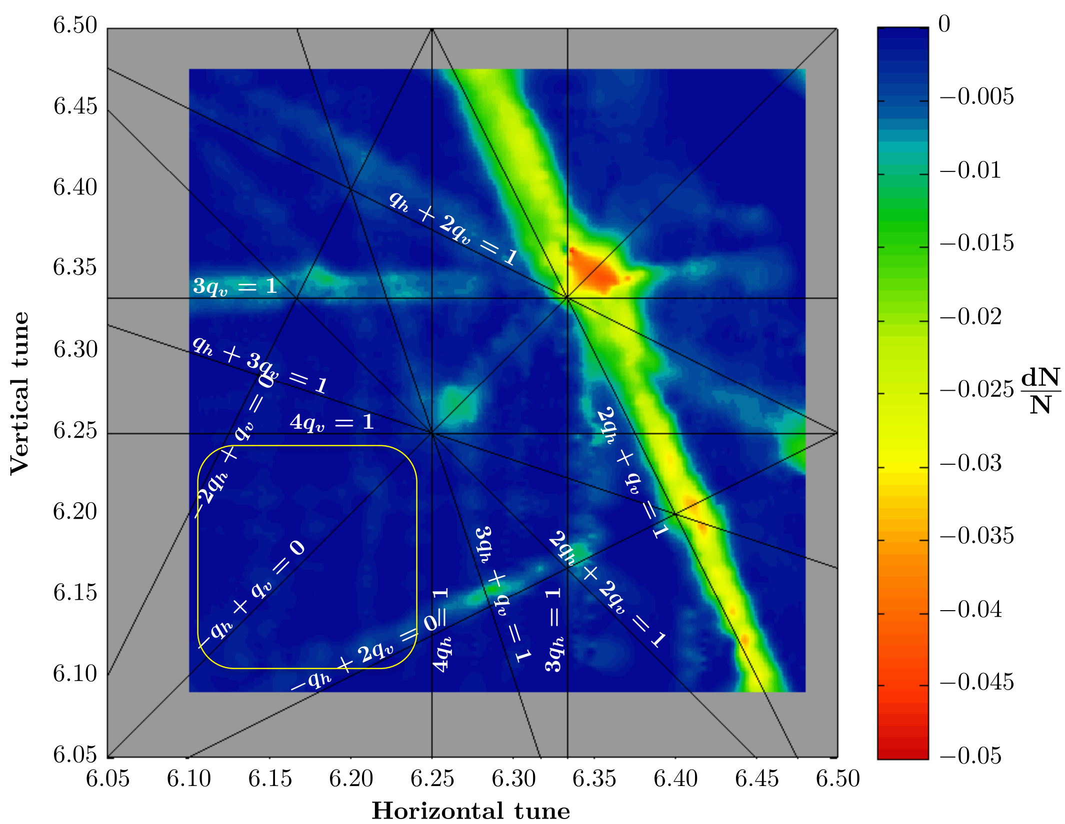

ABBILDUNG 2: Tune gegenüber Strahlverlust. Der Farbcode zeigt den relativen Strahlverlust. Der operative Arbeitsbereich ist durch das Rechteck gekennzeichnet. q_h und q_v sind die fraktionellen Anteile des horizontalen und vertikalen Tunes.

0.2 Raumladungsgetriebene Resonanzen

0.2.1 Der treibende Anteil im PS Lattice

Unter der Annahme, dass die Ladungsverteilung Gaußsch bezüglich der transversalen Ebene ist, kann dessen Potential wie folgt geschrieben werden[11, 12]

$$\begin{aligned} V_{sc} = & \frac{r_p \lambda}{\beta^2 \gamma^2 B_f} \left[-\frac{x^2}{\sigma_x (\sigma_x + \sigma_y)} - \frac{y^2}{\sigma_y (\sigma_x + \sigma_y)} \right. \\ & + \frac{2\sigma_x + \sigma_y}{12 \sigma_x^3 (\sigma_x + \sigma_y)^2} x^4 + \frac{x^2 y^2}{2 \sigma_x \sigma_y (\sigma_x + \sigma_y)^2} \\ & \left. + \frac{\sigma_x + 2\sigma_y}{12 \sigma_y^3 (\sigma_x + \sigma_y)^2} y^4 + \dots \right] \end{aligned}$$

wobei x und y die horizontalen und vertikalen Koordinaten sind, σ_x und σ_y die RMS Strahlgrößen in horizontaler und vertikaler Ebene, r_p der klassische Elektronenradius, λ die longitudinale Raumladungsdichte, β und γ die relativistischen Faktoren, B_f der Bunching-Faktor, definiert als Verhältnis der gemittelten Ladungsdichte zur Spitzendichte. Auf Grund der Symmetrie der Ladungsverteilung enthält das Potential nur Terme gerader Ordnung. Die Strahleinhüllende und die Resonanzbreite bzw. Stärke enthalten die Lattice β-Funktion, womit eine harmonische Analyse auf die β-Funktion eine Abschätzung für die Stärke der raumladungsgetriebenen Resonanz liefert [13].

Das PS hat 100 Combined-Function Magnete, jeder unterteilt in eine fokussierende und defokussierende Hälfte, womit deshalb 50 “FDODFS-Zellen entstehen. Es gibt 10 längere gerade Strecken, die, zusammen mit den Magneten, eine 10-superperiodische Struktur ergeben. Die Tunes werden bestimmt durch die Quadrupolkomponenten der Hauptmagnete. Die Maschine wird hierbei im operativen Tune-Bereich gehalten, entweder durch speziell dafür vorgesehene Quadrupole oder durch vier Kreisläufe von Polflächenwindungen (PFW) und eine Figure-8 Schleife (F8L), je nach Energiebereich[14].

Die Q_y=6.25 Resonanzlinie hat eine interessante Eigenschaft: Sie kann dargestellt werden durch $4Q_y = 25$ oder $8Q_y = 50$, die im Falle des PS eine strukturelle Resonanz ist. Aus Sicht der Raumladungseffekte ist insbesondere die Harmonische von 50 wichtig. Obwohl die FDODF 50-Zellen-Symmetrie durch die Verwendung von Niedrigfeld-Quadrupolen und der längeren geraden Sektionen leicht gestört wird, ist die dominierende Harmonische, die sich aus der vertikalen β-Funktion (oder Strahleinhüllenden) ergibt, nach wie vor 50, wie in Abb. 3 gezeigt.

In dieser Rechnung sind keine mechanischen oder magnetischen Fehler einbezogen und deshalb entstehen keine Harmonischen der Vielfachheit 10. Wenn diese Fehler einbezogen werden würden, die in einer realen Situation unvermeidbar sind, so würde auch jede andere Harmonische, inklusive der Harmonischen 25, auftreten. Allerdings wären diese wesentlich schwächer gegenüber der Harmonischen von 50.

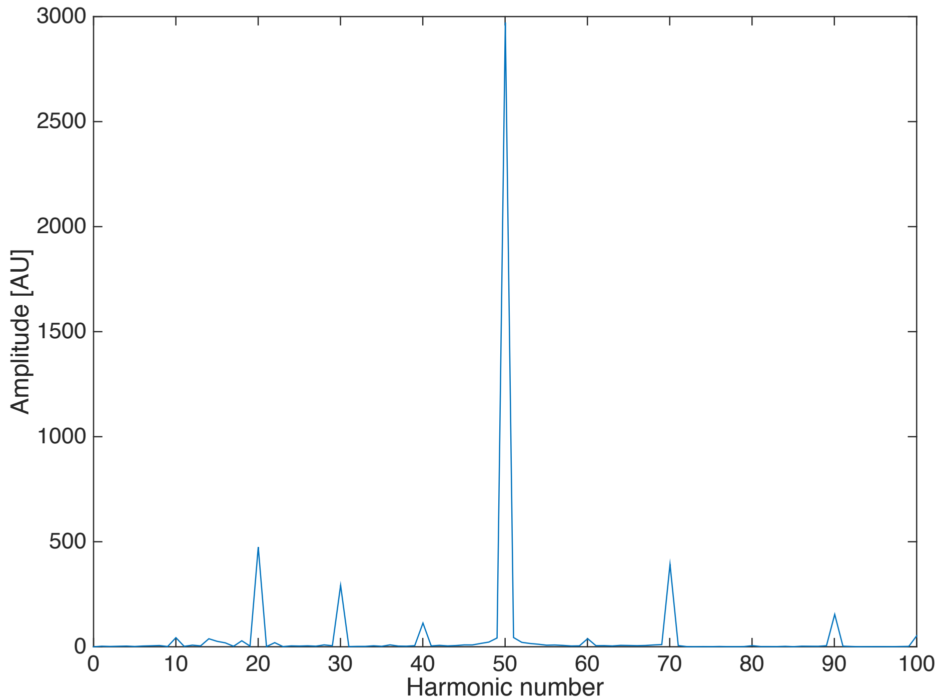

ABBILDUNG 3: Harmonische der vertikalen β-Function mit operativen Einstellungen der PFW und der F8L.

0.2.2 Beobachtungen

Resonanz-kreuzende Messungen mit vier Strahlen verschiedener Helligkeit wurden durchgeführt, um herauszufinden, ob die Strahlhelligkeit einen Beitrag zu den Strahlverlusten liefert.

Der horizontale Tune wurde bei 6.23 belassen, wohingegen der vertikale Tune von 6.24 auf 6.30 innerhalb von 20 ms geändert wurde, dann für 300 ms konstant gelassen wurde und schließlich wieder auf 6.24 herabgesetzt wurde innerhalb von 20 ms. Der Vorteil dieser Vorgehensweise liegt darin, die Zeiten der Strahlverluste genau kontrollieren zu können. Die vier verschiedenen Strahlen sind in Tabelle 1 aufgeführt.

TABELLE 1: Maximales Detuning durch Raumladung für die vier Strahlen, die verwendet wurden beim Kreuzen über die Resonanz Q_y=6.25.

Beam ID	ΔQ_x	ΔQ_y
Beam 1	-0.22	-0.40
Beam 2	-0.18	-0.37
Beam 3	-0.08	-0.24
Beam 4	-0.01	-0.01

In Abb. 4 ist die relative Intensität der vier Strahlen als Funktion der Zeit dargestellt. Die gestrichelte Linie ist der vertikale Tune entlang des Zyklus, wobei beachtet werden muss, dass ein Offset von 0.65 auf den Tune addiert wurde, um auf die gleiche vertikale Skala wie die relativen Intensitäten zu kommen. Es ist ersichtlich, dass die Strahlverluste direkt mit den Raumladungseffekten korreliert sind, hier gegeben duch den maximalen Tune-shift. Diese Messung bestätigt den Zusammenhang zwischen Strahlhelligkeit und Resonanzanregung.

0.2.3 Phasenraumstruktur

Da wir erwarten, dass die Resonanz durch Raumladung getrieben ist, schauen wir auf die Situation bei festgelegten Positionen s (longitudinal) und x (horizontal), so dass wir die gleiche Raumladungskraft haben und deshalb die gleiche Resonanzanregung.

Es zeigt sich, dass der Phasenraum eine resonante Struktur für Teilchen nahe dem Strahlzentrum aufweist, wobei hier keine longitudinale Bewegung stattfindet. In Abb. 5 ist der vertikale Phasenraum mittels PTC-ORBIT und dem 2.5 D selbst-konsistenten Raumladungsmodell dargestellt für Teilchen die bei s=0 m in longitudinaler Richtung starten und gleicher horizontaler Position und gleichem Winkel.

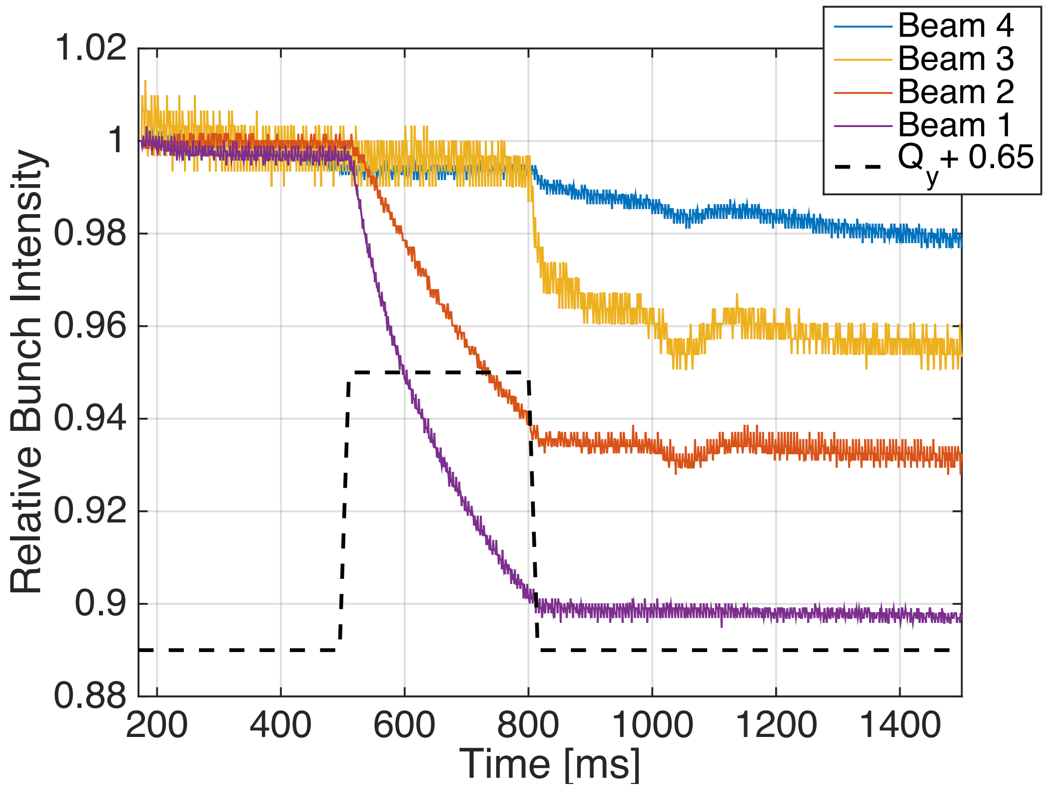

ABBILDUNG 4: Normierte Intensität der vier Strahlen mit verschiedenen Raumladungskräften beim Kreuzen über die Q_y=6.25 Resonanz (durchgezogene Linien). Die gestrichelte Linie zeigt den vertikalen Tuneschritt mit einem Offset von 0.65 um auf die selbe vertikale Skala zu kommen.

Der Phasenraum zeigt eine deutliche 8. Ordnungsresonanz die bis zu 25 mm in die vertikale Ebene hineinreicht bei der ersten Sektion des PS (β_y=11.8 m) und bis zu 35 mm an den Stellen mit dem größten β_y=23.0 m, was das mechanische Aperturlimit darstellt (Die Ausdehnung könnte in Abhängikeit von der horizontalen Koordinate sogar noch etwas größer sein). Dies erklärt die auftretenden Strahlverluste beim Kreuzen der Resonanz.

Mehrere Versuche wurden unternommen, den Phasenraum direkt zu messen, jedoch war auf Grund der Natur der Resonanz keiner erfolgreich. Die Positionen der Inseln, die durch den Strahl angeregt werden,

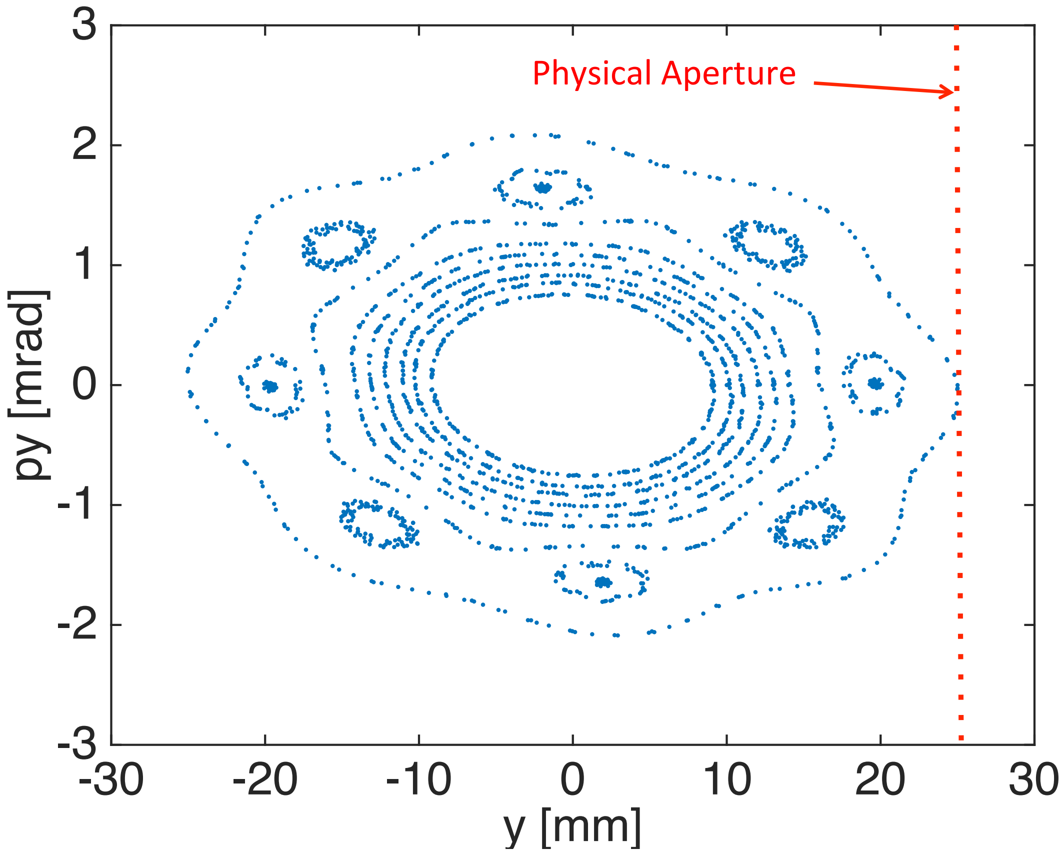

Abbildung 5: Vertikaler Phasenraum für Teilchen im Zentrum des Bunches horizontal und vertikal, erhalten durch PTC-ORBITT [1], bei Vernachlässigung aller Spiegelladungseffekte.

hängen von x und s ab.

Nichtsdestotrotz zeigen Simulationen mit PTC-ORBIT und IMPACT [15] die 8. Ordnungsstruktur. Es ist hierbei zu berücksichtigen, dass alle Codes sehr ähnliche Phasenraumtopologien und Inselamplituden liefern, unabhängig von Unterschieden beim Tracking und den Raumladungsmodellen. In diesen Simulationen liefern die Selbst-Felder die einzigen nicht-linearen Beiträge; somit können wir schließen, dass die

8. Ordnungsresonanz durch Raumladung getrieben wird. Die Tatsache, dass wir 8 Inseln und nicht 4 beobachten, bestätigt, dass nur die Harmonische 50 ($= 8 \times 6.25$) angeregt ist.

0.2.4 Strahlverlustsimulation

Für den Vergleich zur Messung ist der im Folgenden diskutierte Satz von Simulationen, unter Verwendung des Frozen-Modells in pyORBIT [16], durchgeführt worden. Obwohl eine selbstkonsistente Simulation zu bevorzugen wäre, wäre die hierbei erforderliche Rechenzeit unrealistisch (z.B. würde eine Simulation von 500 ms Realzeit in etwa 250 Tage auf 48 Kernen benötigen). In diesem Modell sind sowohl direkte (Coulomb) als auch indirekte (Bildladung) Raumladungskräfte berücksichtigt.

Das PS Lattice ist hierbei als rein lineare Struktur modelliert worden und Raumladungseffekte waren die einzigen nicht-linearen Effekte. Die Strahlparameter sind in Tabelle 2 gezeigt. Der vertikale Tune

TABELLE 2: Simulationsparameter.

Parameters	Value
Intensity [10^{10} ppb]	30
ϵ_x (1σ normalized) [mm.mrad]	1.6
ϵ_y (1σ normalized) [mm.mrad]	1.5
Bunch length [ns]	92
$\Delta p/p$ (rms)	$0.51\ 10^{-3}$
E_{kin} [GeV]	1.4

wurde 500 ms nach Injektion von 0.24 auf 0.29 geändert und anschließend konstant gehalten, um das Experiment wiederzugeben.

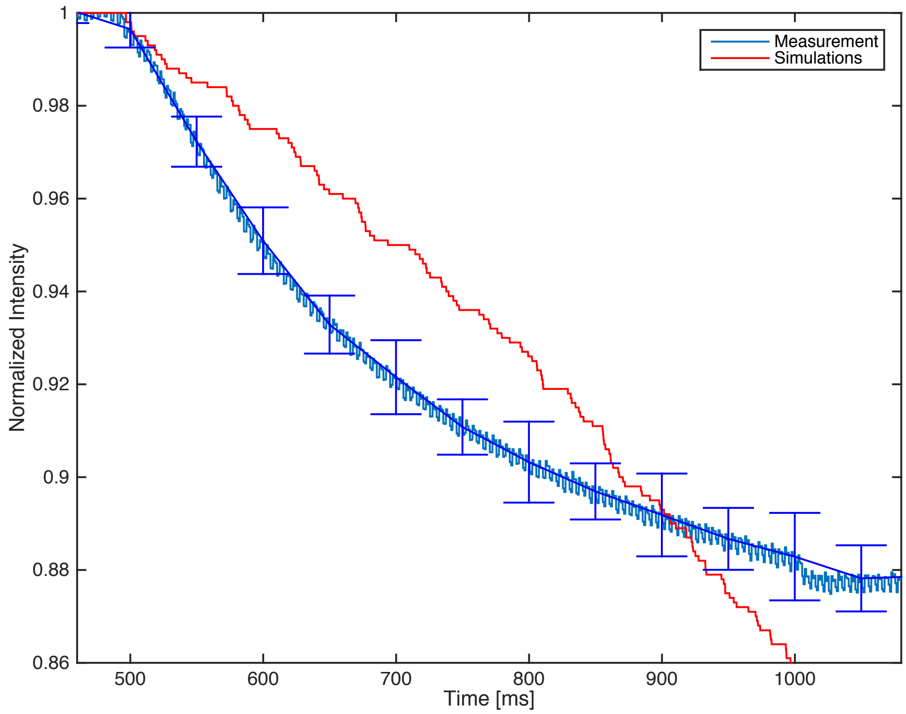

Abbildung 6: Relativer Strahlverlust beim Kreuzen der Resonanz, simuliert (rot) und gemessen (blau).

In Abb. 6 zeigt die blaue Kurve den gemessenen normierten Strahlverlust, der mit den Simulationsergebnissen in Rot verglichen werden kann. Die Fehlerbalken entsprechen der Standardabweichung über 10 Messungen der gemessenen Kurve.

Die Schlussfolgerung aus Abb. 6 ist, dass Raumladung in gewissem Sinne die Größenordnung des Strahlverlustes erklärt, obwohl die Übereinstimmung zwischen dem Experiment und der Simulation nicht exakt ist. Der Unterschied könnte darauf zurückzuführen sein, dass Raumladung in der Simulation durch ein Frozen-Modell dargestellt ist, das einen Sättigungseffekt der Kurve nicht enthalten kann, insbesondere nicht für einen relativ kleinen Strahlverlust. Zusätzlich kommt hinzu, dass der Strahlverlust generell sehr schwierig zu reproduzieren ist, denn dieser hängt von der Halo Population ab. Da der Halo größenordnungsmäßig einige wenige Prozent oder weniger der gesamten Strahlintensität betragen kann, ist dies nahezu unmöglich mit Wirescannern zu messen.

0.3 Verringerung der Strahlverluste

0.3.1 Emittanzwachstum

Als ein Mittel gegen die Effekte der Resonanz kann eine Änderung des vertikalen Tunes die Harmonische 50 vermeiden, ‘also damit diese strukturelle Resonanz. Es wurde deshalb in Erwägung gezogen, den vertikalen ganzzahligen Tune von 6 auf entweder 5 oder 7 zu ändern.

Um diese Hypothese zu untersuchen, wurde eine erste Serie an Simulationen mittels PTC-ORBIT [1] gestartet, die ausschließlich direkte Raumladungskräfte (d.h. Coulomb) berücksichtigt. Um die Effekte ausschließlich auf die Resonanz bei Q_y=6.25 einzuschränken und Effekte anderer Resonanzen zu vermeiden, wurden die Simulationsparameter künstlich so angepasst, dass der Tune-shift nur die Resonanzlinie Q_y=6.25 trifft. Es wurde hierbei kein Strahlverlust festgestellt. Die Resultate basierten auf der 95%-Emittanz, um zwischen der nominellen Optik, basierend auf den ganzzahligen Tunes (6, 6), und der Split-Tune Optik bei (5, 7) zu unterscheiden.

Abb. 7 zeigt einen klaren Unterschied zwischen den Optiken beim Verhalten der 95% Emittanz. Im Falle der nominellen Optik gibt es einen deutlich sichtbaren Anstieg der 95% Emittanz, der durch das Kreuzen der vertikalen Resonanz verursacht wird und der etwa 8 mal stärker als im Falle der Split-Tune Optik ist. Des Weiteren zeigen die Resultate, da in den Simulationen Raumladung als die einzige nicht-lineare Kraft eingeht, dass die Resonanz raumladungsbedingt getrieben wird. Die Tatsache, dass der Resonanzeffekt deutlich größer bei der ganzzahligen Resonanz 6 ist, deutet darauf hin, dass eine strukturelle Resonanz vorliegt.

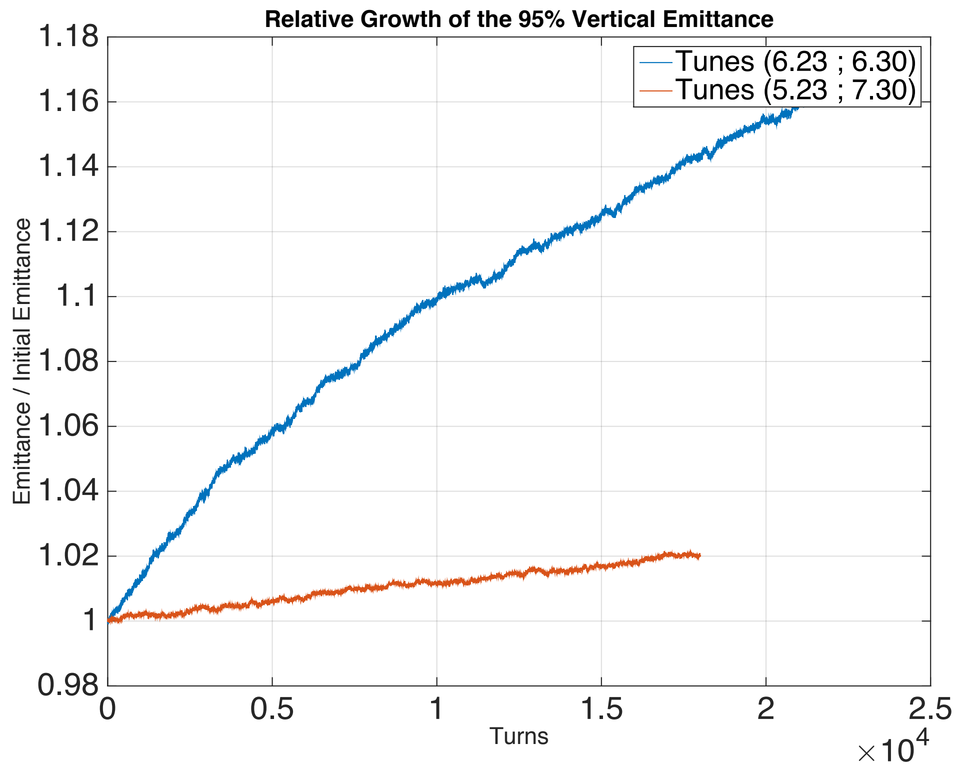

Abbildung 7: Relatives Wachstum der 95%-Emittanz für die nominelle (blau) und die Split-Tune Optik (rot).

0.3.2 Strahlverlust

Für die experimentelle Bestätigung wurde der vertikale Tune um einen ganzzahligen Wert durch Verwendung der F8L geändert, was den Vorteil hat, das Quadrupolfeld zu ändern, ohne dass die höheren Ordnungen eine nennenswerte Rolle spielen [17]. Die Benutzung des Kreislaufs hat allerdings den Effekt, dass dieser auf beide transversalen Tunes in gegensätzlicher Richtung wirkt.

Die Messkampagne fiel zusammen mit dem Neustart der Maschine in 2014. Nachdem der Strahl aufgesetzt wurde, war es möglich, einen LHC-artigen Strahl in die Split-Tune Optik zu injezieren. Verschiedene Tests wurden durchgeführt um die neuen Tunes mit der Optik zu bestätigen. Alle Messungen stimmten mit dem Modell überein, wobei das Beta-Beating und das Dispersions-Beating in der Größenordnung von 10% lag, siehe 4.

Die Messungen bestanden in erster Linie aus dem Tune-Schritt, in dem der horizontale Tune konstant gelassen wurde, während der fraktionelle vertikale Tune von 0.24 auf das Plateauniveau geändert wurde, dort für die nächsten 500 ms konstant gelassen wurde und dann zurückgestellt wurde auf 0.24. Das Plateauniveau ist hierbei zwischen 0.24 und 0.34 variiert worden, um den Effekt der verschiedenen Arbeitspunkte zu sehen, siehe Abb. 8.

Im Falle der nominellen Optik war das Verhalten ähnlich zu dem gemessenen in Abb. 4. Abb. 9 zeigt, dass, je höher das Plateauniveau ist, desto höher auch der Strahlverlust ist. Dies wird erklärt durch die

Zahl und Natur der Teilchen, die die Resonanz kreuzen. Ist der vertikale Tune höher, so überlappt der untere Teil der Tune-Krawatte die Resonanz, was bedeutet, dass Teilchen eine höhere Amplitude haben und dies dann in höheren Strahlverlust mündet.

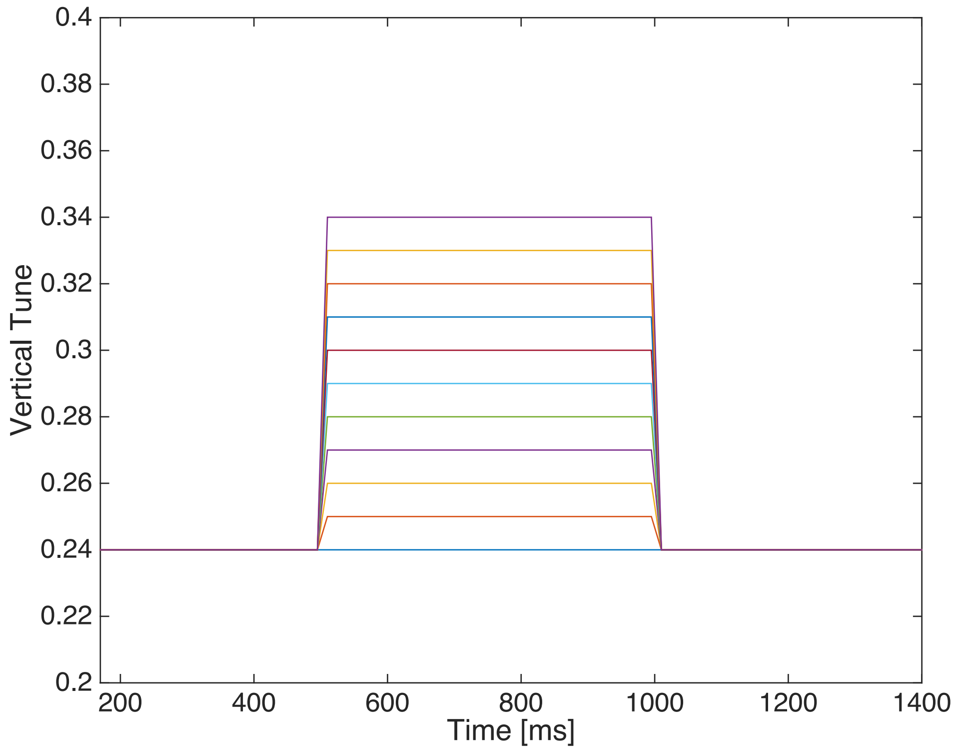

ABBILDUNG 8: Vertikaler programmierter Tuneschritt um über die Resonanz zu gelangen. Der fraktionelle Teil beginnt bei 0.24 und geht auf ein Plateauniveau und schließlich zurück auf 0.24. Das Plateauniveau variiert zwischen 0.24 und 0.34.

Im Falle der Split-Tune Optik verschwanden die Strahlverluste, wie in Abb. 10 zu sehen ist.

Die einzige Kurve mit deutlichen Verlusten beim Kreuzen der 3. Ordnungsresonanz $3Q_y = 22$, die bekanntermaßen angeregt wurde, gehört zu Q_y=7.34, siehe Abb. 2.

Wenn wir die beiden Abbildungen kombinieren, so erhalten wir Abb. 11

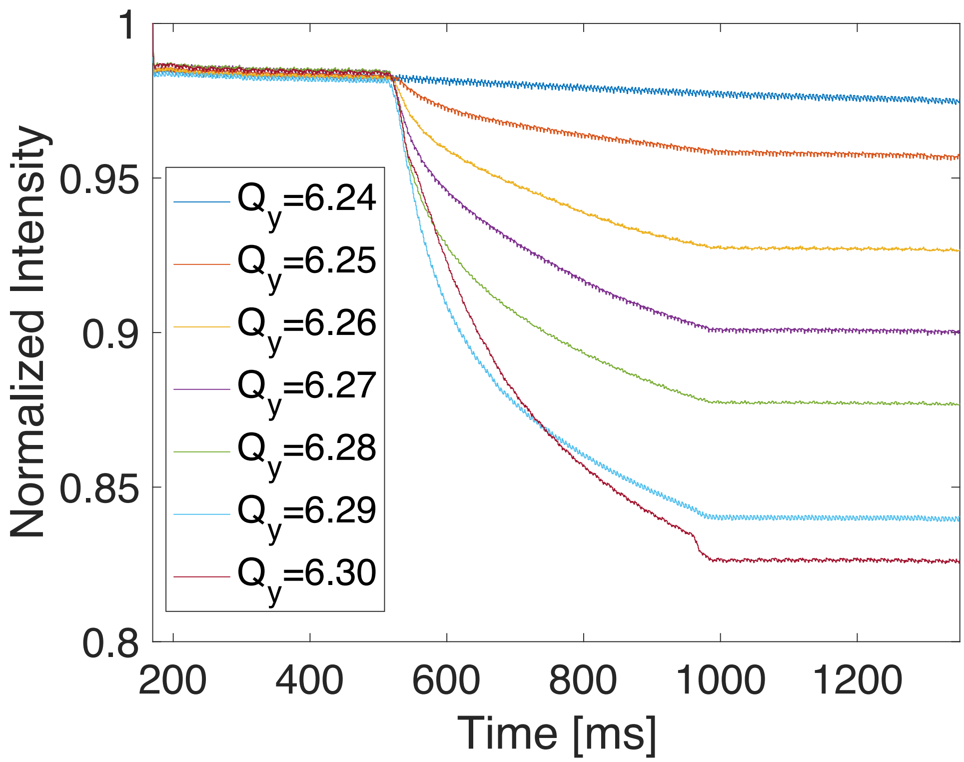

ABBILDUNG 9: Relativer Intensitätsverlust beim Kreuzen über die Resonanz für die nominelle (6,6) Optik.

(in dieser Abbildung ist das Plateau für 0.34 im Falle der Split-Tune Optik nicht gezeigt, da es durch eine andere Resonanz beeinflusst wurde.) Der Effekt des Resonanzübergangs wird vernachlässigbar im Falle der Split-Tune Optik. Dieses Resultat ist sehr interessant, denn es bestätigt, dass die Resonanz strukturell ist ($h = 50$) und verschwindet, sobald die Harmonische auf 58 gesetzt wird.

0.3.3 Diskussion

Es stellt sich heraus, dass die Änderung der ganzzahligen Resonanz ein effektives Mittel ist, um die schädlichen Auswirkungen der Resonanz abzumildern und gleichzeitig wird bestätigt, dass es sich um eine

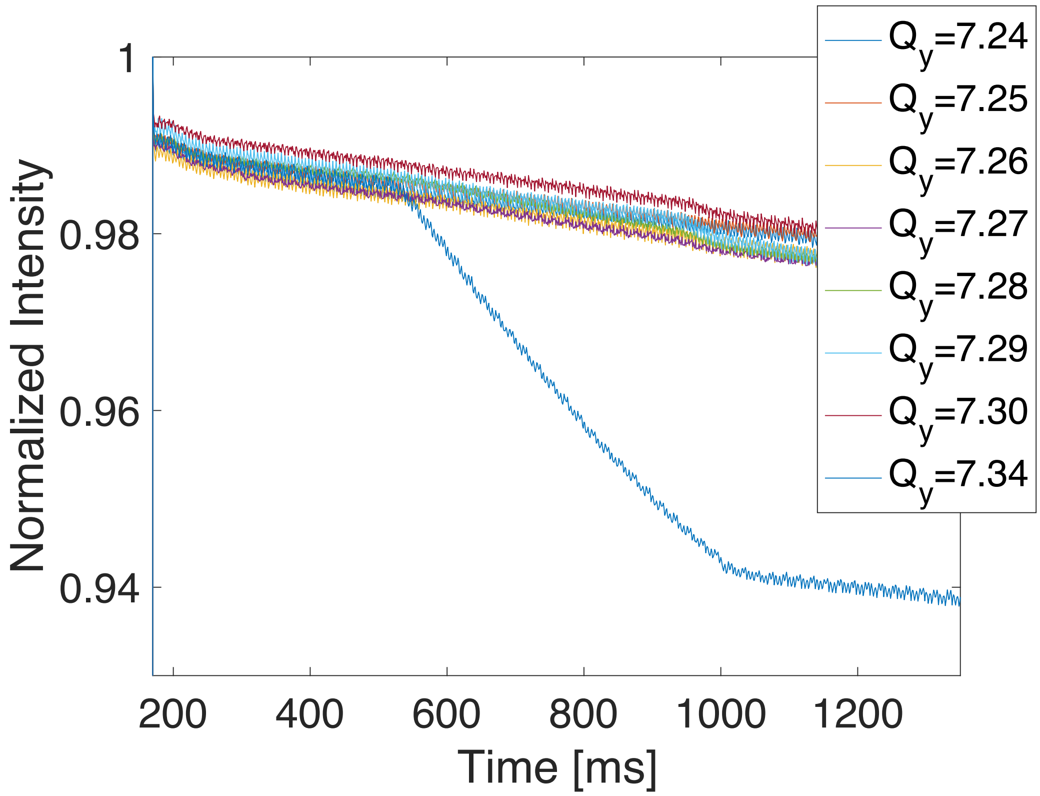

ABBILDUNG 10: Relativer Intensitätsverlust beim Kreuzen über die Resonanz für die (5,7) Optik.

strukturelle Resonanz 8. Ordnung, getrieben durch Raumladung, handelt. Nichtsdestotrotz müssen andere Herausforderungen überwunden werden, um diese Optik in den regulären Betrieb zu übernehmen: Beispielsweise muss die Position der Fast-Pulse-Magnete, die beim Transition-Crossing eine Rolle spielen, geändert werden. Die Herausforderung hier besteht darin, eine geeignete Position zu finden die sowohl den nominellen Tunes wie auch den Split-Tunes genügt, denn die nominellen Tunes müssen nach wie vor für den Fall großer Strahlgrößen verwendet werden. Der Verlustmechanismus konnte ebenfalls erklärt werden durch die Amplituden der Inseln in Abb. 5, die etwa so groß wie die Strahlröhre selbst sind. Die Positionen der Inseln variieren in Abhängigkeit vom Raumladungsdetuning der Teilchen. Die

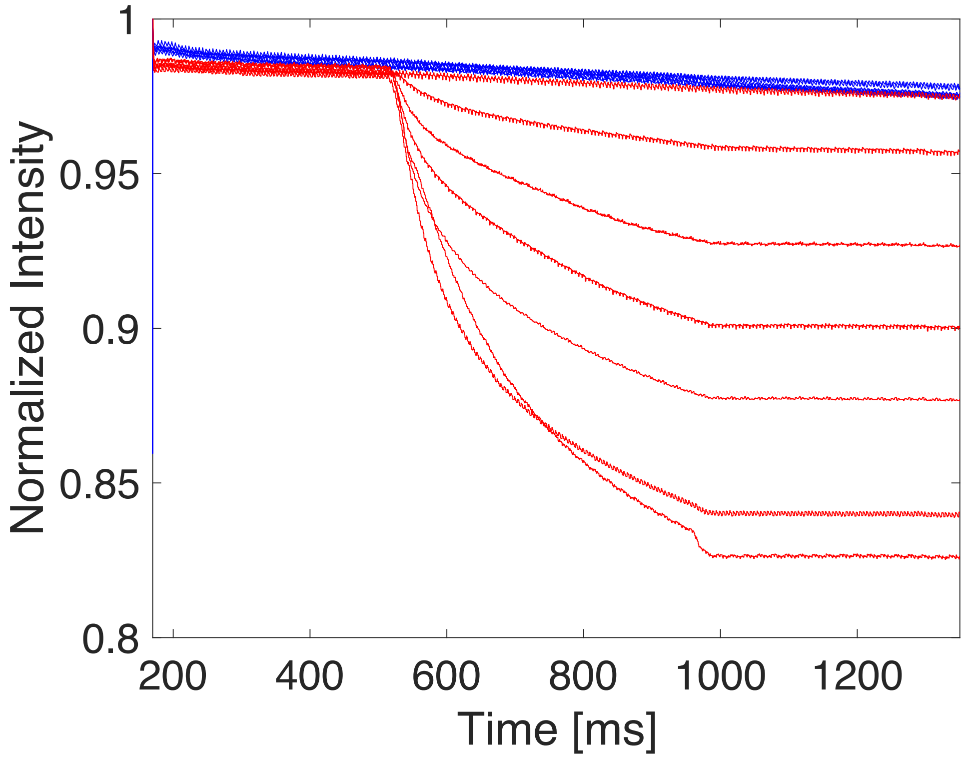

ABBILDUNG 11: Relativer Intensitätsverlust beim Kreuzen über die Resonanz unter nomineller (rot) und Split-Tune Optik (blau).

Synchrotronoszillationen, die horizontale Position und der chromatische Effekt tragen ihre Anteile zu einer Tune-Änderung der Teilchen bei, die diese in Resonanz bringen können.

0.4 Schlussfolgerung

Im PS wurde beobachtet, dass die Q_y=6.25 Resonanz nur im Falle von hoher Strahlintensität angeregt ist, was zu der Hypothese einer raumladungsgetriebenen Resonanz führt. Eine Analyse der PS β-Funktion deutet darauf hin, dass die Strahleinhüllende eine sehr starke Harmonische von 50 enthält, unabhängig von den kleinen Störungen der

Symmetrie, was zu dem Schluss führt, dass eine raumladungsgetriebene Resonanz die gleiche Harmonische besitzt und deshalb $8Q_y = 50$ gilt. Simulationen, in denen nur Raumladung als einzig mögliche Quelle von Nichtlinearitäten in Frage kamen, haben klar eine Resonanz 8. Ordnung im Phasenraum gezeigt sowie einen Strahlverlust in der gleichen Größenordnung. Dies bestätigt, dass es sich bei der Resonanz um eine strukturelle Resonanz 8. Ordnung handelt, die von Raumladung getrieben ist. Ein Wechsel des Tunes wurde vorgeschlagen als Gegenmaßnahme und dieser liefert eine weitere Bestätigung der Hypothese. Erwartungsgemäß ist der Effekt der Resonanz vernachlässigbar geworden nach Wechsel des Tunes. Es ist außerdem interessant, dass sich diese Studie auf die vertikalen Resonanzlinie Q_y=6.25 konzentriert, denn die vertikale Strahlgröße ist hier kleiner, was im Resultat einem größeren vertikalen Raumladungsdetuning entspricht. Die horizontale Resoanzlinie ist nicht leistungslimitierend, es wurde jedoch beobachtet, dass diese ebenfalls für die Strahlintensität gefährlich werden kann. Diese Resonanz ist ebenfalls von 8. Ordnung und strukturell, getrieben durch Raumladung und könnte ebenso abgemildert werden, indem der horizontale Tune geändert wird.

Chapter 1

Introduction

1.1 LIU and general motivation

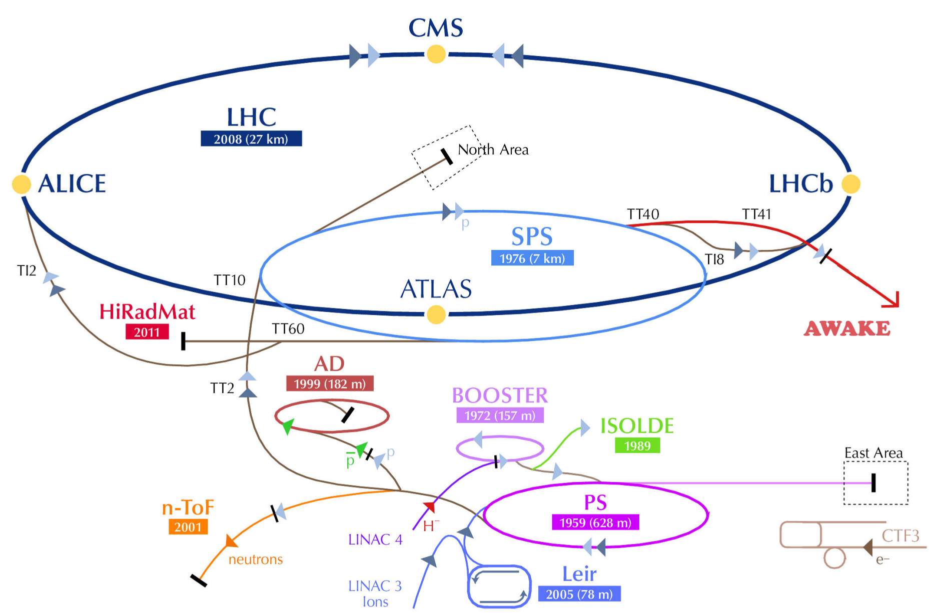

FIGURE 1.1: The CERN accelerator complex.

The Large Hadron Collider (LHC) [18] is the world largest particle accelerator with its 27 km circumference. The LHC was designed and built at the European Organization for Nuclear Research (CERN) in order to collide protons and lead ions at a center of mass energy of 7 TeV (ions 7 TeV proton equivalent). The accumulate collision data lead to the discovery of the Higgs boson in 2012 [19], which has opened the door to more possibilities and studies in the field of High Energy Particle Physics. The existence of the Higgs boson completes the missing piece of the Standard Model theory [19], the theory that describes the interaction between elementary particles. The discovery of the Higgs is a motivation for further studies of its precise properties and of the possibility of a more complex theory beyond the standard model. The amount of accumulated data is one of the most essential parameters for any study, which is proportional to the number of collisions in the LHC, which in turn is proportional to quantity defined as luminosity. The High Luminosity LHC (HL-LHC) [6] project aims to significantly increase the instantaneous luminosity L, expressed as in Eq. 1.1 and the amount of accumulated data is proportional to the luminosity.

$$L = \frac{N^2 \, f \, n_b}{4\pi \, \sigma_x^* \sigma_y^*} F \tag{1.1}$$

where N is the intensity per bunch, f is the beam revolution frequency, n_b is the number of colliding bunches, $\sigma_{x,y}^*$ is the RMS beam size in x/y plane at the collision point and F is a factor that depends on the geometry of the collision.

Increasing the accumulated data over a certain period of time means increasing the luminosity, which requires an upgrade of the LHC injectors in order to deliver brighter beams (the brightness is proportional to the ratio of the bunch intensity to is emittance). The LHC Injectors Upgrade (LIU) [7] project aims to upgrade the injectors (PSB, PS, SPS plus the introduction of LINAC4) in order to cope with the future demand of the LHC beams.

For the LHC beams production, the transverse emittance before the LIU upgrade is determined by the multi-turn injection from the Linac2 to the PSB (after the upgrade the LINAC4 will replace LINAC2), the longitudinal bunch spacing and structure is determined by the PS and the final beam adjustments (tail scrapping and bunch length adjustments) are performed in the SPS. The maximum intensity per bunch is limited by the longitudinal acceptance and stability in the PS and SPS [20][21], as well as space charge (Coulomb repulsion between same charge particles, see section 1.4). The number of bunches is limited by the RF gymnastics in the PS and the number of PS injections in the SPS. The beam size $\sigma^*_{x,y} = \sqrt{\beta^*_{x,y}\epsilon_{x,y}}$ ($\epsilon_{x,y}$ is the RMS normalized emittance in x/y plane) is limited by the space charge in the PSB, PS and SPS.

The limiting machine between the injectors depends on the LHC production scheme (number of bunches, bunch spacing, intensity per bunch...etc), Fig. 1.2 shows the limit of each machine in two diagrams, for the standard scheme (top) and the Batch Compression bunch Merging and Splitting scheme BCMS (bottom) [2]. The blue lines represent the space charge limit of each machine and the red vertical line represents the longitudinal limit of the SPS. It is important to note that the limit of the PS is always space charge.

In order to produce brighter beams, the injectors have to relax their space charge limit, which will be achieved through an energy upgrade of the different machines, Fig. 1.3 illustrates the LIU energy upgrade program: it consists of the replacement of Linac2 with Linac4, which will accelerate H^- beams up to 160 MeV/c in order to relax the space charge limitations at the PSB injection. The PSB will also be upgraded to receive beams at 160 MeV/c and accelerate them up to 2 GeV/c instead of 1.4 GeV/c, in order to relax the PS space charge limitation at injection energy.

In addition to the energy and hardware upgrade, many studies have been carried out in order to understand each machine limitations to produce higher brightness beams [23].

This thesis focuses on the space charge limitations in the PS as it is the main limitation for higher brightness LHC-type beams delivered to the SPS. This study quantifies the limitation in terms of tune-spread due to direct space charge for a given level of beam loss and emittance growth (Chapt. 2). Then we will focus on betatronic resonances that become more harmful as the beam gets brighter (Chapt. 3). The correlation between the brightness of the beam and the resonance strength led to the hypothesis of the presence of a space charge driven resonance, and given the symmetry of the PS lattice, it was thought

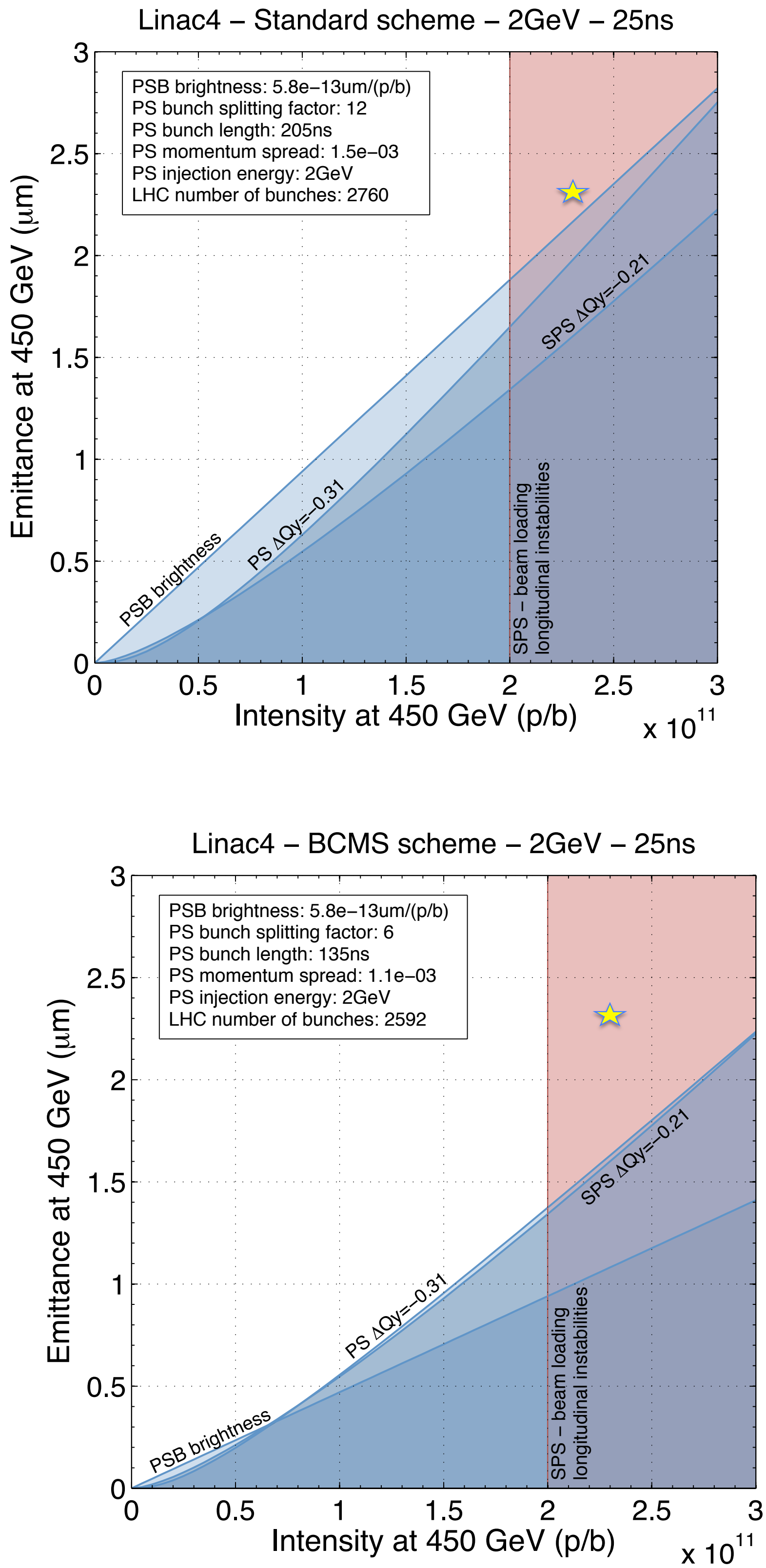

FIGURE 1.2: Machines limitations for LHC-25 ns beam production in the case of nominal scheme (top) and Batch Compression bunch Merging and Splitting scheme BCMS (bottom). The yellow star is the HL-LHC requirements for the LHC [2].

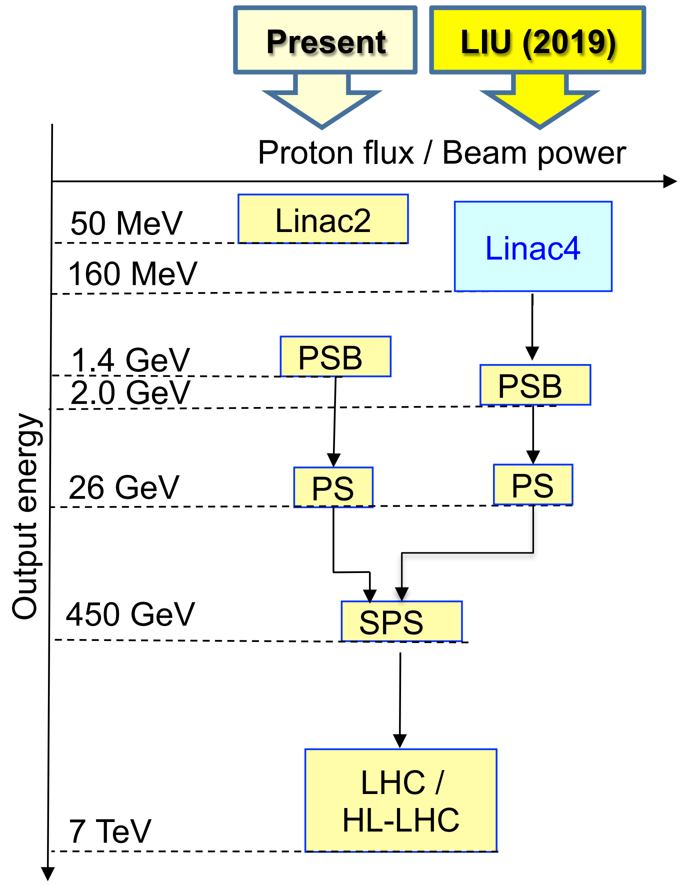

FIGURE 1.3: The LIU energy upgrade program [22].

to be a 8^{th} order structure resonance driven by space charge. Chapt. 4 proposes a mitigation for this resonance for future operations.

1.2 Single particle dynamics

This section gives a very brief overview of the main concepts and formulas of single particle dynamics used in the following chapters of this thesis. Detailed explanations and derivations could be found in particle accelerator literature [24][25].

1.2.1 Transverse dynamics

For circular accelerators, the most adapted coordinate system is Frenet reference system, following the ideal orbit along the accelerator as in Fig. 1.4, where x and y denote the horizontal and vertical transverse displacement from the ideal orbit, s denotes the longitudinal displacement along the ideal orbit and ρ is the local radius of curvature. Under magnetic dipolar field B_0, we call a reference particle the particle of charge e that follows the design orbit and therefore has a momentum p_0 such as:

$$\frac{p_0}{e} = B_0(s)\rho(s) \tag{1.2}$$

The quantity $B_0(s)\rho(s)$ is also called the magnetic rigidity, as it gives the bending radius as a function of the energy and the dipolar field.

In the linear approximation, the equations of motion, also called Hill's equations, can be written as in Eq. 1.3.

$$\begin{aligned} x'' + K_x(s)x &= \frac{\delta}{\rho} \\ y'' + K_y(s)y &= 0 \end{aligned} \tag{1.3}$$

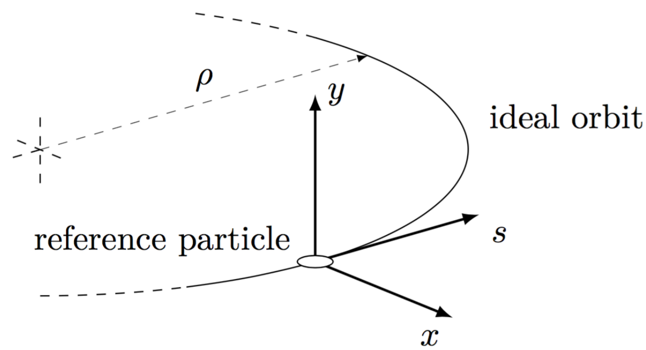

FIGURE 1.4: Curvilinear coordinate system. x and y are respectively the horizontal and vertical transverse distance from the design orbit and s is the longitudinal distance along it [4].

where:

- $x'' = \frac{d^2x}{ds^2}$, $y'' = \frac{d^2y}{ds^2}$
- $K_x(s) = -(k(s) - \frac{1}{\rho^2})$, $K_y(s) = k(s)$
- $k(s) = \frac{\partial B_y(s)}{\partial x} \frac{1}{B_0(s)\rho(s)} = \frac{\partial B_x(s)}{\partial y} \frac{1}{B_0(s)\rho(s)}$, $k(s)$ is the normalized quadrupole gradient of the magnets
- $\delta = \frac{\Delta p}{p_0}$, δ is the relative momentum deviation.

Given the periodicity of the functions $K_{x,y}(s)$ ($K_z(s) = K_z(s + C)$ because the lattice of the machine repeats itself by definition every turn, with C the circumference of the machine) and using the Floquet theorem, the general solution of the Hill's equations can be written as in Eq. 1.4

$$z(s) = \sqrt{\epsilon_z \beta_z(s)} cos(\phi_z(s) + \phi_{z,0}) + \delta D_z(s) \tag{1.4}$$

where:

- z substitutes either x or y
- ϵ_z is proportional to the area covered by a particle in the phase space (z, z'), ϵ_z is called emittance
- β_z is a periodic amplitude function, called betatron function
- ϕ_z is the betatronic phase ($\phi(s) = \int \frac{ds}{\beta(s)}$)
- $D_z = \frac{\partial z}{\partial \delta}$, D_z is called the dispersion function

The dispersion function gives the dependence of the transverse position on the momentum. Dispersion appears due to the dependence of the bending radius on the particle momentum. Therefore, in a synchrotron usually there is no dispersion in the vertical plane because there is no bending in that direction.

We can then define the betatronic tune Q_z as:

$$Q_z = \frac{1}{2\pi} \oint \phi_z(s) = \frac{1}{2\pi} \oint \frac{ds}{\beta_z(s)} \tag{1.5}$$

The chromaticity is defined as the derivative of the tune with respect to the momentum deviation (Eq. 1.6):

$$Q'_z = \frac{\partial Q_z}{\partial \delta} \tag{1.6}$$

leading to the normalized chromaticity definition (Eq. 1.7):

$$\xi_z = \frac{Q'_z}{Q_z} \tag{1.7}$$

Similarly, higher order chromaticities can be defined as the higher order derivatives with respect to the momentum deviation:

$$Q_z(\delta) = Q_{z,0} + Q'_z\delta + Q''_z\delta^2 + ... \tag{1.8}$$

Therefore a particle with a different momentum from the reference particle will have a different path for non-zero dispersion $D_z = \frac{\partial z}{\partial \delta}$ and a different tune for non-zero chromaticity $Q'_z = \frac{\partial Q_z}{\partial \delta}$.

The emittance ϵ defined in Eq. 1.4 is defined for a single particle motion. For a multi-particle beam, the emittance is defined as a statistical quantity representing the area that contains a certain percentage of the total beam, therefore it depends on the beam transverse distribution. In the case of a Gaussian beam, the most commonly used quantity is the RMS emittance ($\epsilon_{z,RMS}$) and it contains 1σ of the Gaussian beam. In this case the 1σ beam size in the transverse plane z is defined as:

$$\sigma_z(s) = \sqrt{\epsilon_{z,RMS}\beta_z(s) + D_z^2(s)\delta_{RMS}^2} \tag{1.9}$$

The total charge of the beam is called the beam intensity I and we define the beam brightness as:

$$Brightness = \frac{I}{\frac{1}{2}(\epsilon_{x,RMS} + \epsilon_{y,RMS})} \tag{1.10}$$

1.2.2 Longitudinal dynamics

While the transverse motion is defined by magnetic fields, the longitudinal one in the phase space defined by (E, t), is defined by electric fields in the Radio-Frequency (RF) cavities, where a voltage $\hat{V}$ is applied following Eq. 1.11.

$$\hat{V}(t) = V sin(\omega_{RF} t) \tag{1.11}$$

where V is the voltage amplitude, ω_{RF} is the RF angular frequency and t the time.

Similarly to the reference particle in transverse, the synchronous particle is defined as the particle that sees the same RF frequency every turn and it satisfies the following equation:

$$\omega_{RF} = h\omega_0 \tag{1.12}$$

where ω_0 is the angular revolution frequency of the particle and h is the harmonic of the RF system. In other terms, the electric field frequency has to be a multiple of the revolution frequency, in order for the synchronous particle to see exactly the same voltage at each turn. If the harmonic number is larger than 1, then there could be h synchronous particles.

We define the momentum compaction factor α_c as:

$$\frac{dC}{C} = \alpha_c \frac{dp}{p} \tag{1.13}$$

where C is the particle path length and p is the particle momentum. α_c describes the variation of the path length to the momentum deviation.

We define the slip factor η as:

$$\frac{df}{f_0} = \eta \frac{dp}{p} \tag{1.14}$$

where f is the revolution frequency and p the momentum. The slip factor η describes the variation of revolution frequency with respect to the momentum deviation.

The following relation can be derived from the previous two definitions:

$$\frac{df}{f_0} = \left(\frac{1}{\gamma^2} - \alpha_c\right) \frac{dp}{p_0} = -\eta\delta \tag{1.15}$$

where γ is the relativistic factor.

α_c is fixed by the optics, *i.e.* the quadrupoles settings, of the machine, therefore there can be an energy during the acceleration process in a synchrotron at which the revolution frequency doesn't depend on the momentum: it is called transition energy (γ_{tr}).

The phase of the RF system is set such as, particles with lower momentum than the synchronous particle would arrive later at the RF system (below transition) and it will see a higher electric field, which increases its momentum towards the synchronous particle momentum. A particle of higher momentum, would arrive later at the RF system, gaining less energy than the synchronous particle and therefore decreasing its momentum deviation. This process, illustrated in Fig. 1.5, make the particles oscillate around the synchronous particle, in a stable bucket (maximum stable phase space area around the synchronous particle), forming a stable bunch in the (E, ϕ) plane. The contour of the bucket is called separatrix.

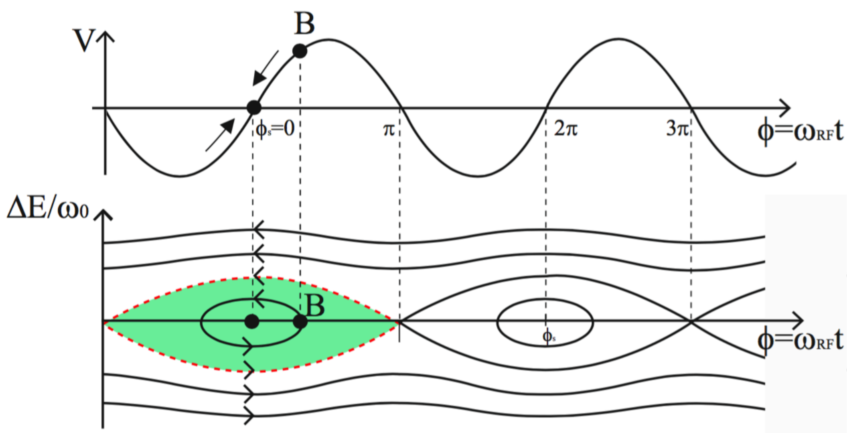

FIGURE 1.5: Top: the RF voltage waveform with a synchronous particle at ϕ_s. Bottom: The particle trajectories in the longitudinal phase space $(\phi, \frac{\Delta E}{\omega_0})$. The maximum stable area (bucket) is indicated in green color. The separatrix is shown with the dashed red contour. The particle B performs a synchrotron oscillation inside the bucket, in this case without acceleration ($\phi_s = 0$) and below transition energy [26].

In Fig. 1.5, the motion of particle B in the longitudinal phase space $(\phi, \frac{\Delta E}{\omega_0})$ is called the synchrotron motion and it can be defined by an angular synchrotron frequency ω_s and a synchrotron tune Q_s (number of synchrotron oscillation per turn), similarly to the transverse motion. The tune can be written as:

$$Q_s = \frac{\omega_s}{\omega_0} = \sqrt{\frac{eVh|\eta|}{2\pi\beta_0^2 E_0}} \tag{1.16}$$

where ω_0 is the angular revolution frequency, e is the electron charge, V is the RF voltage, h if the harmonic number, η the slip factor, β_0 is the relativistic factor, E_0 is the total particle energy.

Typically, the synchrotron tune Q_s is much smaller than the betatronic one. For example, in the CERN PS the synchrotron tune at injection is 0.001 and the betatronic tune 6.1.

The maximum number of bunches circulating in the machine is the same as the harmonic number of the RF system.

An asynchronous particle oscillates between the head (small ϕ) and the tail (large ϕ) of the bunch around the synchronous particle. This motion is very important for the coupling between space charge and the betatronic resonances.

1.3 Betatronic resonances

Using the Hamiltonian formalism, the general resonance condition can be written as [24]:

$$mQ_x + nQ_y = l \tag{1.17}$$

where m, n and l any three integers, and $N = |m| + |n|$ is the order of the resonance. For example, let's consider the case where $m = 1, n = 0$, and l an integer. In an ideal case, a particle with tune $Q_x = l$ would be stable. However, in practice every accelerator has small errors in the linear magnetic fields (dipolar and quadrupolar), error of alignment of the magnets and additional non-linear magnetic fields. When a particle has a horizontal tune equal to an integer and there is a magnetic dipolar error at a longitudinal position s, the particle comes at this position with exactly the same betatronic phase every turn. Therefore at each turn it accumulates the dipolar error as an angular displacement, growing its horizontal amplitude until it hits the physical aperture and gets lost. However, if this particle has a half-integer tune, two consecutive crossings at the position s will have opposite betatronic phases, therefore the error compensate the perturbation of the previous turn and the amplitude will, on average, remain the same. This simple example was for an one dimensional resonance, but the same principle applies to coupled resonances and higher order resonances. A N-multipolar error drives a resonance of order N, for example a quadrupole ($N = 4$) drives a resonance of order 4 ($|n| + |m| = 4$).

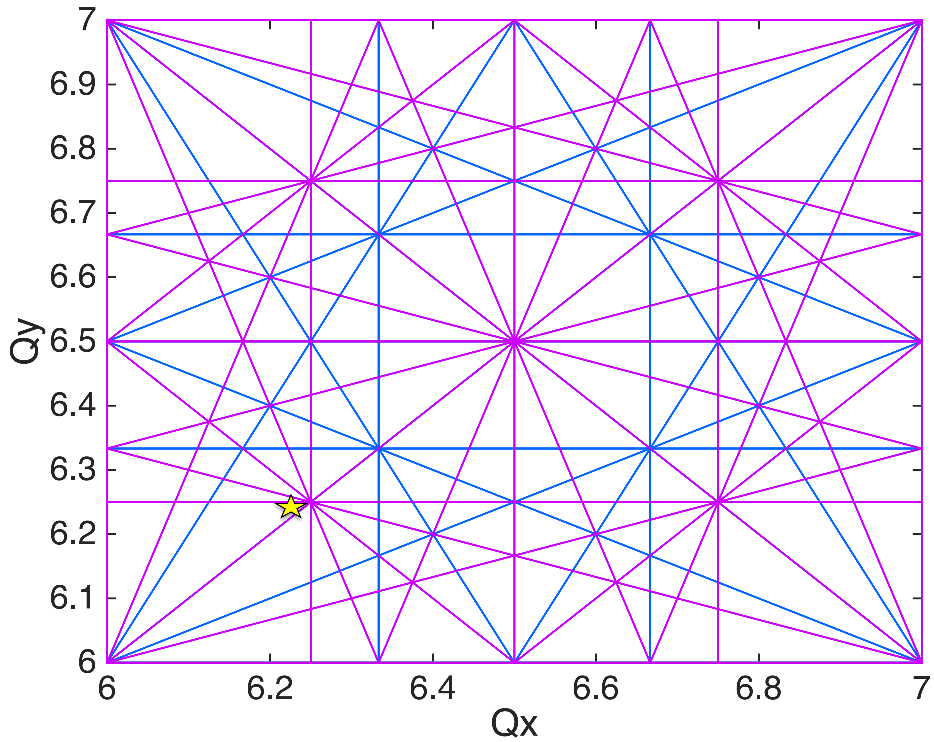

FIGURE 1.6: Tune diagram, the horizontal axis represents the horizontal tune, the vertical axis represents the vertical tune. The lines are the resonance lines up to the 4^{th} order. Application to the PS with integer tunes (6,6), the yellow star is a typical LHC beam working point.

Given the resonance condition in Eq. 1.17, we define the working point as the pair (Q_x, Q_y) and a tune diagram as the diagram where the horizontal axis represents the horizontal tune and the vertical axis represents the vertical tune Fig. 1.6. The resonance condition translate into the lines drawn $(mQ_x + nQ_y = l)$, imposing restrictions on the working point choice.

For a resonance of order N, if n (the vertical coefficient) is even then it is associated to a normal resonance. While if n is odd, the resonance is a skew resonance (driven by a skew N-multipole).

A stable particle has an elliptic motion in the phase space (z, z'), while in the case of a resonance, the phase space is distorted and shows a specific topology depending on many parameters and mainly the resonance order. For a resonance of order N, the phase space shows an N-gon (polygon of N sides). Depending on the detuning with amplitude due to high order magnetic components, N island structures could form around the N-gon. An illustration is given Fig. 1.7, where a sextupole is excited (N=3) and the tune is very close to the resonance line $3q_z = 1$, with q_z being the fractional part of Q_z. The phase space shows a clear triangular (3-gon) shape. and in the cases where there is an additional octupolar component, 3 islands appear. It is important to note that the topolgy doesn't change depending on the parameters (distance to the resonance, sextupole strength...etc), it only depends on the order of the resonance, while the exact shape depends on many parameters like the distance to the resonance ($|nq_x + mq_y - 1|$), the sextupole strength, the other multipoles...etc. In Fig. 1.7, the resonance deforms the trajectory of the particle, increasing its maximum amplitude and that's why resonances may cause beam loss and emittance growth.

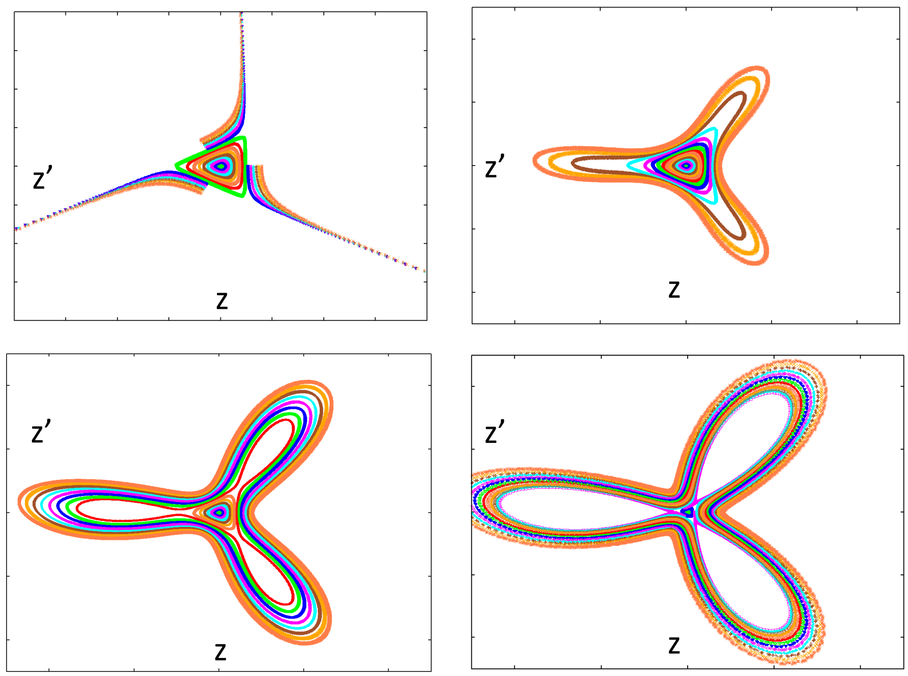

FIGURE 1.7: Phase space topology of a third order resonance in 4 different cases. 1^{st} case (upper left): Only sextupolar error included, no higher orders. 2^{nd} case (upper right): a sextupolar plus an octupolar errors are included, no higher orders. 3^{rd} case (lower left): same as 2^{nd} case with smaller distance to the resonance. 4^{th} case (lower right): same as 3^{rd} case with even smaller distance to the resonance.

1.4 Space charge effects

Space charge is one of the most important collective effects, especially for low energy machines. Space charge effects are divided into two categories, direct and indirect. The direct space charge effects are due to the fields generated by the beam itself. While the indirect effects, also called image effect, are due to the image charges formed at the surface of the beam pipe. In this thesis we focus only on the direct space charge effects, as the beam pipe of the CERN PS is very large compared to the beam size and therefore the effect of the image charges is not significant for the following studies.

1.4.1 Direct space charge effects

Let's consider a bunch of particles of the same charge stored in an accelerator. In a moving frame, centered on the bunch, the particles repel each other due to Coulomb forces. While, in the laboratory frame, the moving particles form a parallel currents that attract each other. These two dynamics act against each other. At low speed (energy) the Coulomb forces are dominant and therefore the effect of space charge is very important, and it become less significant as the energy is increased.

It is easy to conceive that the self field generated by the beam depends on the particle distribution. Fig. 1.8 shows the electromagnetic force versus the transverse displacement x (horizontal or vertical) for the case of a quadrupole, space charge with a uniform transverse distribution and space charge with a Gaussian transverse distribution. Since most of the beams have Gaussian transverse particle distribution, all the following analysis assumes that the transverse distribution is Gaussian.

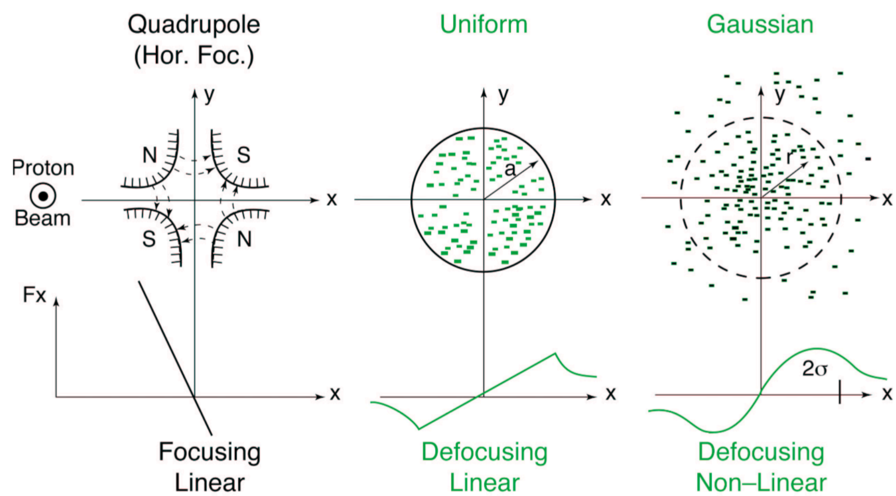

FIGURE 1.8: The electromagnetic force versus the transverse displacement x (horizontal or vertical) for the case of a quadrupole (left), space charge with a uniform transverse distribution (middle) and space charge with a Gaussian transverse distribution (right) [27].

If we consider a beam with a Gaussian distribution, particles will experience a different space charge depending on their transverse and longitudinal positions, inducing a tune spread among the particles due to the quadrupolar component of the space charge field. The small-amplitude particles of the beam are the most detuned by the space charge. This analysis is usually performed in the transverse plane (2D), then the longitudinal position of the particle influences is used to scale the space charge force by the local particle density. In other terms, we slice the bunch longitudinally into several slices, each slice has its own local particle density but all of them have the same transverse distribution, the space charge can be considered in a 2D transverse frame and simply scaled by the longitudinal line density of the bunch Fig. 1.9.

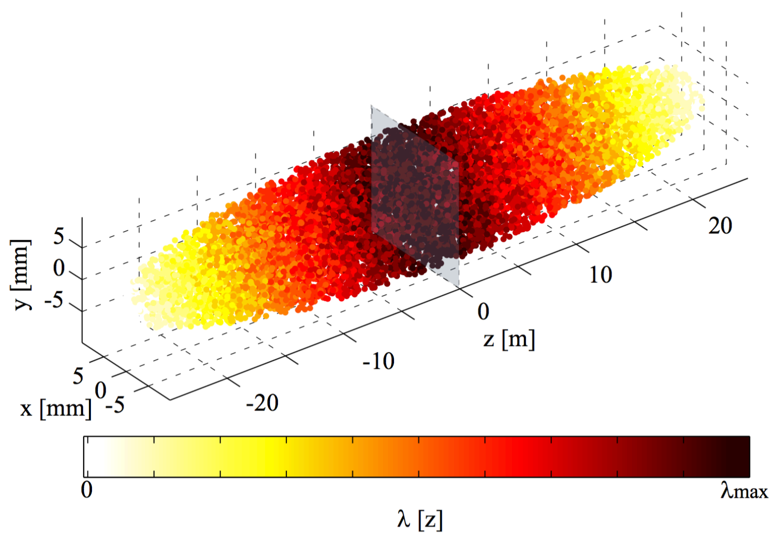

FIGURE 1.9: 3D representation of the bunch, where s and y are the transverse horizontal and vertical coordinates. z is the longitudinal coordinate and λ is the longitudinal line charge density along the bunch, represented as the color-scale.

The tune spread due to space charge has the shape of a necktie, as in Fig. 1.10. The core of the beam (small amplitude particles) are at lowest part of this necktie as they get detuned the most with respect to the zero-current tune. The large amplitude particles get detuned the least and are at the higher part of the necktie.

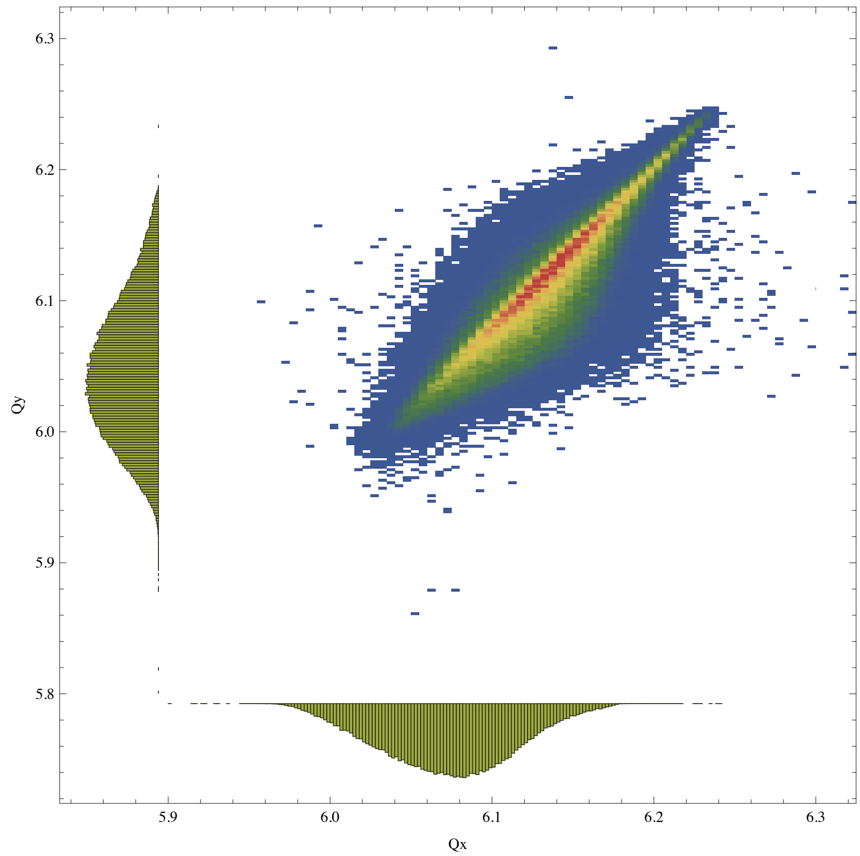

FIGURE 1.10: Space charge necktie (tune-spread) for a Gaussian beam. The horizontal axis is the horizontal tune, the vertical axis is the vertical tune and the colorscale reprents that particle density.

The space charge necktie represents a static picture of the tune spread. Particles move longitudinally under the synchrotron motion, therefore they experience different strength of the space charge forces depending on the local density at their longitudinal position. Therefore, particles oscillate as well in the necktie due to the synchrotron motion. A detailed study of these oscillations can be found in [26].

Since space charge induces a tune-spread as in Fig. 1.10, we introduce the concept of zero-current working point (Q_x, Q_y) which correspond to the working point without space charge (at zero intensity). The choice of the zero-current working point becomes dependent on the space charge, in order for the necktie to avoid overlapping resonances or at least minimize the effects of the overlapped ones.

1.4.2 Resonance crossing for a space charge dominated beam

In previous studies [8] [28] [29], it has been shown that a resonance crossing for space charge dominated beams can be divided into two regimes. The first regime is when the lower part (small amplitude particles) of the necktie overlaps the resonance. Given the synchrotron motion, the small amplitude particles cross repeatedly the resonance as they move in the necktie, causing the growth of their amplitude and consequently the beam's emittance growth. On the other hand, the second regime is when the higher part (large amplitude particles) of the necktie overlaps the resonance. For the same reason of synchrotron modulation, the large amplitude particles cross repeatedly the resonance causing their amplitude growth and eventually hitting the beam pipe and causing beam loss.

The mechanism of amplitude growth due to resonance crossing was explained by the "resonance trapping mechanism" [10]. In a very brief and schematic representation, when a particle is in a resonance island and it moves longitudinally due to the synchrotron motion, the island position moves due to the detuning (caused by the change of space charge forces as seen previously). This island shift, if done at a certain "speed", it can trap the particle inside the island, leading to its amplitude growth. The resonance trapping mechanism, can explain the emittance growth and beam-loss due to the overlap of the necktie and betatronic resonances.

Another important concept is the asymmetric crossing of a resonance. The effects of a resonance crossing in one direction, is not the same as the crossing in the opposite direction. For example, if the $3Q_y = 19$ is a harmful resonance and increasing the working point from 6.3 to 6.66 will not have the same effect as decreasing the working point down from 6.66 to 6.3. This is because of the direction of the movement of the resonance islands. When the space charge induces a tune spread, the lowest particles (the most detuned) are the small amplitude particles, so when the zero-current tune increases, the space charge necktie overlap the resonance with particles with smaller amplitude and therefore the resonance islands appear at smaller amplitude. Fig. 1.11 is an illustration of this effect, where a one dimensional vertical resonance was considered for simplicity. When the zero-current working point is higher (blue necktie), the detuning with amplitude is higher (blue line) and therefore the intersection with resonance is at a lower vertical amplitude (J_y). This illustration is static, if we imagine a dynamic scenario where the green line moves up until it reaches the blue line, we will find out that the islands amplitude (intersection of the detuning with amplitude and the resonance line) decreases, and vice versa.

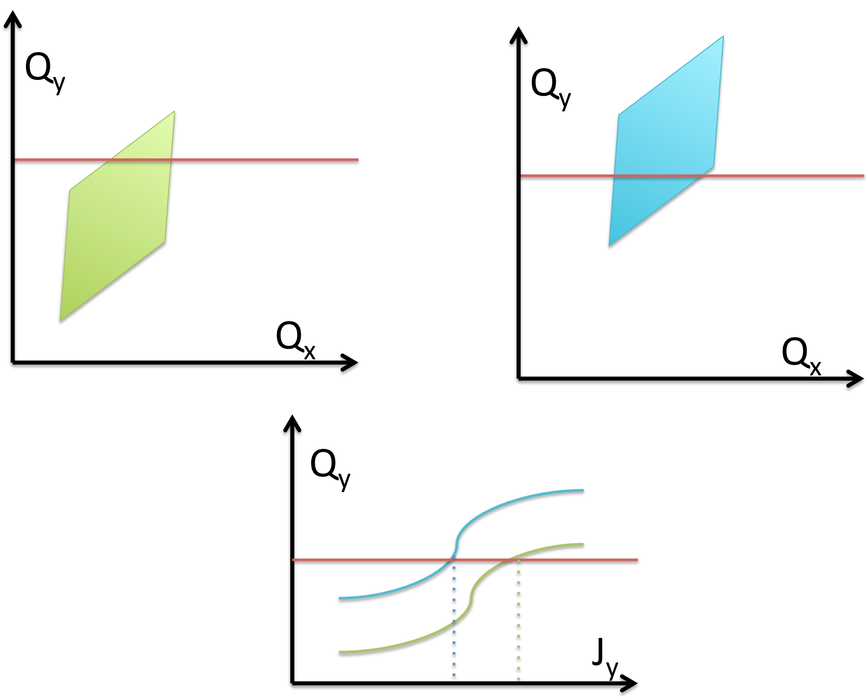

FIGURE 1.11: An illustration of the island amplitude dependence on the working point position. Top left: the space charge necktie (green) overlaps the resonance (red). Top right: the space charge necktie (blue) overlaps the resonance (red) with the a lower part (smaller amplitude particles) than the left case. Bottom: a schematic view of the tune (Q_y) as function of the vertical amplitude (J_y) for both cases, the blue curve corresponds to the blue necktie and the green curve corresponds to the green necktie. Note that the shape of the detuning with amplitude is not correct, it is just a schematic representation for a global understanding.

1.5 The CERN PS

The CERN PS was commissioned in 1959 and it was considered as a great achievement since the PS is the first alternating-gradient accelerator to be built and commissioned. For nearly 60 years, the PS has been accelerating and decelerating beams of protons, ions, antiprotons and electrons, serving many other machines like the Intersecting Storage Rings (ISR), the Large Electron Positron (LEP) and the Large Hadron Collider (LHC). Currently, the PS is part of the LHC injector chain, it accelerate protons and ions and deliver them to the SPS. The PS is also currently serving other experiments like the Antiproton Decelerator (AD), the Neutron Time Of Flight (nTOF) and the EAST ones. This section is an overview of the main characteristics and parameters of the CERN PS, especially those discussed later in this thesis. A detailed description of the machine can be found in the two reports [30] [31].

1.5.1 The PS lattice structure and magnets

The PS lattice is composed of 100 combined function main magnets, separated by 100 straight sections. Each magnet is composed of 10 blocks, divided into two half-units of 5 blocks each, focusing and defocussing. Leading to the lattice structure of the PS: “FOFDOD” (Fig. 1.12). In addition to the main magnets, other tuning elements are inserted in the straight sections, such as injection, extraction, accelerating cavities, auxiliary magnets and diagnostics equipments.

The straight sections do not have different lengths, breaking the 50 fold symmetry ($50 \times FOFDOD$) into 10 super-period.

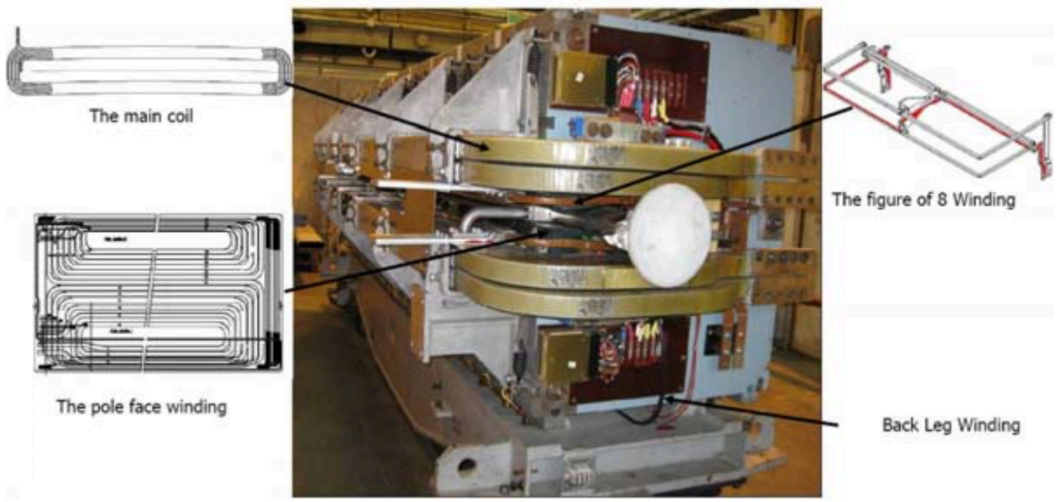

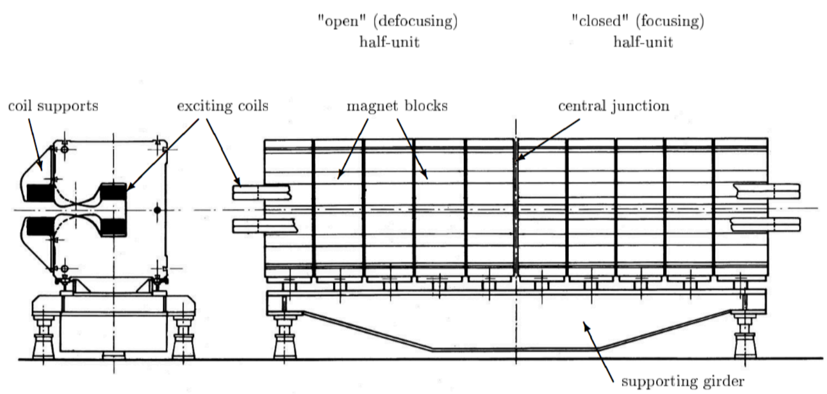

FIGURE 1.12: Top: Picture of the PS main magnet and drawings of the PFW, the F8L and the main coil [30]. Bottom: drawing of the main magnets showing the 10 blocks, the two half-units and a cross section. [17]

Fig. 1.13 shows the cross section of a main magnet. The magnet is powered through the main coil and is intended to provide the required dipolar component for the bending and the quadrupolar component necessary for the focusing. Additional circuits were added in order to give more degrees of freedom and tuning to the machine. Four of these circuits are located on top of the magnet poles, therefore called Pole Face Windings (PFW), and another circuit in the shape of the number eight, called the Figure of Eight Loop (F8L) Fig. 1.13.

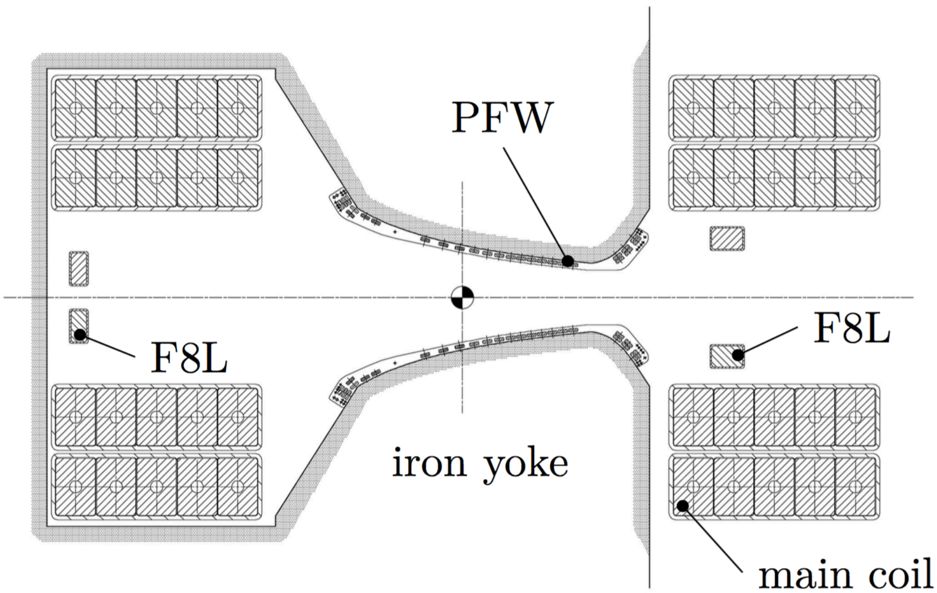

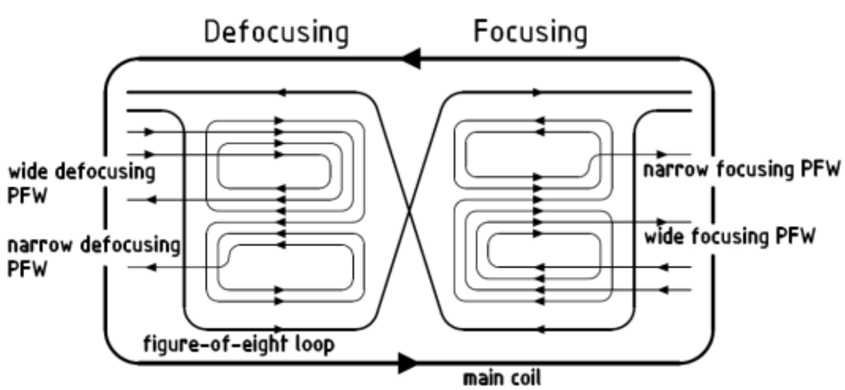

FIGURE 1.13: Top: cross section of the main magnet of the PS. The reference point between the two poles corresponds to the location of the closed orbit. The circuits of the PFW are situated directly on top of the poles. The F8L circuit is located between the main coils as shown above. Bottom: schematic up-down view of the PFW and F8L [17].

The PFW are divided into narrow and wide circuits (Fig. 1.13), where narrow and wide refer to the size of the gap between the magnet poles where each circuit is. There are in total 4 PFW circuits and 1 circuit of the F8L, allowing the control of 5 physical parameters. They are used to control both transverse tunes, both transverse linear chromaticities and one of the two transverse second order chromaticity. These circuits may induce also large undesired non-linear field components, leading to resonance excitation or beam instability. An extensive study of the control of the 5 parameters [4] was performed and resulted in a series of matrices that give the 5 currents as function of the variation of tunes and chromaticities. These matrices are for different settings such as 5×5 mode: controlling the 5 parameters, 4×4 mode: controlling only tunes and linear chromaticities, 3×3 mode: controlling tunes and one chromaticity while keeping the narrow and wide circuits with the same currents, each setting has its own advantages and reliability level. It is important to note that these matrices are measured for small variations of the each of the parameters and they are a local linear approximation to a non-linear function. For large changes of the parameters, the simulated matrices [17] might be more accurate, even though they also need an initial measured benchmark at the new parameter level.

In addition to the PFW and F8L which are distributed all along the machine, 40 Low Energy Quadrupoles (LEQ) are installed in the straight sections in order to control both transverse tunes at the injection energy and up to 3.5 GeV. It is interesting to note that the LEQ positions do not show any symmetry in the machine, introducing a perturbation to the 10 fold structure symmetry of the PS.

Besides this high level of transverse flexibility given by the PFW, the F8L and the LEQ, the PS has also a very sophisticated RF system making the PS the main longitudinal shaper in the LHC complex. The PS performs several bunch splitting, merging and rotation for the production of the operational LHC beams. The RF system comprises cavities with frequencies of 10, 20, 40, 80 and 200 MHz.

A cycle is defined as the sequence of events starting by the ramp of the magnets from 0 current, passing by the injection of the beam, until its extraction to the end-user. The PS is called a cycling machine, because it can perform a series of these cycles, serving a series of end-users at the simultaneously. The unit of time of the cycles is called basic period (BP), which correspond to 1.2 s. The length of a cycle is at least 1 BP and it last several BP. The series of cycles is repeated over time and it is called super-cycle. The super-cycle is typically 20-35 BP We define the c-time (or clock-time) is the measure of time inside of a cycle. It is initialized to 0 at the start of each cycle and its unit is ms. For example, an injections at C170 means that the injections happens 170 ms after the start of the cycle.

The PS was the first accelerator to have beams successfully crossing the energy, shortly after its commissioning in 1959. The longitudinal dynamics are quite different below and above the transition energy, for example the stable RF phase is shifted by $\frac{\pi}{2}$. Moreover,

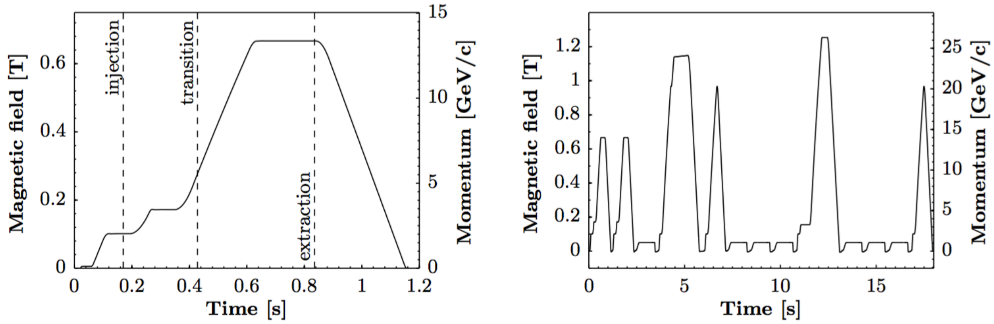

FIGURE 1.14: Left: an example of a PS magnetic cycle. Injection occurs at 170 ms, transition energy is crossed at 428 ms and the beam is extracted at 835 ms. Right: an example of the PS super-cycle, where there are zero cycles (the field is ramped only to 50 Gauss), and end-user cycles (the field is ramped up to the extraction energy) [32].

at transition energy the beams could suffer from a number of undesirable effects like longitudinal instabilities. To avoid these effects a solution was proposed, the “gamma transition jump” [33] which is still currently in use. It consists of changing the periodic optics using fast pulsed quadrupoles in order to modify dynamically the momentum compaction factor η. It allows the beam to cross faster the non-adiabatic regime around the transition energy. This method has proven its efficiency, especially for the high intensity beams that suffer the most of the longitudinal instabilities close to the transition energy [34].

1.5.2 Instrumentation

Beam instrumentation is a key system in an accelerator in order to monitor the operational beams, as well as localizing and debugging any failure and, of course, in order to develop and understand ongoing research. The beam intensity is one of the most important quantities to monitor, it is measured using beam current transformers (BCT) [35] which infers the beam intensity from the current induced by the passage of the beam inside a dedicated measurement coil. Given its simplicity, the measurement can give the intensity every ms. The beam transverse position is measured using electrostatic pickups (PU) [36]. The transverse tune is measured by a based band tune (BBQ) measurement system, which has been developed at CERN [37]. The beam is kicked in the transverse direction, then the position of the beam centroid is measured by a sensitive PU turn-by-turn, generating a signal on which a Fast Fourier Transform (FFT) is performed to get the highest amplitude harmonic, which is the tune.

A fundamental beam property is the particle phase space ((x,x') or (y,y')) distribution, which is essential for the space charge, brightness and luminosity computations. We are unable to measure the full phase space distribution. However, we can measure its projection on the geometrical axes (x, y, s), which can be used to deduce the phase space distributions. In the transverse planes, the beam wire scanners (BSW) Fig. 1.15 measures the beam profile by flipping a carbon wire though the circulating beam in the horizontal or vertical direction to create secondary particles that are detected by scintillators plus photomultipliers [30]. In the PS, it is possible to flip the wire twice during a cycle, once in the "in-direction" and once in the "out-direction". The measurement limitation comes from the fragility of the system and that it takes about 2 ms to measure the beam profile when rotating the wire at about $20\,m/s$. This speed is considered extremely fast for a mechanical system but quite slow for this measurement since the beam performs about $1,000$ turns during this measurement. The measurement gives therefore an average of the beam distribution over the 2 ms.

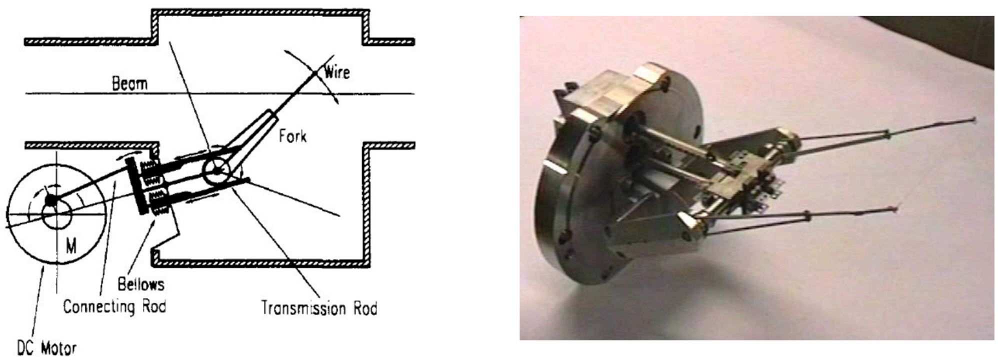

FIGURE 1.15: Schematics of the wire scanner system (left) and a photo of the device (right) [30].

On the other hand, a wall current monitor (WCM) [36] is a pick-up that measures the longitudinal charge density profile turn-by-turn. By using the turn-by-turn data and the well known synchrotron motion theory, a tomographic reconstruction algorithm is applied in order to reconstruct the longitudinal phase space [38].

1.5.3 The LHC beam production scheme

The LHC beam production cycle is 3 BP (3.6 s) long. It features a double batch injection from the PS Booster (PSB), being two injections separated by 1 BP, as illustrated in Fig. 1.16. The first batch contains 4 bunches and there are 2 bunches in the second batch. The bunches are injected at the kinetic energy of 1.4 GeV, the first batch is stored for 1.2 s, then shortly after the second injection the RF system performs a triple splitting, increasing the harmonic from 7 to 21, producing 18 bunches. The bunches are then accelerated to the top-energy of 26 GeV/c, crossing the transition energy. At flat-top, the 20 MHz RF system performs a double splitting and then the 40 MHz system performs a second double splitting to reach a total of 72 Bunches in harmonic 84 seperated by 25 ms. Finally, a bunch rotation is performed by the 80 MHz system briefly before the bunches are sent to Super Proton Synchrotron (SPS).

The double batch injection scheme imposes that the first 4 bunches are stored for 1.2 s at injection energies. The large space-charge tune-spread of the very bright beams causes an overlap with a number of machine resonances and this in turn causes emittance growth and beam loss, making the space charge one of the main limitations of the LHC injectors complex.

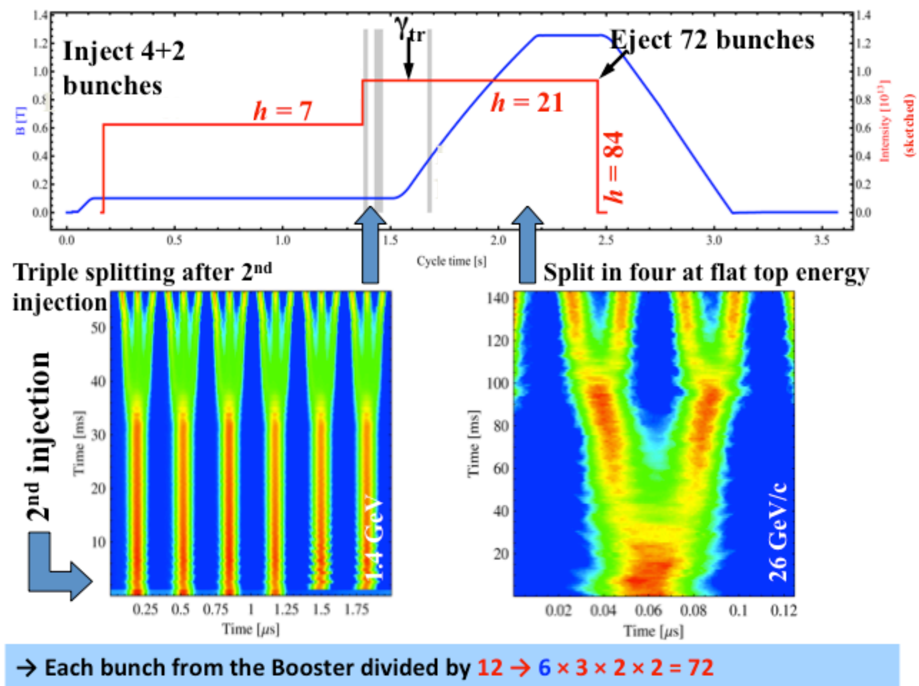

Figure 1.16: LHC cycle in the PS. Top: the magnetic cycles (blue) is ramped up from injection kinetic energy (1.4 GeV) to extraction kinetic energy (26 GeV/c). The cycle features double-batch injection, as it the total intensity (red) reveals. The RF harmonic is changed from 7 to 21, to 42 and finally to 84, splitting each of the injected bunches in 12. Bottom: longitudinal bunch triple splitting (left) and two double splitting (right) [3].

1.6 Simulation Codes

In this work, several simulation codes were used depending on the problem and its parameters. While a general description of these codes is given in this section, for a detailed and specific description please refer to their corresponding references.

PTC-ORBIT [1], pyORBIT [16], IMPACT [15] and MADX-SC [39] have been used as space charge simulation codes in order to study the interplay between space charge and resonances in th PS. Each code presents advantages and limitations, therefore each one was used when it was the most adapted to the phenomenon under study. On the other hand, MADX [40] [41] was used for single particle tracking and optics calculations.

1.6.1 MADX and PTC

The Methodical Accelerator Design (MAD) [39] [41] was developed at CERN in order to design the LHC optics and it has been used to simulate many accelerator lattices worldwide.

An accelerator can be defined as a sequence of elements (magnets, RF cavities, diagnostics devices...etc), then the code can compute the corresponding optics and track particles 6D coordinates. The elements can be defined as thin-lens elements (no longitudinal length), or more realistically as thick elements. The thin-lens approximation make the tracking non-symplectic, but it has been found to be an acceptable approximation [41], unless the magnet bending angle is quite large, so the thin lens approximation is not suitable for small machines (large bending angles). Another alternative is to split thick magnets in several thin lens elements, which is a better approximation but it increases the tracking time.

MADX is the 10^{th} version of MAD, which include an impeded of the Polymorphic Tracking Code (PTC) [42], in order to overcome non-symplectic tracking in side of thick elements, which is the main limitation of MAD. In the case of the PS, the particle tracking and optics design is usually made in PTC as the machine is relatively of a small bending radius and the magnets are quite complex. As illustrated in Fig. 1.17, the PS magnet is modeled as 4 thick magnets, 2 magnets representing the focusing half-units and 2 magnets representing the defocusing half-units. Thin multipoles were added before and after each magnet in order to model the PFW and F8L. They are powered such that the chromaticities (up to the 2^{nd} order) match the measured one.

In this thesis, all the lattice optimization and optics changes were performed using the PTC embedded in MADX, which proved to be very close to measured values.

1.6.2 PTC-ORBIT and pyORBIT

PTC-ORBIT [1] has been the CERN baseline space charge code since 2011. It is the merger of two well known and benchmarked codes, PTC [42] and ORBIT [43]. As seen in the previous section, PTC

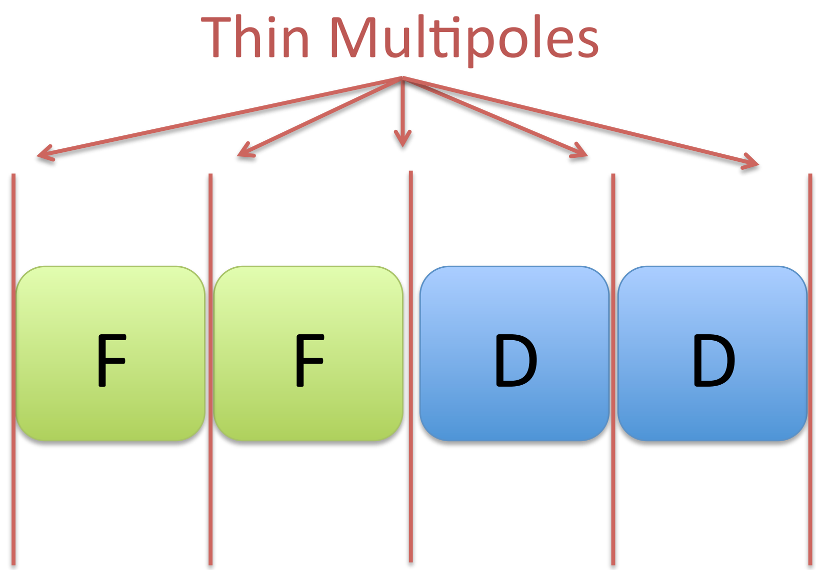

FIGURE 1.17: Schematics of the modeling of one of the main PS magnet in MADX.

is used for the optics calculations and single particle tracking while ORBIT is used for multi-particle calculations like space charge and impedance.

In order to perform a space charge simulation, the machine lattice is defined as in MADX or in PTC, then space charge nodes are introduced between these nodes respecting certain rules (a maximum distance between 2 consecutive space charge nodes, maximum integrated gradient between 2 consecutive nodes...etc). The ensemble of the MADX lattice and space charge nodes constitute the new machine representation for PTC-ORBIT. PTC-ORBIT allows the possibility of simulating time-varying fields and components through control tables, where elements can be varied throughout the simulation. Once these tables are defined, the tracking starts. In order to simulate space charge, a multi-particle beam is tracked around the machine. The tracked beam consists of a number n of "macro-particles", a macro-particle represents $\frac{N}{n}$ particles (N being the number of real particles). The number of macro-particles chosen is a compromise between computing time and realistic representation of the space charge.

The code is parallelized, and since the single particle tracking is completely independent from particle to particle, the single particle tracking is parallelized on several processors (typically 32-48). Once particles reach a space charge node, all particles coordinates are gathered on one processor, where the space charge kick is calculated and applied to each particle. Then the particles are distributed again between different processors to be tracked trough PTC elements until the following space charge node where the same procedure as at the previous space charge node is performed. This process is carried out until completion of the desired number of turns.

As it can be noticed, this process mixes between fully-parallel tracking (PTC) and single processor calculations for the space charge kick (ORBIT). The mixture between these two processes, sets a maximum optimal number of processors above which the parallelization wouldn't speed up the process. This effect is due to the interplay between single processor computation time and inter-processors communication time. The maximum optimal number of processors depends on the speed of the processors, the speed of the communication between them and the architecture of the problem, *i.e.* the geometry and particle distribution. Therefore, a set of simulation has to be launched to determine the maximum optimal number of processors for each combination of cluster and problem architecture. Then, the optimal number effectively used for simulations might be lower depending on the number of simulations to be launched and the available number of processors.

In general, space charge could be computed in a full-3D mode (x, y, s), where all 3D effects are taken into account, but in ORBIT the effects are computed separately in transverse and longitudinal planes. This approximation is valid as the longitudinal effects are negligible compared to the transverse ones.

In general there are 5 types of transverse space charge kick possible models or calculation techniques:

- Pair-wise sum : simple sum of the Coulomb forces on each particle caused by each of the other macro-particles.
- Brute-force Particle-In-Cell (PIC): the macro-particles are binned in a 2D mesh divided in $N_{bin,x} \times N_{bin,y}$ in the (x, y) plane, then the space charge force is computed on each node if the grid, then the force is interpolated to be applied on each macro-particle (Fig. 1.18).
- Fast Fourier Transform (FFT) Particle-In-Cell: similar procedure as the Brute-force PIC except that the force is calculated on the grid nodes using a FFT method (Fig. 1.18).
- LU decomposition: the Poisson equation is written as $A\Phi = b$ (being A and Φ two matrices and b a vector), then it is solved

using the decomposition of A into $L \times U$ (L a lower triangular matrix and U an upper triangular matrix).

- Successive Over Relaxation (SOR) iterative: the Poisson equation is written as $A\Phi = b$ (being A and Φ two matrices and b a vector), then it is solved using the decomposition of A into $D+L+U$ (L a strictly lower triangular matrix and U a strictly upper triangular matrix and D a diagonal matrix).

Only the first 3 methods are included in ORBIT. The Pair-wise sum requires n^2 operations to calculate the kick, making it the slowest method. It is recommended as occasional benchmark rather than a simulation routine.

Although the Brute-force PIC routine requires ${N_{bin,x}}^2 \times {N_{bin,y}}^2$ operations, making it faster than the pair-wise sum, the FFT PIC routine is more often used since it is very similar and faster (only $2\sqrt{N_{bin,x}N_{bin,y}}$ $log(\sqrt{N_{bin,x}N_{bin,y}})$). The FFT PIC is similar to the Brute-force PIC, except that the force is calculated on the grid nodes using a FFT method. The force is computed on the grid nodes by solving the Poisson equation which can be written in the differential form as:

$$\nabla^2\Phi = \frac{\rho}{\epsilon_0\gamma^2} \tag{1.18}$$

where Φ is the electric potential, γ is the relativistic factor, ρ is the charge density, ϵ_0 is the vacuum permittivity.

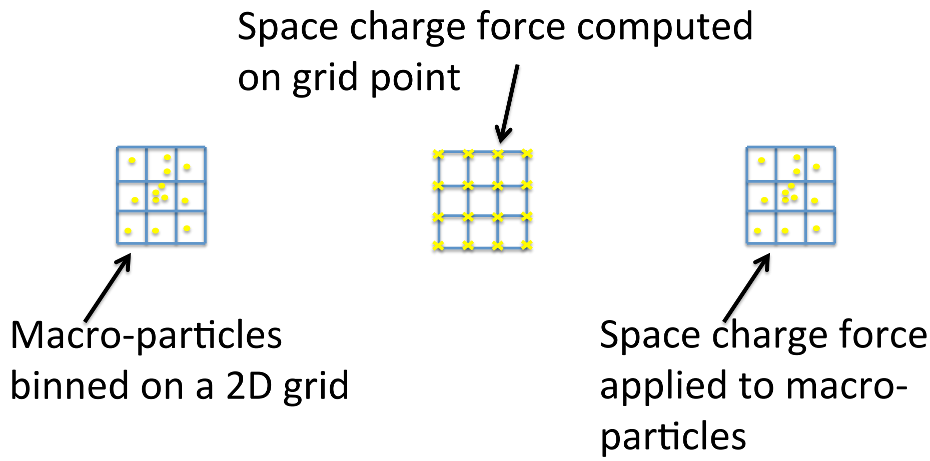

Figure 1.18: Illustration of space charge kicks computation using the Particle-In-Cell method. For the Brute-for PIC case, the second step is done by summing the Coulomb forces. For the FFT PIC case, the force is computed with an FFT method.

In ORBIT, there are 2 modes of transverse space charge kick calculation, the 2 D and 2.5 D models. In the 2 D calculations, all particles are projected on the same transverse plane, where the kick is calculated, then the space charge is scaled with respect to the local longitudinal line density. On the other hand, for the 2.5 D the bunch is longitudinally divided in several slices. Each slice is projected in one transverse plane, where space charge is computed and applied. The 2.5 D mode is useful in case of change of the transverse distribution along s as for bunched beams, in which case projecting all particles in the same transverse plane would neglect this effect.

When computing the space charge kick, if the boundary conditions are imposed, the computation imposes that the electric field vanishes at the pre-defined boundaries, consequently including the indirect space charge effect. If the boundary instead are not considered, the field is computed with “infinite boundaries”, consequently taking into account only the direct space charge effects.

Recent developments of PTC-ORBIT included the change to a new python interface and the re-implementation of several modules as well as the introduction of the “frozen space charge” [8] module, giving birth to pyORBIT. In PTC-ORBIT, the space charge kick is computed at every space charge node, explaining its definition as ”self-consistent” space charge simulation. On the other hand, a “frozen space charge” module is when the space charge kick is computed only once and then the same kick is applied to the beam at each passage till the end of the simulation. Since the kick is computed only once, it is reasonable to compute an analytical solution (more accurate but much slower) and apply it to the beam. Such a frozen module is considerably faster than a self-consistent code because it requires the tracking of almost 2 order of magnitude less macro-particles ($\sim 1,000$ instead of $\sim 100,000$), since the kick is computed analytically with a large number of particles ($\sim 100,000$) once then the same kick is applied on fewer tracked particles ($\sim 1,000$).

In the case of the self-consistent simulations, a convergence study is needed at the beginning of each set of simulations in order to determine the optimal parameters, like the number of macro-particles, the binning of the transverse space charge grid, the binning of the longitudinal slicing, the number of space charge nodes per turn, etc.

Typically, we choose a case where no emittance growth is expected to be seen, for example a very low brightness beam, then run simulations with different parameters and we choose the fastest set of parameters that doesn't show any artificial emittance growth (noise) which would be induced by the PIC binning [44][45]. In the case of the frozen space charge module, the space charge kick is computed using a large number of macro-particles ($\sim 250,000$) then only few thousand particles are tracked in order to see the emittance growth and beam loss.

For the PS, the gain in terms of speed is impressive. $\sim 1,000$ turns require $\sim 1\,day$ for the self-consistent case, while it only takes $\sim 2\,min$ for the frozen model. We have to note that these figures are for order of magnitude, they may vary depending on the beam parameters. Additionally, the precision of the beam loss and emittance growth is reduced by the small number of macro-particles (1000), but it could be easily compensated by using ore processors since frozen space charge simulations are highly scalable, in other terms the use of more processors can compensate the loss of speed due to a larger number of macro-particles.

1.6.3 IMPACT

The Integrated Map and Particle Tracking Code (IMPACT) [15] code has been developed at LBNL. It is a space charge code, where the tracking part is similar to MADX, consequently only thin lens elements are used in order to keep a symplectic tracking. The space charge module uses a PIC method in order to compute the space charge kicks. The general structure is similar to PTC-ORBIT, space charge nodes are placed between the tracking elements. Particles are tracked trough the regular lattice untill they reach the space charge node, where a space charge kick is computed and applied to the particles. In IMPACT, the space charge module has been implemented in parallelized scheme, which means that the tracking and the space charge module computations split and performed simultaneously on several processors, allowing the simulation of a full 3D space charge module within a very reasonable time ($\sim 90,000\, turns/day$). The space charge module has also a boundary conditions flag allowing to include the indirect space charge if needed.

1.6.4 MADX-SC

Recent development of MADX have led to the implementation and integration of a frozen space charge module, sometimes referred to as MADX-SC [39]. The principle is the same as previously explained, where space charge nodes are introduced between the elements, particles are tracked through regular elements and a space charge kick is applied when the particles reach the space charge node. The fact it is a frozen space charge module means that the kick is computed analytically and that the number of tracked macro-particles can be as few as $\sim 1,000$ macro-particles, allowing for faster simulations. However, MADX has not been fully parallelized.

1.6.5 Summary table

In the following table the summary of the main characteristics of each code.

Parameters	PTC-ORBIT/pyORBIT (self consistent)	pyORBIT (frozen)	IMPACT	MADX-SC
Speed for the PS lattice (turns/day)	$\sim 1,000$	$720,000$	$\sim 90,000$	$\sim 50,000$
Number of tracked macro-particles	$\sim 250,000$	$\sim 1,000$	$\sim 100,000$	$\sim 1,000$
Number of processors used	~ 48	~ 48	~ 256	~ 4
Indirect space charge effects	possible	not possible	possible	not possible
Space charge module	2 D / 2.5 D	analytical	3 D	analytical
Scalability with number of processors	limited (optimal ~ 48)	very high (scales with larger number of macro-particles)	limited (optimal ~ 256)	very limited (only one node)

Table 1.1: Summary of simulation codes characteristics.

Chapter 2

Current limitations for high beam-brightness

2.1 Space Charge at injection at the CERN PS

The production of the LHC beams in the CERN Proton Synchrotron (PS) features a double batch injection scheme as shown in Fig. 2.1, as explained in section Sect.1.5 the two injections occurring at an interval of 1.2 s during the 1.4 GeV (kinetic energy) flat-bottom. This long waiting time on the injection plateau causes one of the main limitations for high brightness beams, due to the fact that for large betatronic tune-spreads induced by direct space charge, particles can cross deleterious resonances many times due to large $\Delta p/p$, large ξ in both planes and many synchrotron periods.

A study of the betatronic resonances [4] has shown the most dangerous ones. Fig. 2.2 shows beam losses versus working point, the horizontal axis is the horizontal single particle tune while the vertical one is the

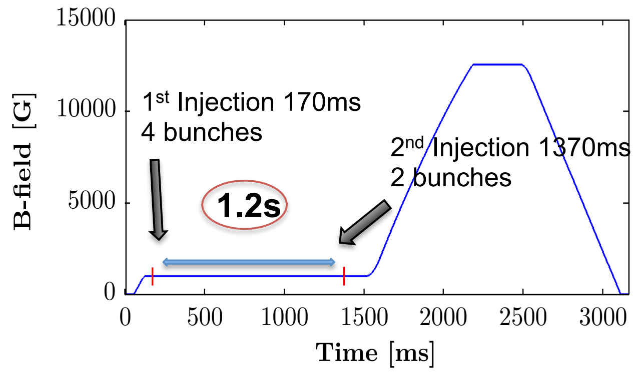

FIGURE 2.1: LHC magnetic cycle, featuring 2 injections, seperated by 1.2 s.

single particle vertical tune and the color-scale represents the beam-loss. A beam with a large transverse size and low brightness, to avoid too large non-chromatic tune spreads, was used to cross the resonances, which were identified by beam losses. It can be concluded from Fig. 2.2 that the PS lattice features a strong skew sextupolar component exciting the $2\,Q_x{+}Q_y$ and $3\,Q_y$ resonances. The normal sexupolar resonances seem to be less excited but still present, as the $Q_x{+}2\,Q_y$ resonance is excited.

The current operational working points for the LHC-type beams are within the area Q_x=[6.1 : 6.24] and Q_y=[6.1 : 6.245], as illustrated in Fig. 2.2, to avoid resonances. Head-tail instabilities are dumped by using the transverse coupling introduced by the Q_x-Q_y resonance [46], in addition to linear coupling from skew quadrupoles. The typical detuning due to direct space charge of the nominal LHC type beams is about -0.2 in the horizontal plane and -0.28 in the vertical one [46], which means that the tune footprint is very close and sometimes even overlaps the integer resonances. Moreover, the High Luminosity LHC beam parameters [47] require an even larger detuning, with an

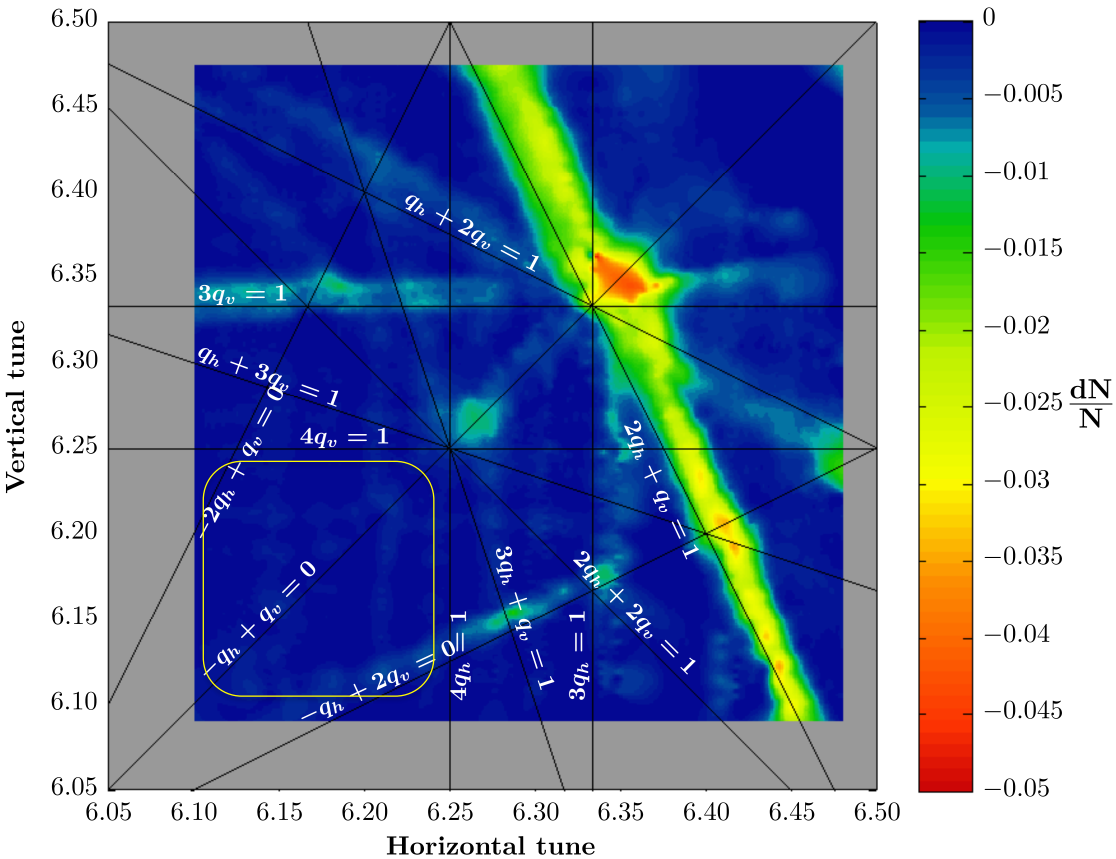

FIGURE 2.2: Tune loss map. The color code indicates the amplitude of the beam loss. The LHC beam operational working point area is identified by the yellow rectangle [4].

allocated budget for maximum beam loss and transverse emittance growth for the PS of only 5% each.

Therefore a study of the effect of direct interaction of space charge dominated beams with resonances is necessary, especially considering the effect of different tune-spreads due to space charge since the PS operates beams with a large spectrum of parameters.

2.2 Previous study

In a previous study [5] done for the preparation of the PS as LHC injector, the effect of space charge dominated beams and resonances was studied with respect to the working point and the maximum tune-spread due to space charge. In the left figure of Fig. 2.3, the two curves are for 2 different working points (6.22 ; 6.22) and (6.22 ; 6.28). The emittance growth is exponential-like with respect to the maximum tune-spread, while the change of working point delays the growth almost linearly. The right figure of Fig. 2.3 shows the time-evolution along the constant energy magnetic cycle of the relative emittance growth, which shows a slow asymptotic growth.

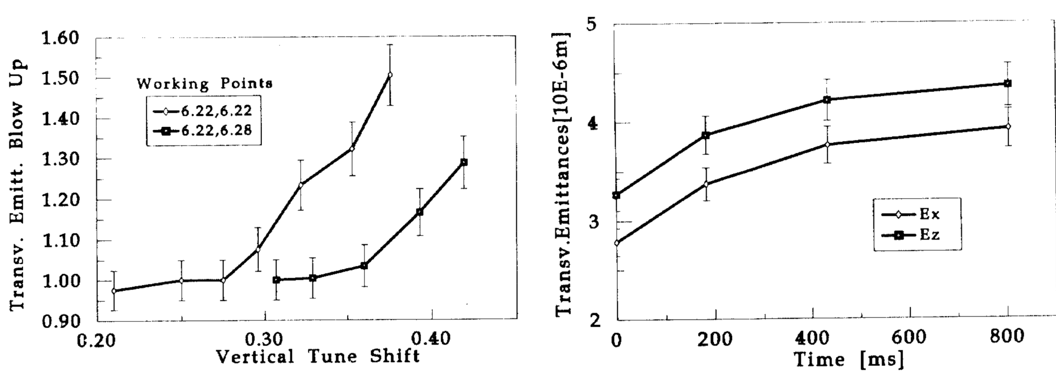

FIGURE 2.3: Emittance growth with respect to maximum tune shift due to space charge (left), emittance growth with respect to storage time (right), as published in 1993 [5]

From Fig. 2.3, the left figure indicates that the 5% emittance growth budget would be reached for a tune-shift of 0.33-0.35, but no beam loss was indicated. It is interesting to know if the machine is behaving in the same way nearly 20 years later and understand the mechanics and details of the limitations, therefore a similar study was conducted in 2013.

2.3 Measurement technique and observables

Since there are strict limitations on emittance growth and beam-loss for the production of LHC high-brightness beams, it was thought to do a similar study taking into account the current and future requirements in terms of losses, blow-up and beam parameters, in order to understand the limitations and necessary improvements. Such a study is crucial to determine the maximum acceptable tune-spread due to space charge with an experimental approach, including all known and unknown effects, as the beam effectively experience it.

The aim of the study is to measure the emittance blow-up and beam loss for different tune-spreads after 1.2 s at injection energy, representing the same conditions as for the first batch of the LHC beams. Such data will help defining a maximum acceptable tune spread due to direct space charge within a given budget of emittance growth and beam loss.

2.3.1 Emittance measurement

The transverse profiles were measured using a wire-scanner, which averages the beam profile during about 1000 turns. Then, using the optics model ($\beta_{x,y}$(s) and D_x(s)) of the machine at the locations of the wire-scanners, emittances could be derived from the beam profiles.

Only one wire-scanner measurement can be taken per cycle. For a better statistics, each case was measured 10 times, which means one emittance measurement in 10 cycles. Therefore the reproducibility of the beam was very important to reduce the statistical error. There might be an uncertainty on the absolute value of the emittance because of an error on the assumed optics functions (β and D_x) at the location of the wire scanner. This systematic error is not of a significant importance in this study as the aim of the study is to observe relative emittance growth and not the absolute values.

2.3.2 Varying the maximum detuning due to space charge

The bunch was compressed adiabatically in the longitudinal plane during 20 ms after injection (see Fig. 2.4) using a ramp of the RF voltage of the main 10 MHz RF system to vary the space charge forces. Then the beam is stored for 1.2 s at 1.4 GeV kinetic energy. Depending on the maximum voltage of the bunch compression (up to 200 kV), beams could have different space charge maximum detuning.

As shown in Fig. 2.4, the beam is injected at ctime 170 ms then 20 ms later it is compressed during 20 ms. The first measurement is done at ctime 220 ms from the start and a second one at ctime 1420 ms, corresponding to 1.2 s between the initial and final measurements.

The measurements were done with a single bunch beam with the parameters as given in Tab. 2.1.

The direct space charge forces are quantified using the maximum detuning due to space charge, which is estimated for the different beams according to the following equations [27]:

Parameters	Value
Intensity [10^{10} ppb]	~ 115
ϵ_x^* (1σ normalized) [mm.mrad]	~ 1.6
ϵ_y^* (1σ normalized) [mm.mrad]	~ 1.25
$\Delta p/p$ (rms)	$\sim 10^{-3}$
h_{rf}	8
Full Bunch length before compression [ns]	~ 180
V_{rf} [kV]	20
E_{kin} [GeV]	1.4

TABLE 2.1: Nominal beam parameters before compression

$$\Delta Q_x = -\frac{\lambda_{max} r_p}{2\pi\beta^2\gamma^3} \oint \frac{\beta_x(s)}{\sigma_x(s)[\sigma_x(s) + \sigma_y(s)]} \mathrm{d}s \tag{2.1}$$

$$\Delta Q_y = -\frac{\lambda_{max} r_p}{2\pi\beta^2\gamma^3} \oint \frac{\beta_y(s)}{\sigma_y(s)[\sigma_x(s) + \sigma_y(s)]} \mathrm{d}s \tag{2.2}$$

Where $\sigma_x(s) = \sqrt{\beta_x(s)\epsilon_x + D_x^2(s)(\Delta p/p)^2}$ is one standard deviation of the horizontal beam size and $\sigma_y(s) = \sqrt{\beta_y(s)\epsilon_y(s)}$ one standard deviation of the vertical beam size. λ_{max} is the maximum line density in units of number of protons/m, r_p the classical proton radius, β and γ are the relativistic factors, $\beta_{x,y}(s)$ the horizontal/vertical beta functions at longitudinal position s, $\epsilon_{x,y}$ the horizontal/vertical physical emittances, D$_x(s)$ the horizontal dispersion function and $\Delta p/p$ is the rms momentum spread.

Eq. 2.1-2.2 assume a Gaussian beam in the transverse and longitudinal planes. Although the beams are not perfectly Gaussian, simulations of the direct space charge tune spread agreed with the estimates given by the these equations.

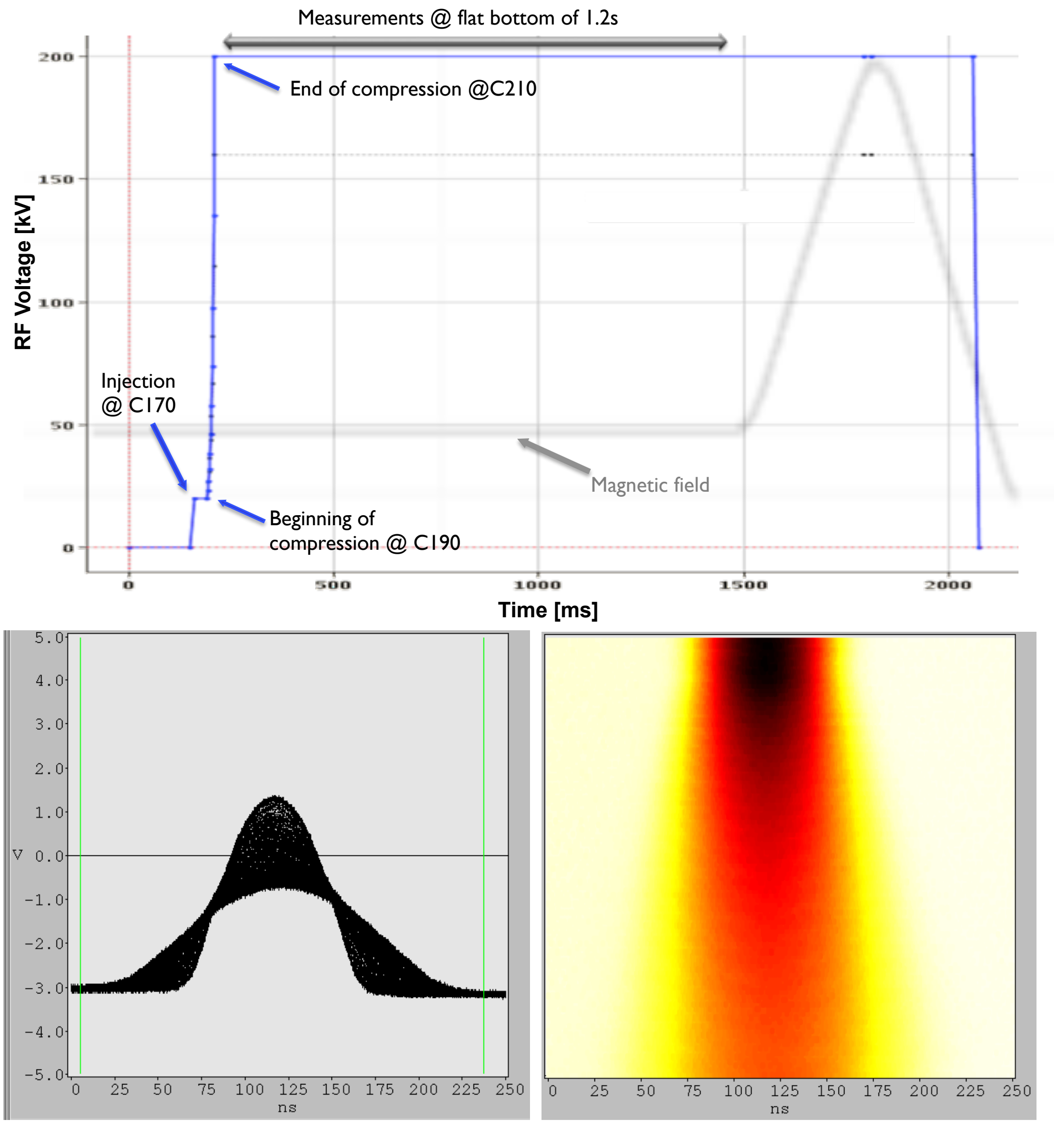

Figure 2.4: Total cavity voltage throughout the cycle(top) and Measured longitudinal beam profiles during an adiabatic bunch compression (bottom). The bottom left figure shows the several longitudinal profiles of the bunch during the compression. The bottom right figure is a waterfall representation of the bottom left figure where time in a bottom-up direction.

2.3.3 Choice of working point

As mentioned, the allowed budgets for beam-loss and emittance blow-up are 5% each, therefore the measurement working point was chosen to have less than 5% loss. During the scan of the working points, beam-loss was observed when any of the transverse tunes was close to 6.25. In Fig. 2.5, the plots represent the beam-loss in 10^{10} protons with respect to the horizontal tune (left) and vertical tune (right), the other tune is always fixed to 6.23. The error bars are the random errors due to the reproducibility from cycle to cycle, as the measurement was averaged over 10 cycles. Only the random errors are important for these graphs because other systematic errors cancel-out in a relative measurement. This observation was surprising as in previous studies, the 4^{th} order resonance has not been observed to be excited and causing beam losses, as can be seen in Fig. 2.2. This scan lead to the choice of the working point Q_x= 6.23 and Q_y= 6.255 as it had less than 5% losses, even with the highest bunch-compression. The strategy was then to move the vertical working point downwards to Q_y= 6.245, closer to the integer to see its effect on the beam.

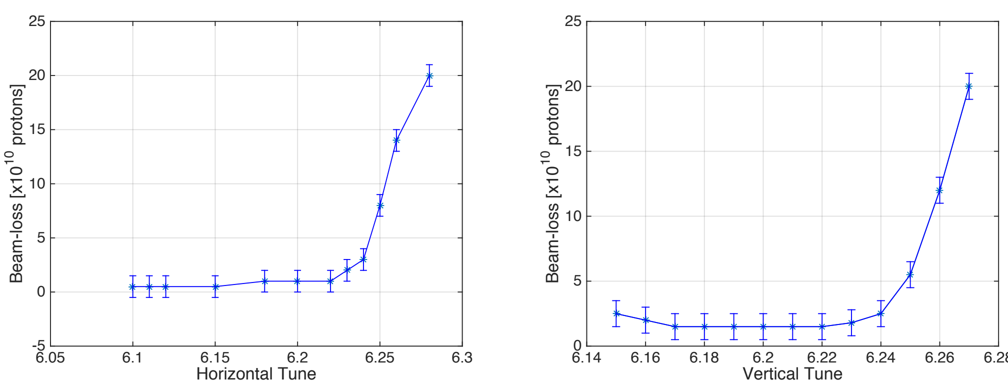

FIGURE 2.5: Loss scan with respect to working point. Horizontal tune scan (vertical tune constant at 6.23) on the left. Vertical tune scan (horizontal tune constant at 6.23)

2.4 Measurement results

The results of this campaign are summarised in Fig. 2.6 where the vertical axis is the vertical emittance growth, the horizontal axis is the maximum vertical tune-shift due to space charge and the color-scale is the beam loss during the 1.2 s plateau at 1.4 GeV. The two lines are there simply to connect the measurements of a given working point and guide the eye, the blue one is at the working point (6.23 ; 6.255) while the pink one is at (6.23 ; 6.245).

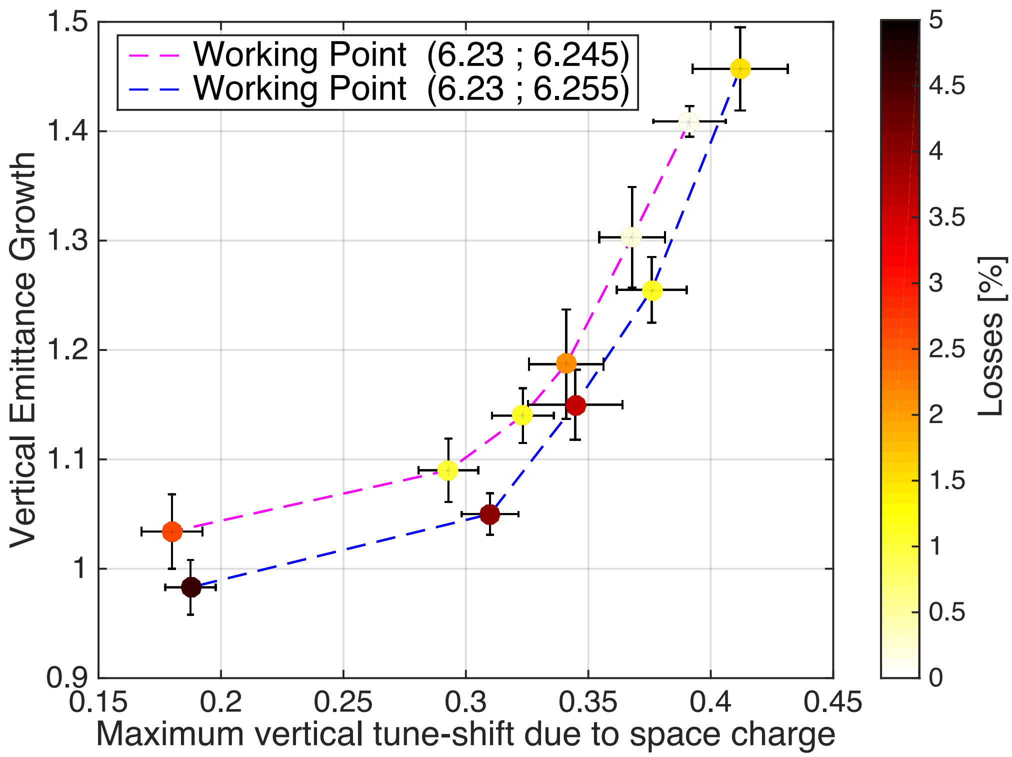

FIGURE 2.6: Vertical emittance growth and beam-loss with respect to the maximum vertical detuning due to space charge after 1.2 s.

The behavior in Fig. 2.6 is very interesting because it reveals several important effects:

- The emittance growth has an exponential-like behavior with respect to tune-spread.

- The effect of the integer resonance:

  As the space charge creates an incoherent tune-spread, where the smaller amplitude particles receive larger detuning, the integer resonance overlaps the incoherent-tune of the small amplitude particles, therefore it is the source of emittance growth. It is illustrated by the decrease of the emittance blow-up when the vertical working point is increased from 6.245 (pink line) to 6.255 (blue line).

- The effect of the 4^{th} order resonance:

  On the other side of the tune-spread, the 4^{th} order overlaps the incoherent-tune of the large amplitude particles, causing mainly beam losses. It is illustrated by the higher beam-loss when the vertical tune is at a higher value (i.e. 6.255), due to a larger number of particles overlapping the resonance. It can also be noticed that the beam-loss decreases when there is a larger spread as the particles density close to the 4^{th} order resonance is decreased and therefore the beam-loss.

  Losses are measured with a working point below the resonance (at 6.245) because of the chromatic detuning ($Q'_y \,.\, \Delta p/p(4\sigma) \approx 2.8\,10^{-2}$) that brings particles on the resonance.

In a very approximate picture the results can be explained by the fact that the incoherent tune-spread of the beam is trapped between two resonances: the integer resonance overlapping the tune of the small amplitude particles, causing the emittance growth; and the 4^{th} order resonance overlapping the tune of the large amplitude particles,

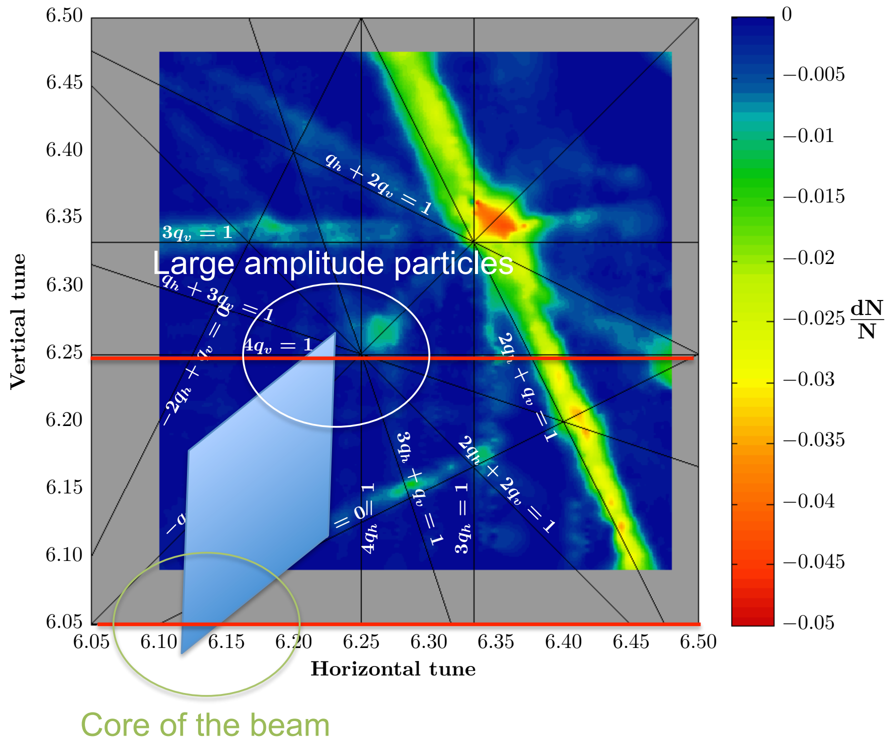

FIGURE 2.7: Illustration of the overlapping between the beam's tune-spread and the integer and the fourth order resonances.

causing beam-loss (see Fig. 2.7). For a large tune-spread, the choice of the working point is therefore a trade-off between emittance growth due to the integer and beam-loss due to the fourth order resonance.

In this study only the vertical emittance growth is taken into account because the horizontal emittance did not show a significant variations since the maximum tune spread in the horizontal plane did not exceed -0.22 with a horizontal tune of $Q_x = 6.23$ (see Fig. 2.8).

On the other hand, when looking at the time evolution of the emittance growth in Fig. 2.9, two regimes can be recognized:

- The first regime is a fast growth between the two first measurement points (200 ms).

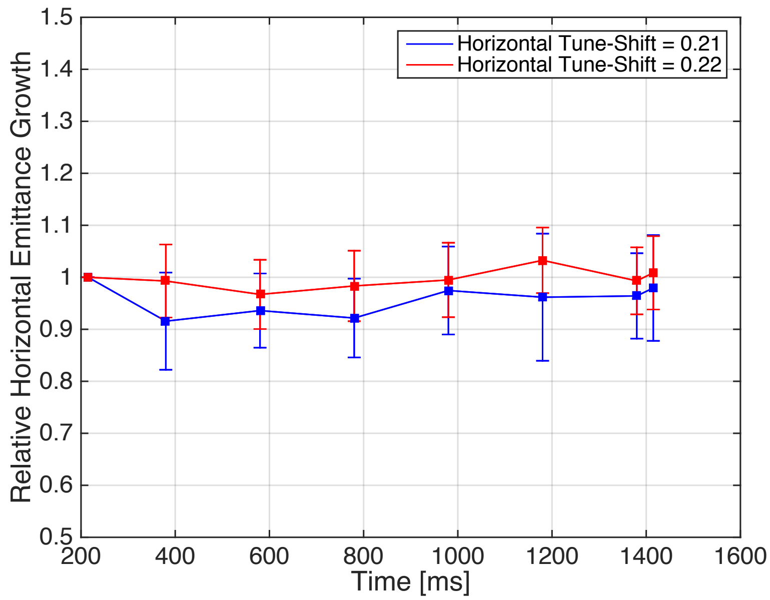

FIGURE 2.8: Horizontal emittance growth with respect to the maximum vertical detuning due to space charge and storage time, at the working point (6.23 ; 6.255).

- The second regime is a slower asymptotic growth.

This result is interesting for the choice of the possible filling schemes of the LHC. One of the possibilities is a single batch injection scheme, where instead of injecting 4+2 bunches in 2 batches, only 1 batch of 4 bunches is injected and immediately accelerated, therefore avoiding the long waiting time at injection but producing 48 bunches. Such a scheme would result in 5-10% decrease of the total number of bunches in the LHC depending on the filling scheme, but if the final emittance of such a scheme is much smaller, the brightness of the beam could be higher. Fig. 2.9 suggests that such a scheme wouldn't be efficient for tune-spreads beyond 0.34 since the fast regime would already damage the beam quality and brightness.

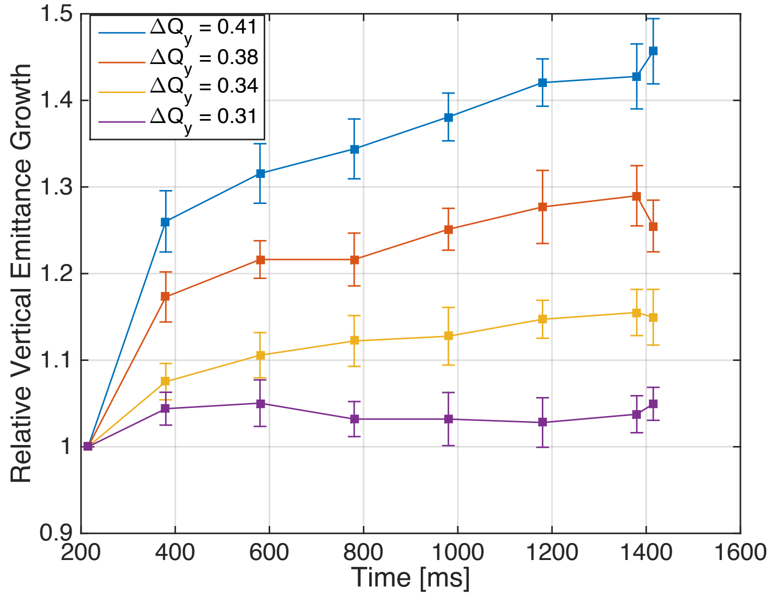

FIGURE 2.9: Vertical emittance growth with respect to the maximum vertical detuning due to space charge and storage time, at the working point (6.23 ; 6.255).

2.5 Simulations

A simulation study was done in order to confirm that the incoherent tune-spread trapped between two resonances would result in the behavior observed in Fig. 2.6 and Fig. 2.9. Due to the very long computing-time needed to reproduce 1.2 s with PTC-ORBIT ($\approx$ 500 days per simulation), it was thought to artificially excite the 4^{th} order resonance in order to enhance the beam-loss and consequently have a visible emittance growth and beam-loss in a shorter computing time. On the other hand, the lattice of the PS was simplified to increase the simulation speed. Therefore the aim of this study is not to reproduce the absolute value of the emittance growth and losses but rather to verify that their behavior with respect to working point and maximum tune-shift due to space charge, agrees with the measurement.

The lattice used was simplified by removing all multipoles, originally used to match the non-linear chromaticities. Then an octupole in straight-section 39 (oct39) was excited to enhance the effect of the 4^{th} order resonance. The simulations were carried out using the frozen space charge module of pyORBIT. A parameter scan was performed to choose a set of beam parameters as well as an octupole excitation that allow a visible effect in terms of emittance growth and beam-loss within 1000 turns. The parameters used are given in Tab. 2.2.

Parameters	Value
Intensity [10^{10} ppb]	80-160
ϵ_x (1σ normalized) [mm.mrad]	3
ϵ_y (1σ normalized) [mm.mrad]	3
h_{rf}	8
Bunch length [ns]	160
V_{rf} [kV]	20
E_{kin} [GeV]	1.4
I (oct39) [A]	10

Table 2.2: Simulation parameters

Two working points were chosen (6.23 ; 6.26) and (6.23 ; 6.27), the vertical tunes are increased with respect to the measured ones to enhance the effect of the 4^{th} order resonance and obtain significant beam-loss over 1000 turns. The incoherent tune-spread was varied by changing the bunch intensity between 80 and 160 10^{10} ppb. Following the same post-processing as in the measurement case, the simulations gave the results presented in Fig. 2.10. The results show a similar behavior of the emittance growth and beam-loss with respect to the maximum tune-shift due to space charge as well as the working point. Increasing the zero current vertical tune decreases the effect of the integer resonance and therefore decreases the emittance blow-up. On the other hand, it increases the population of protons crossing the 4^{th} order resonance and therefore increases the losses. The two plots have the same pattern of increase of losses from working point to the other as well as from tune-spread to the other. The emittance blow-up has a similar behavior growth with respect to the tune-spread and to the change of working point.

The time evolution of the emittance growth in Fig. 2.11, shows a similar behavior as in the measurements Fig. 2.9. There are 2 regimes, first a fast growth, then follows a slow asymptotic regime. It also indicates that the first regime is very fast, confirming that a single batch injection would not be efficient for large tune-spreads.

The high frequency noise of the curves in Fig. 2.11 is due to the limited number of macro-particles used in the simulations, leading to a small fluctuation of the estimated emittance throughout the betatronic motion of the macro-particles.

2.6 Discussion

Simulations confirm that the measured behaviors are compatible with a tune-spread enclosed between two resonances.

From Fig. 2.6, it could be deduced that the current maximum acceptable tune-spread is -0.34, in order to respect the 5% limitation in terms of emittance blow-up and beam-loss.

It is interesting to notice that the $Q_y = 6.25$ resonance was discovered to be excited as shown in Fig. 2.5, while it was not observed during the loss-map measurements as in Fig. 2.2. Therefore a study of the $Q_y = 6.25$ resonance is very important to understand its source and possible mitigations in order to increase the maximum acceptable incoherent tune-spread.

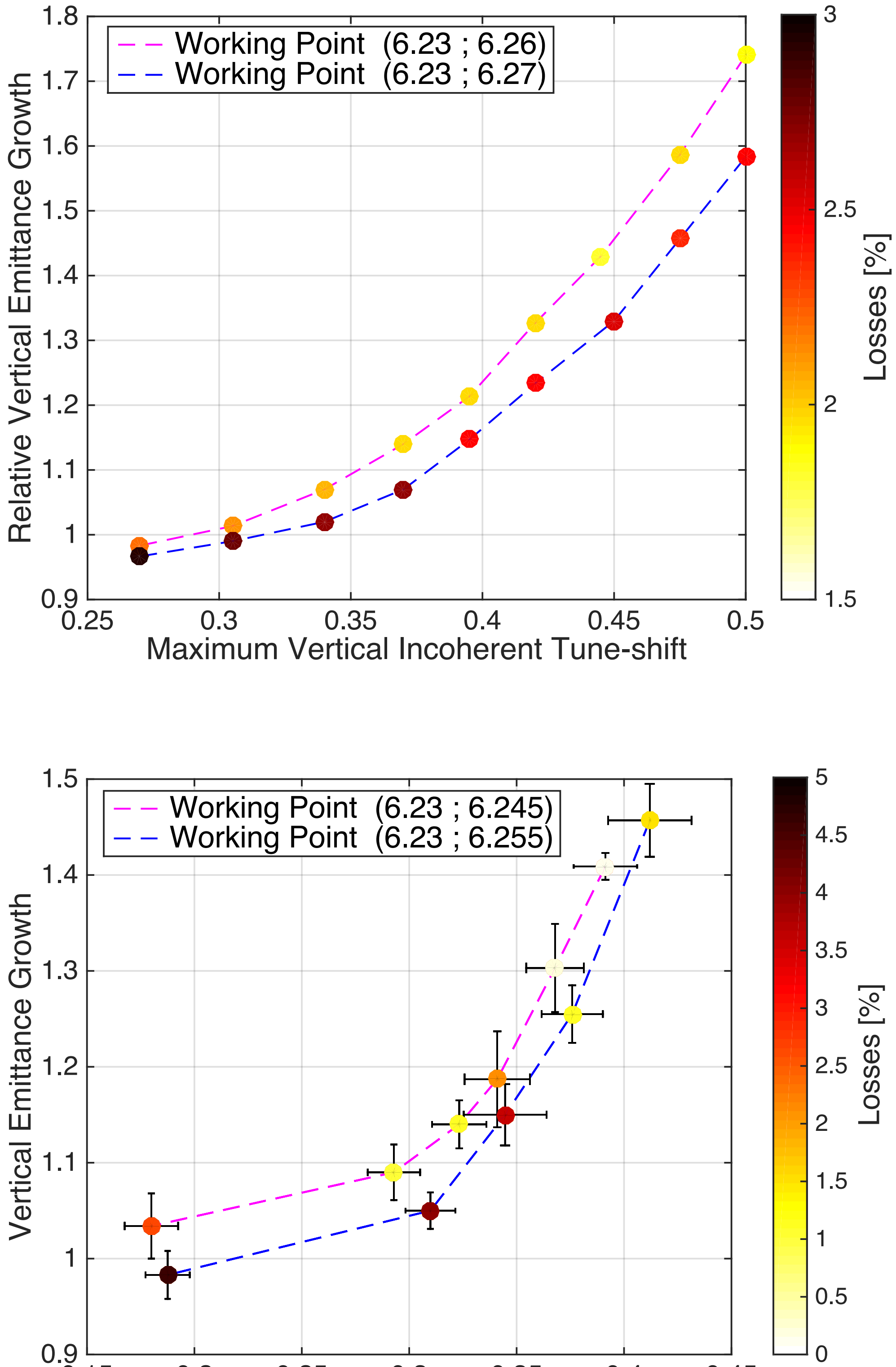

FIGURE 2.10: Vertical emittance growth and beam-loss with respect to the maximum vertical detuning due to space charge, as given by simulations (upper) and measurements (lower, same as Fig. 2.6)

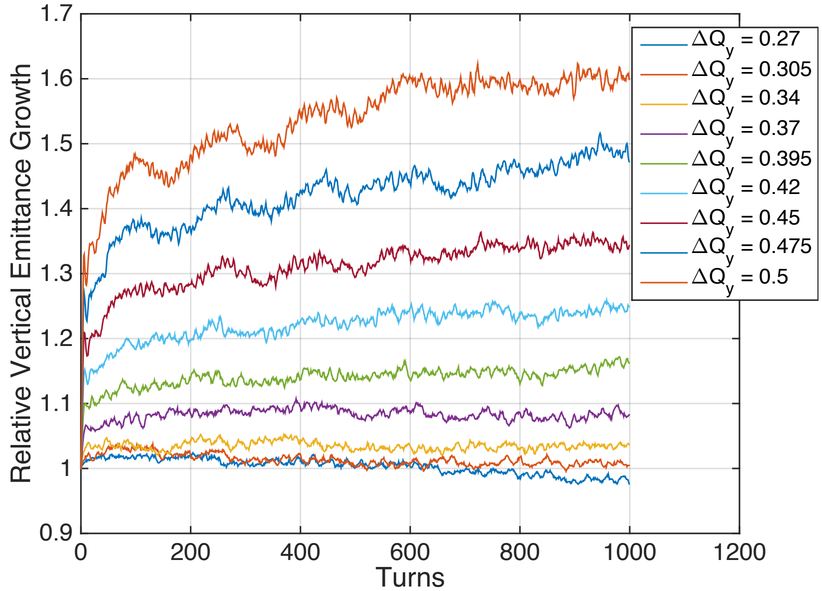

FIGURE 2.11: Simulated vertical emittance growth with respect to the maximum vertical detuning due to space charge and storage time, at the working point (6.23 ; 6.26).

Chapter 3

8^{th} order super-structure resonance driven by space charge

During the study of the maximum acceptable tune-spread in the PS, the $Q_y = 6.25$ resonance was observed to be excited even though it was never seen in the loss-map measurements [4]. The only difference between these two measurements being the beam parameters, therefore the resonance was thought to be driven by the beam itself. A detailed study started in order to identify the reason of its excitation as well as the possible methods to mitigate it.

3.1 Possibility of a space charge induced resonance in the PS

3.1.1 Space charge as a driving term

In low energy synchrotrons, usually space charge effects set the limit of the maximum brightness within a certain budget of emittance growth and beam loss. This limit is usually expressed in terms of the maximum acceptable incoherent detuning due to space charge. While the tune spread provides the area occupied by the individual tunes of the different particles, the choice of working point is usually made in order to avoid overlapping the space charge tune-spread and the harmful betatronic resonances.

Although it is possible to correct magnet errors and misalignments using corrector magnets, they are not the only source of resonance excitation. The beam of charged particles generates a field and feels it in addition to external magnetic fields. The self-field has several particularities compared to an external magnetic field generated by a magnet. For example, the self-field is centered at the center of the bunch, while the magnet is centered around the geometric center. Another very important particularity is that the self-field has the harmonics of the beam envelop, which are the same as the β-function harmonics (RMS beam size is: $\sigma = \sqrt{\epsilon_{z,RMS}\beta_z}$). In previous studies, it has been shown that space charge can drive betatronic resonances [11] [28].

In an accelerator with N FODO cells, the beam envelop is modulated N time, which makes the harmonic N of the space charge force. If we assume a transversely Gaussian beam, the space charge potential would contain only even orders because of the symmetry. Consequently, the space charge force can only excite even order resonances $(2^{nd}, 4^{th}, 8^{th}...etc)$. If space charge has the same harmonic N as the betatronic resonance, the resonance is called a structure resonance and it is excited even when the lattice has no magnetic error or misalignment. Space charge can also drive resonances of different harmonics (non-structure resonances), but the resonance strength and effect in this case are significantly weaker and there is a need of beam envelop perturbation in order to a space charge driven non-structure resonance to be excited.

Assuming the charge distribution is Gaussian in transverse planes $\rho(x,y) = \frac{\lambda e}{2\pi\sigma_x\sigma_y} exp(-\frac{x^2}{2\sigma_x^2} - \frac{y^2}{2\sigma_y^2})$, the space charge potential V_{sc} can be expanded as [11], [12]:

$$V_{sc}(x,y) = \frac{r_p \lambda}{\beta^2\gamma^2 B_f} \int_0^\infty \frac{-1 + exp(-\frac{x^2}{2\sigma_x^2+t} - \frac{y^2}{2\sigma_y^2+t})}{\sqrt{(2\sigma_x^2+t)(2\sigma_y^2+t)}} dt \tag{3.1}$$

$$
\begin{aligned}
V_{sc} \approx -\frac{r_p\lambda}{\beta^2\gamma^2 B_f}\Bigg[& \frac{x^2}{\sigma_x\left(\sigma_x+\sigma_y\right)}+\frac{y^2}{\sigma_y\left(\sigma_x+\sigma_y\right)} \\
& + \frac{2\sigma_x+\sigma_y}{12\sigma_x^3\left(\sigma_x+\sigma_y\right)^2}x^4+\frac{1}{2\sigma_x\sigma_y\left(\sigma_x+\sigma_y\right)^2}x^2y^2+\frac{\sigma_x+2\sigma_y}{12\sigma_y^3\left(\sigma_x+\sigma_y\right)^2}y^4 \\
& + \frac{\left(8\sigma_x^2+9\sigma_x\sigma_y+3\sigma_y^2\right)}{60\sigma_x^5\left(\sigma_x+\sigma_y\right)^3}x^6+\frac{\left(3\sigma_x+\sigma_y\right)}{4\sigma_x^3\sigma_y\left(\sigma_x+\sigma_y\right)^3}x^4y^2 \\
& + \frac{\left(\sigma_x+3\sigma_y\right)}{4\sigma_x\sigma_y^3\left(\sigma_x+\sigma_y\right)^3}x^2y^4+\frac{\left(3\sigma_x^2+9\sigma_x\sigma_y+8\sigma_y^2\right)}{60\sigma_y^5\left(\sigma_x+\sigma_y\right)^3}y^6 \\
& + \frac{\left(16\sigma_x^3+29\sigma_x^2\sigma_y+20\sigma_x\sigma_y^2+5\sigma_y^3\right)}{280\sigma_x^7\left(\sigma_x+\sigma_y\right)^4}x^8 \\
& + \frac{\left(5\sigma_x^3+20\sigma_x^2\sigma_y+29\sigma_x\sigma_y^2+16\sigma_y^3\right)}{280\sigma_y^7\left(\sigma_x+\sigma_y\right)^4}y^8 \\
& + \frac{\left(5\sigma_x^2+4\sigma_x\sigma_y+\sigma_y^2\right)}{10\sigma_x^5\sigma_y(\sigma_x+\sigma_y)^4}x^6y^2+\frac{\left(\sigma_x^2+4\sigma_x\sigma_y+\sigma_y^2\right)}{4\sigma_x^3\sigma_y^3\left(\sigma_x+\sigma_y\right)^4}x^4y^4 \\
& + \frac{\left(\sigma_x^2+4\sigma_x\sigma_y+5\sigma_y^2\right)}{10\sigma_x\sigma_y^5\left(\sigma_x+\sigma_y\right)^4}x^2y^6 \\
& + 10^{th} order\, terms,\ 12^{th} order\, terms\, ...)\Bigg]
\end{aligned}
\tag{3.2}
$$

where σ_x and σ_y are the RMS beam size in horizontal and vertical directions, r_p is the classical proton radius, λ is the line charge density (the ratio of the total charge to the bunch length), β and γ are the relativistic factors, B_f is the bunching factor defined by the ratio of the average density to the peak density.

Because of the symmetry of the charge distribution, only even order potential exists. Both the beam envelope and the resonance strength contain the lattice β function, therefore the harmonic analysis of the beta function gives the estimate of the strength of space charge driven resonance.

3.1.2 PS parameters

In this section we are going to test if the $Q_y = 6.25$ resonance could be driven by direct space charge in the CERN PS. If a resonance is excited by space charge and not by the magnetic field errors, the betatronic frequency has to have the same harmonic as the space charge force, which has the same harmonic as the beam envelope. With it's 100 combined function magnets, the PS has 50 unit-cells "FDODF", and therefore it has a very strong harmonic 50. Even though the 50 unit-cells symmetry is slightly perturbed by the use of low field tuning quadrupoles used at injection energies and by the difference in length between the drifts, the largest harmonic extracted from the vertical β function is 50 as shown in Fig. 3.1. It is important to notice that the harmonic 25 is not excited, not even by introducing up to 1% random errors of the quadrupolar fields, which is much larger than the design tolerance and verified by the latest magnetic field measurements [17]. Therefore the excited resonance should have a harmonic 50, which means the resonance is $8Q_y = 50$. Consequently, $8q_y = 1$ in each cell (q being the phase advance per cell), or in other terms, the particles are resonant at every cell, making this resonance a "super-structure resonance" [11].

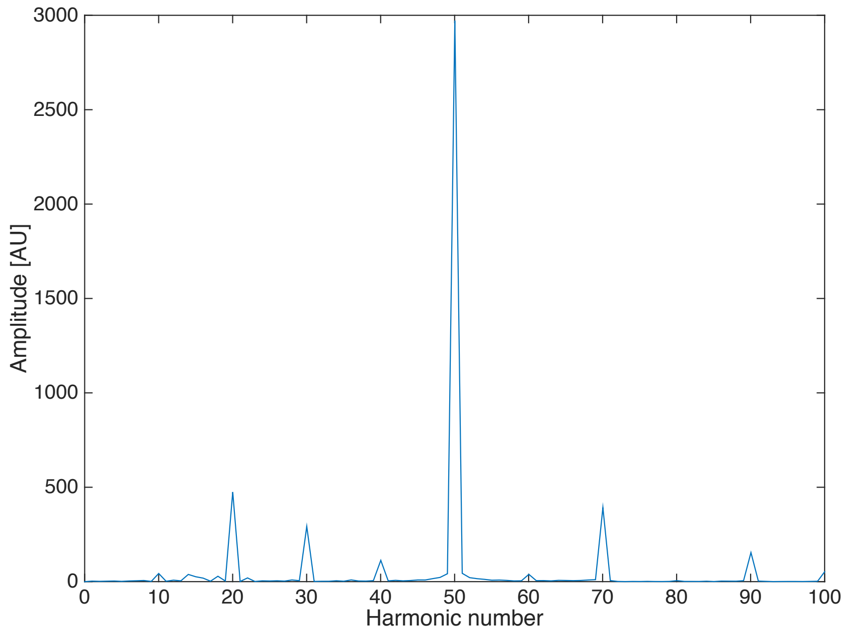

FIGURE 3.1: Harmonics of the vertical β function

From the above, we can conclude that if the $8Q_y = 50$ resonance is driven by space charge, it would be a 8^{th} order super-structure resonance.

3.1.3 Phase space structure

3.1.3.1 Harmonic 50

A simulation was made with IMPACT [15] using a simplified lattice, where only direct space charge is the source of non-linearities, in order to verify whether it drives the 8^{th} order resonance. The beam parameters used are given in Tab.3.1.

In order to reconstruct a phase space structure due to a resonance generated by the self fields, one has to look at a fixed longitudinal

Parameters	Value
Intensity [10^{10} ppb]	30
ϵ_x (1σ normalized) [mm.mrad]	1.6
ϵ_y (1σ normalized) [mm.mrad]	1.5
Bunch length [ns]	92
$\Delta p/p$ (rms)	0.51 10^{-3}
E_{kin} [GeV]	1.4

TABLE 3.1: Simulation parameters

position because the island position depends on the field strength which in turn depends on the local charge density and therefore on s.

Figure 3.2 shows the vertical phase space simulated using IMPACT with a 3 D self-consistent space charge model [15], for particles that start at $s = 0$ in the longitudinal direction and the same value of horizontal position and angle. The phase space shows a clear 8^{th} order resonance structure with 8 islands. Since direct space charge is the only source of non-linearities in these simulations, this proves that the 8^{th} order resonance $8Q_y = 50$ is driven by space charge.

3.1.3.2 Test of harmonic 25

$Q_y = 6.25$ resonance could a 4^{th} order (harmonics 25) or an 8^{th} order (harmonic 50). The symmetry of the PS, the harmonic analysis of the lattice and the phase space structure confirm that it is the 8^{th} order resonance.

An additional interesting test to verify our understanding of the mechanism is to artificially change the symmetry of the PS lattice from 50 x"FDDF" cells to 25 x"FDDFFDDF" cells by breaking the symmetry of the cell, making the unit of symmetry twice as long as the

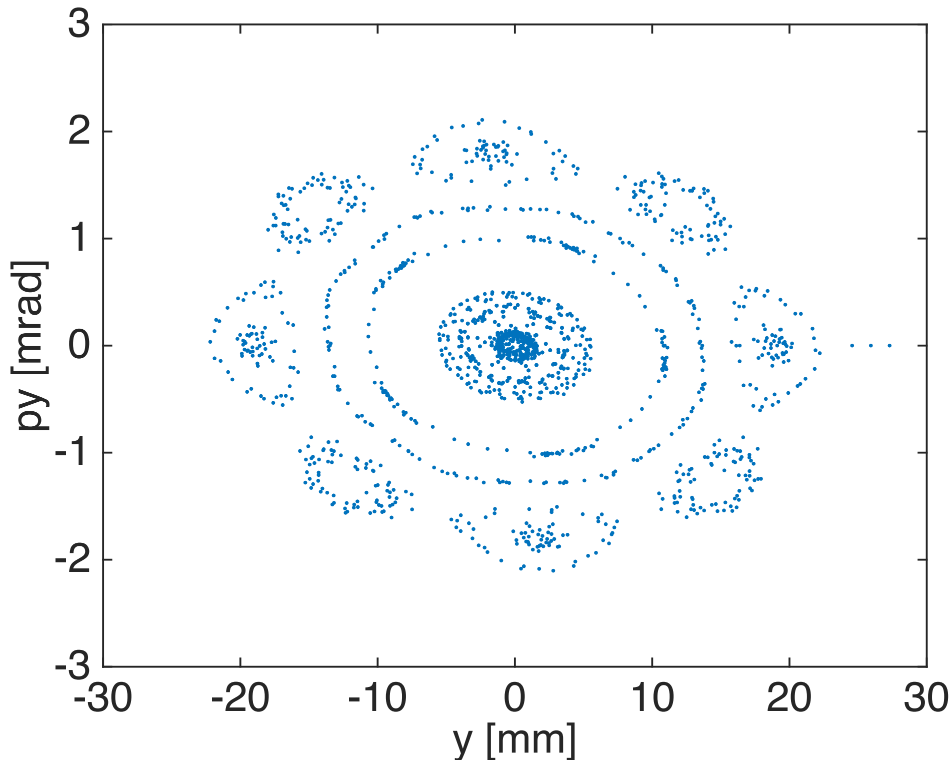

FIGURE 3.2: Vertical phase space for particles at the center of the bunch horizontally and longitudinally, obtained with IMPACT including space charge effects.

present one. Such a change lead a significant increase of the harmonic 25 in the PS lattice, as shown in Fig. 3.3.

Following the same analysis, we could predict now that the harmonic 25 will be excited and driving the 4^{th} order resonance $4Q_y = 25$. A phase space analysis, similar to the one done in section 3.1.3.1, was done using IMPACT.

This test confirms our understanding of the problem, the 8^{th} order resonance is excited due to the symmetry of the lattice. The 4^{th} order cannot be driven by space charge unless there is exactly the same error in every cell, making the symmetry unit twice as large, which

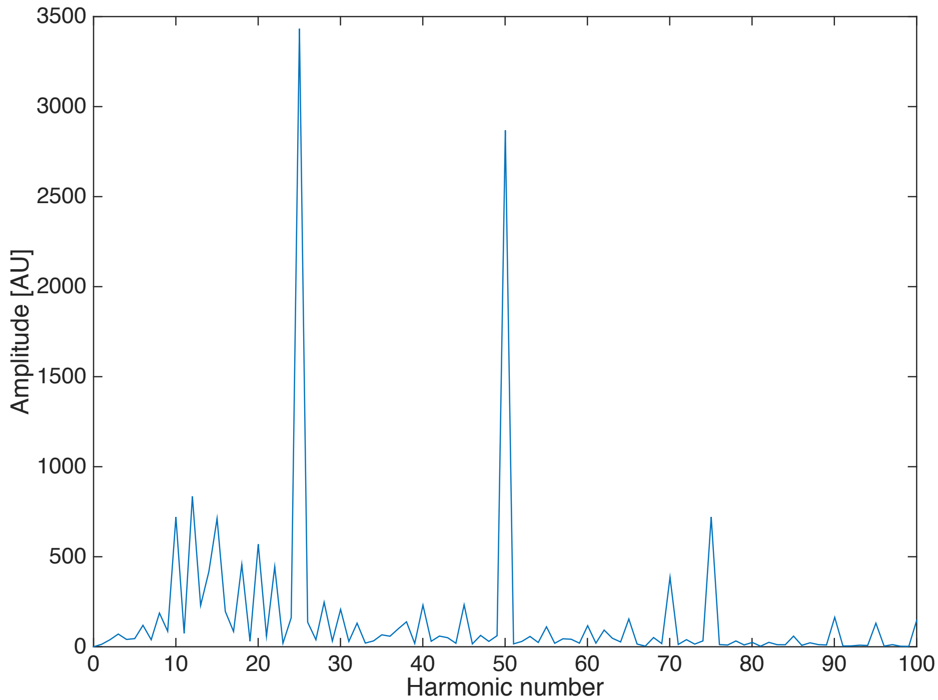

FIGURE 3.3: Harmonics of the vertical β function.

is highly unlikely. Therefore, the observed resonance must be an 8^{th} order resonance.

3.1.4 Conclusion

Given the PS lattice symmetry, the harmonic analysis shows that a space charge driven resonance has to have a harmonic 50. The space charge simulations show that when direct space charge is the only source of non-linearities then it drives the 8^{th} order super-structure resonance $8Q_y = 50$ in the case of the typical operational beam parameters. This translates for machine operation in the fact that if the space charge non-linear field dominates as the machine non-linearities, then it could excite the $8Q_y = 50$ resonance. This will be the case at

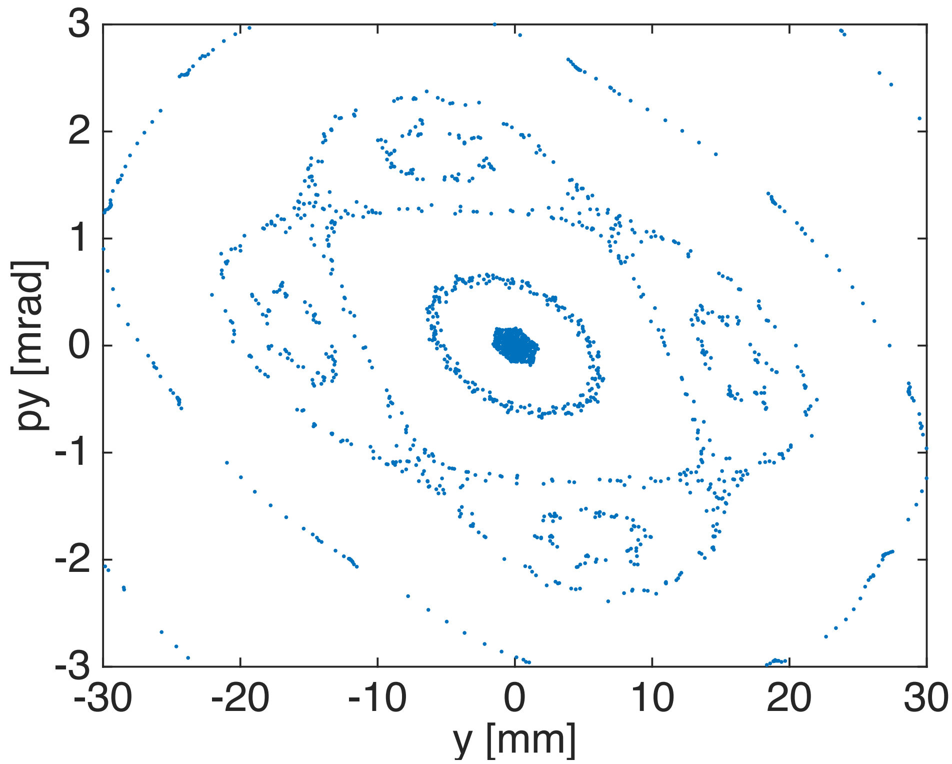

FIGURE 3.4: Vertical phase space for particles at the center of the bunch horizontally and longitudinally, obtained with IMPACT including indirect space charge effects, for a modified lattice such that the harmonic 25 is enhanced.

injection energies, where the machine is very linear [4] and direct space charge tune-shift exceed |0.3| for the LHC-type beams. We have now to verify if this resonance could explain the amount of beam loss observed at the crossing of this resonance.

3.2 Measurements and Simulations

3.2.1 Brightness dependence measurement

The main difference between the loss-map measurements and the integer resonance study presented in Chap. 2 are the beam parameters.

For the loss map, the used beam was transversely very large, to enhance the loss rate and to have a small direct space charge tune-spread (≈ -0.05) to minimize the overlap of several resonances for the same single particle tune and be able to disentangle the effect of each single resonance at the time. On the other hand, during the integer resonance study, the used beams had large space charge tune-spread (-0.2 to -0.4). Consequently, the resonance was thought to be excited by the beam itself and more specifically by the beam self-field. This hypothesis could be experimentally tested by observing the difference in terms of beam-loss with respect to beam space charge forces. In order to clearly quantify the beam-loss, the resonance was crossed twice in a step shape as illustrated in Fig. 3.5. The horizontal tune is kept at 6.23 and the vertical tune is ramped from 6.24 to 6.30 during 20 ms then kept constant for 300 ms, then it is ramped down to 6.24 during 20 ms. The advantage of such a step is to have a beam-loss that starts and ends at precise timings.

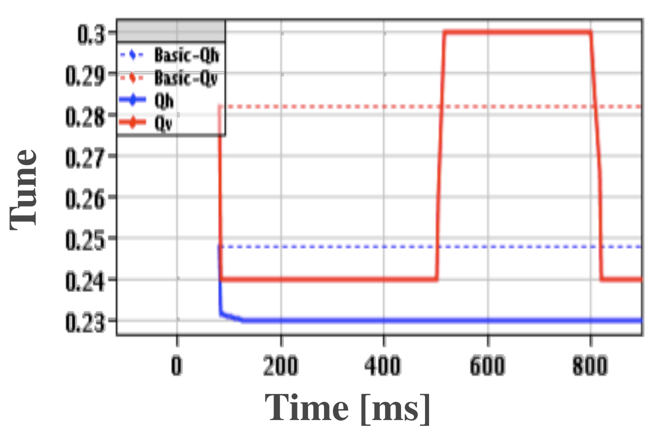

FIGURE 3.5: Tune step used to cross the resonance.

In order to test the hypothesis of a space charge excited resonance, four beams with different space charge forces were used to cross the resonance. The space charge is quantified by the maximum detuning due to space charge given by Eq. 2.1-2.2, computed for each of the beams of Tab. 3.2.

Beams	ΔQ_x	ΔQ_y
Beam 1	-0.22	-0.4
Beam 2	-0.18	-0.37
Beam 3	-0.08	-0.24
Beam 4	-0.01	-0.01

TABLE 3.2: Maximum detuning due to space charge for the four beams used to cross the $Q_y = 6.25$ resonance line

In Fig. 3.6, the relative intensity of the four beams is given as a function of the time. The dashed line is the vertical tune throughout the cycle, an offset of 0.65 was added to the tune in order to fit within the same vertical scale as the relative intensities. It can be seen that the beam-loss is directly correlated to the space charge forces, in this case quantified by the maximum tune-spread. The measurement confirms the correlation between the beam brightness and the resonance excitation. We observed that the "Beam 3" did not present any loss at the first crossing, while it showed losses in the second resonance crossing. This could be explained by the direction of the crossing, as when the vertical tune is increased the islands amplitude decreases, while when the tune is decreased, the island amplitude increases, as seen in the Introduction chapter.

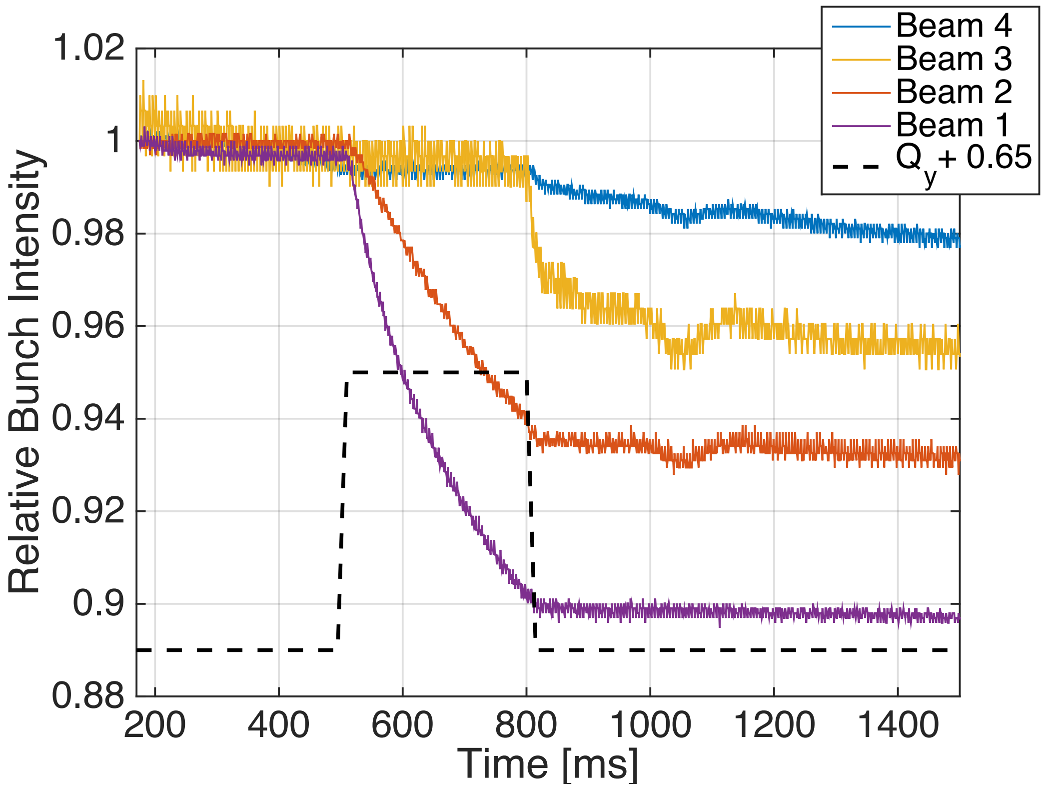

FIGURE 3.6: Relative intensity of four beams with different space charge forces while crossing the $Q_y = 6.25$ resonance (solid lines). In dashed line, the vertical tune-step with an offset of 0.65 to fit within the same vertical axis.

3.2.2 Beam loss measurement and simulation

In this section we present results of the simulation of the beam loss due to the $Q_y = 6.25$ resonance, using the frozen model in pyORBIT because of the speed limitation of the self-consistent model (500 ms would need 250 days of simulations on 48 cores). In this model, both the direct and the indirect space charge were taken into account but no magnetic errors were included. The beam parameters were the same as in Tab. 3.1.

In these simulations, the tune has been changed with a similar step as in Fig.3.5 with a plateau at Q_y=0.29 and 500 ms duration.

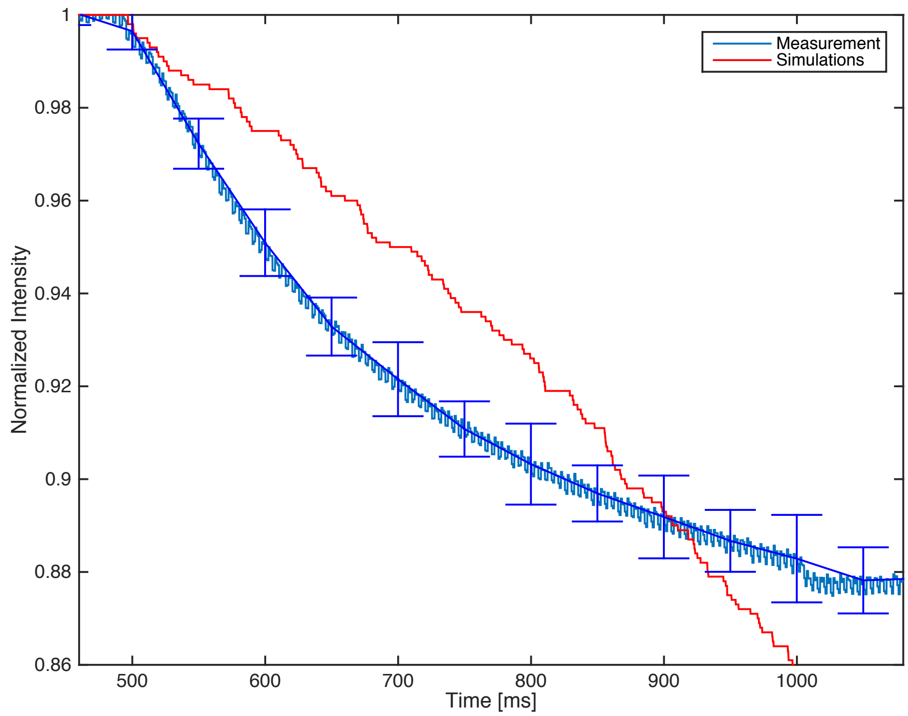

FIGURE 3.7: Relative intensity loss due to resonance crossing simulated (red) and measured (blue).

In Fig. 3.7, the blue curve is the measured normalized beam loss, while the simulated one is in red. The error bars are the standard deviation over 10 measurements for the measured curve. Fig. 3.8 is a simple zoom on the starting slope, where it can be seen that the slope of the measurement is only 1.57 larger than the simulated slope.

The main conclusion of Fig. 3.7 is that only space charge as non-linearity can explain the order of magnitude of the beam loss.

The difference between measurements and simulations could be explained by the fact that the space charge is represented by a frozen model, which could justify the absence of saturation effect in the curve, especially for a relatively small beam loss. Additionally, the

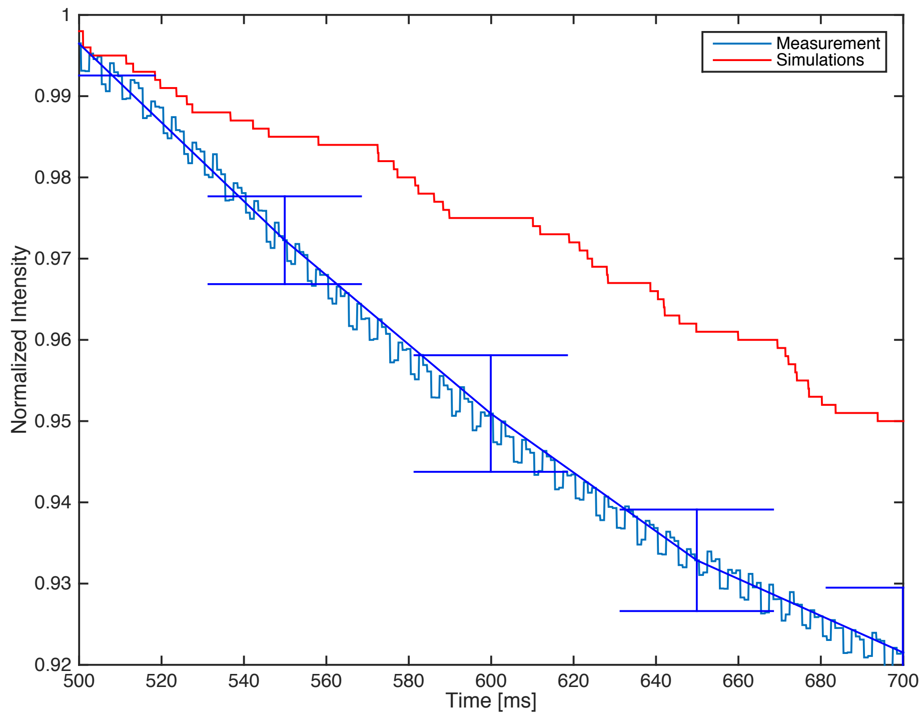

FIGURE 3.8: Relative intensity loss due to resonance crossing simulated (red) and measured (blue).

beam loss profile is very difficult to reproduce since it depends on the initial halo population, which is almost undetectable by the wire-scanner if it is in the order of few percent of the total beam intensity. The beam loss also depends on the machine alignment and magnetic errors which are not well known. For the purpose of this study, the result represents a good agreement in terms of order of magnitude of beam loss generated by the self-field and we will ignore the details of the beam loss.

Simulations confirm that space charge can drive the 8^{th} order resonance, which generates the same order of magnitude of the observed beam loss.

3.2.3 Beam loss mechanism

As discussed in the introduction, studies have shown that the overlap of the space charge necktie and an excited resonance can lead to emittance growth or beam loss due to the trapping mechanism. The trapping mechanism happens because of the particles cross the resonance as they follow the synchrotron motion. In the specific case of the $8Q_y = 50$ resonance, the resonance is driven by space charge, therefore the resonance strength also depends on the horizontal position. Fig. 3.9-3.10 shows the trajectory of a resonant particle in the 3D space (y, y', x), where the structure of the islands can be clearly seen. it is interesting to note the correlation between the horizontal position and the island amplitude. The islands are at maximum amplitudes when the horizontal position is near the center of the beam ($x = 0$). The nature of the resonance adds another modulation to the particle trapping mechanism. This mechanism was not at the center of this study but the remark was very interesting and worth more future investigations. It is important to note two points: first, Fig. 3.9-3.10 shows only 4 islands because it shows only 1 particle at the tune of 6.25. In order to see the 8 islands, one has to track two particles with initial coordinates inside of two neighboring islands. Second, the horizontal variation in Fig. 3.9-3.10 is very small because with larger variations the structure is not visible anymore. This should be due to the presence of too many modulations, as the longitudinal modulation appears at large horizontal excursions because of the dispersion.

Since the end result of all modulations is a variation of the tune, it is easier and clearer to change the tune (only 1 parameter) and see its effect, Fig. 3.11 shows the topology of the vertical phase space for 3 zero-current tunes 6.27, 6.29 and 6.31. As expected, increasing the zero-current tune decreases the island amplitudes. Therefore, any tune modulation that makes a particle cross the resonance could be a source of particle trapping, resulting in emittance growth or beam loss.

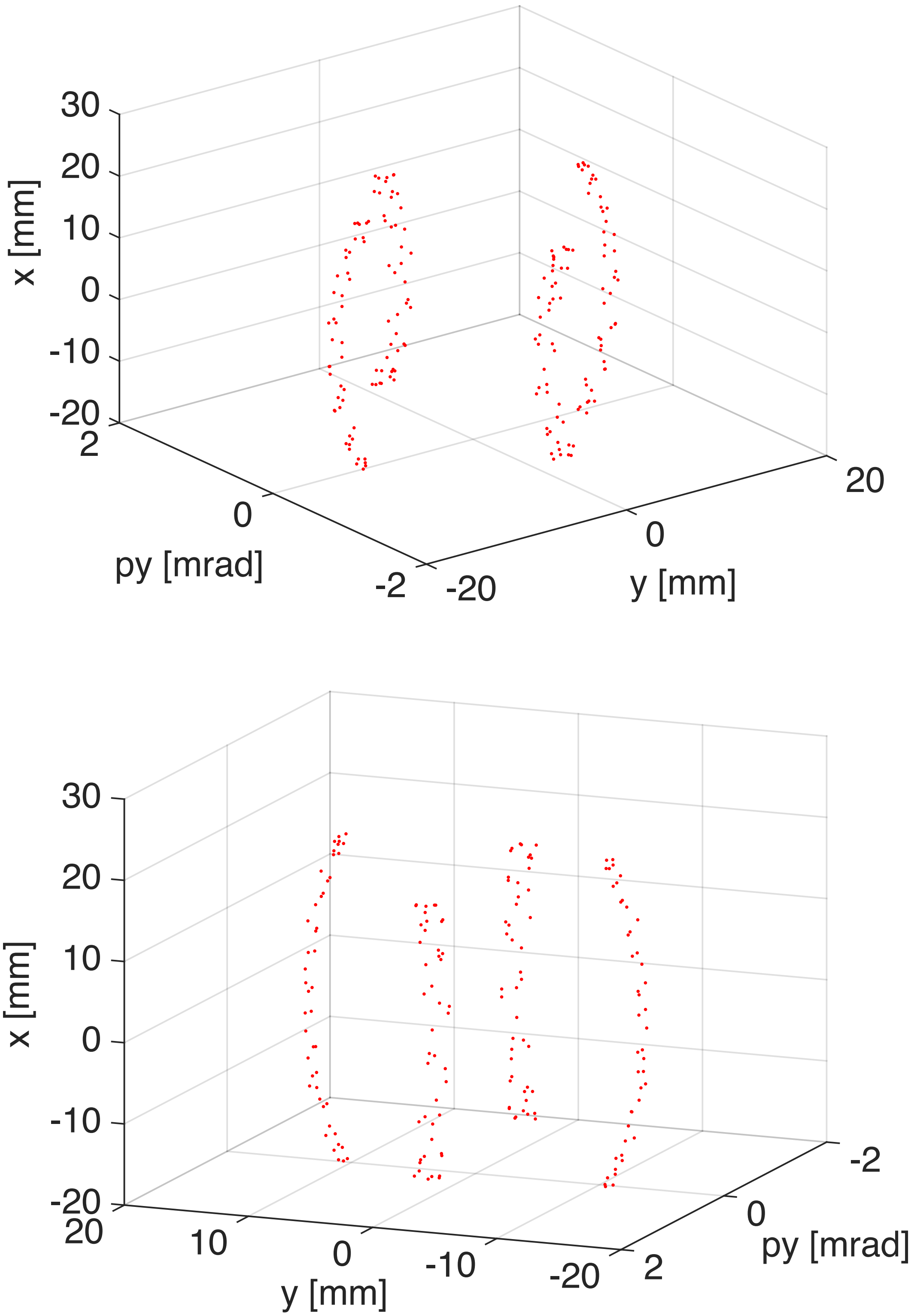

FIGURE 3.9: Trajectory of one particle in the 3D space (y, py, x). The two plots are two view angles (the bottom plot is the top plot rotated by $\frac{\pi}{2}$ around the x axis).

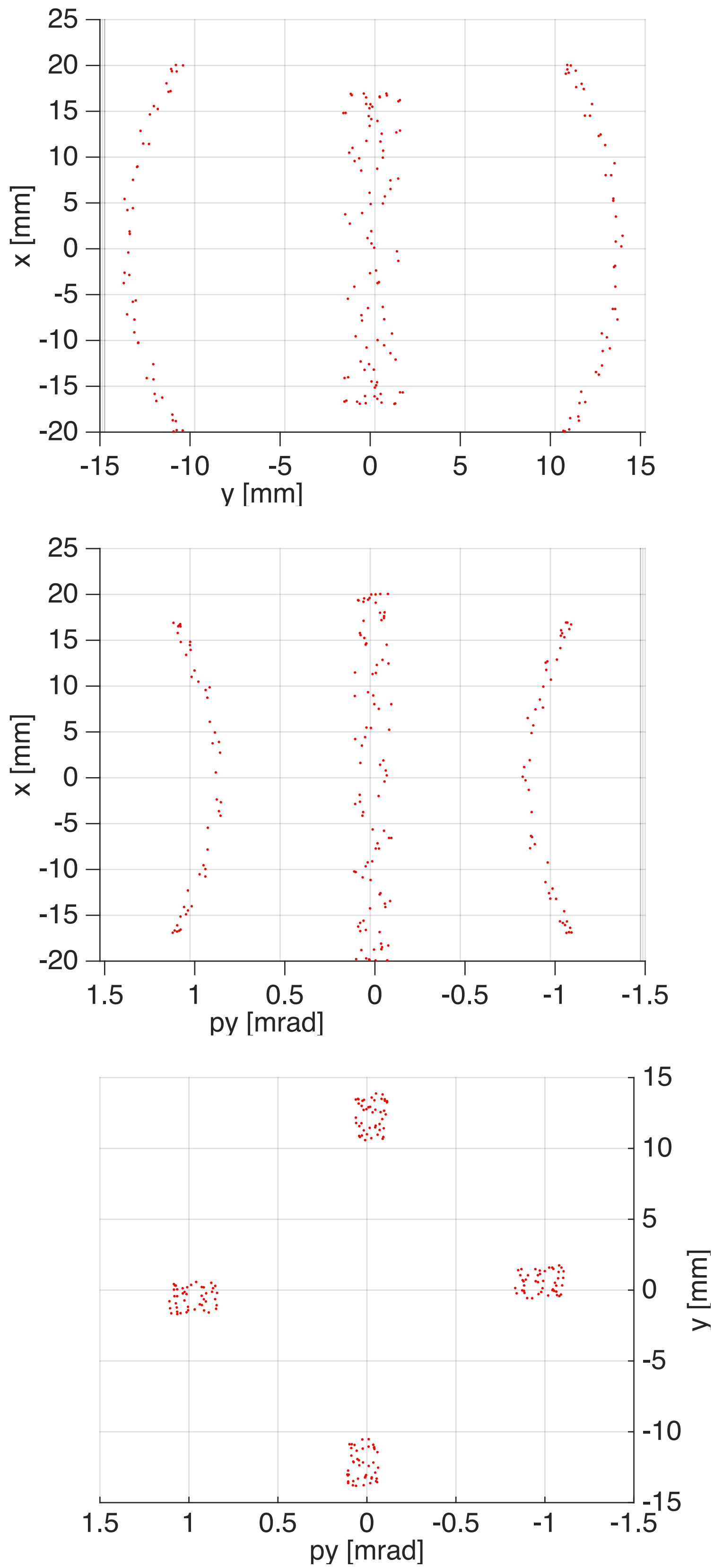

FIGURE 3.10: The 3 projections of the trajectory of a resonant particle in the 3D space (y, py, x). The projection planes are (x, y) (top), (x, py) (middle) and (y, py) (bottom).

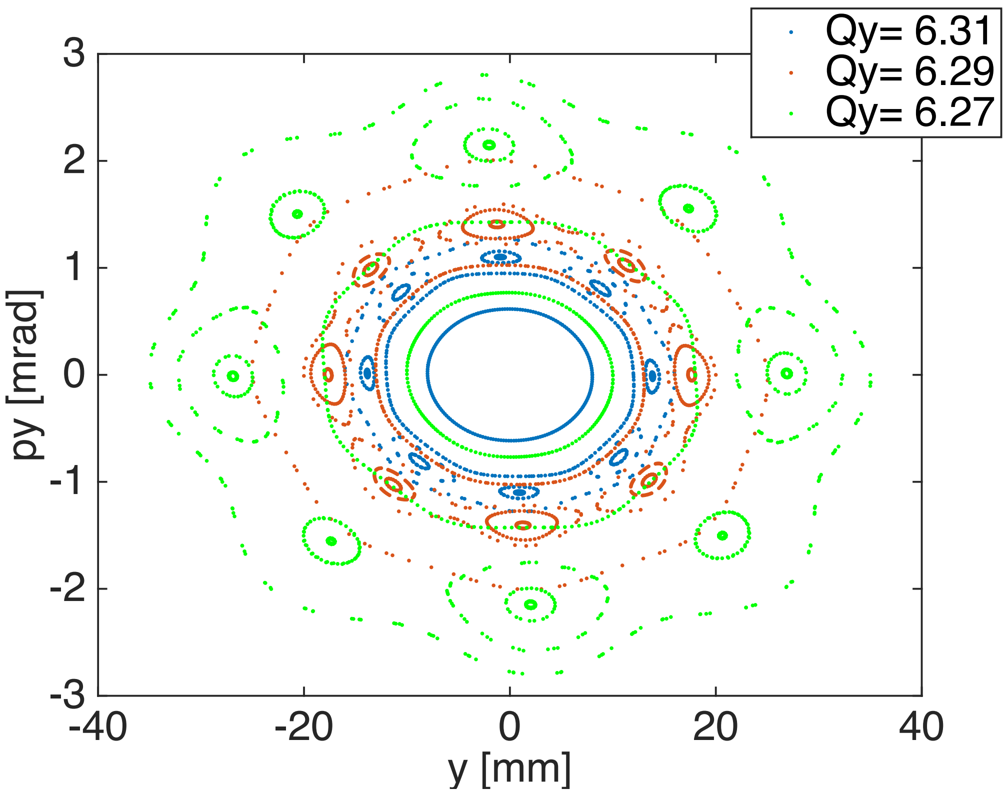

Figure 3.11: Phase space topology for 3 different vertical tunes 6.27, 6.29 and 6.31.

3.2.4 Phase space structure using different codes and space charge models

Since we expect the resonance to be space charge driven, we look at fixed s and x positions, in order to have the same space charge force and therefore the same resonance excitation, to be able to see a resonant phase space topology.

In Fig. 3.12, the vertical phase space is simulated using PTC-ORBIT with the 2.5 D self-consistent space charge model, for particles that start at $s = 0\,\mathrm{m}$ in the longitudinal direction and the same horizontal position and angle. The phase space shows a clear 8^{th} order resonance structure that extend up to 25 mm in the vertical plane at the first section of the PS ($\beta_y = 11.85\,\mathrm{m}$), which means the structure could extend up to 35 mm at the machine sections with the largest $\beta_y = 23\,\mathrm{m}$, while the vertical mechanical aperture is 35 mm, therefore explaining the beam loss occurring during the crossing of the resonance.

Several trial of phase space measurements were performed but none were successful because of the nature of the resonance, being excited by the beam itself, the space charge force depends on x and s. The phase space cannot be probed as done in other cases, for example in ref. [48].

The simulations with PTC-ORBIT and IMPACT, both revealed the 8^{th} order structure, confirming the hypothesis of the beginning of the study. It is important to note that all codes give very similar phase space topology and island amplitude (Fig. 3.12 - 3.13 - 3.14 - 3.15),

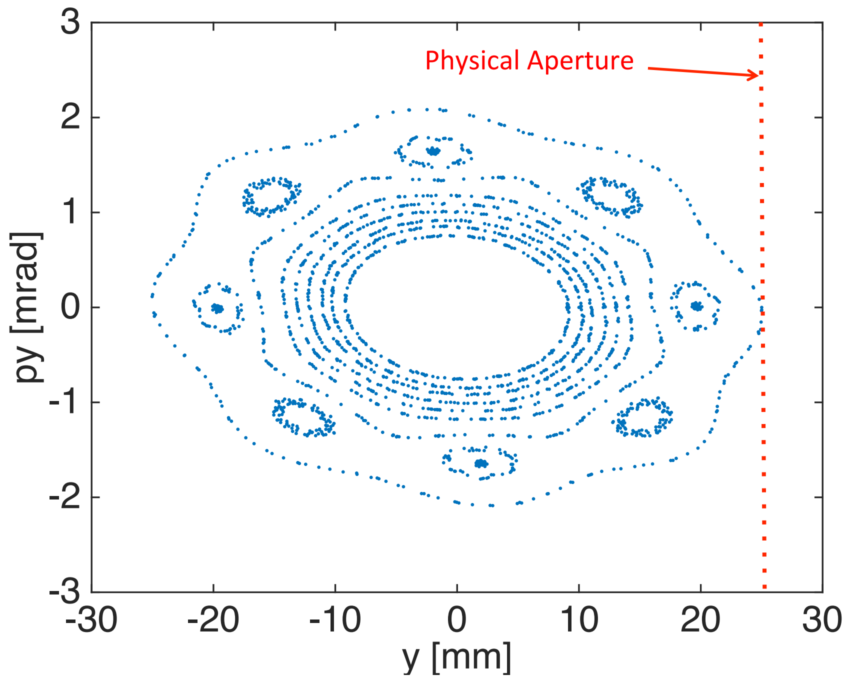

FIGURE 3.12: Vertical phase space for particles at the center of the bunch horizontally and longitudinally, obtained with PTC-ORBIT without any indirect space charge effect. The red dotted line represents the vertical physical aperture at large β.

despite of the difference in tracking and space charge models. In these simulations the only non-linear components come from the self-fields, therefore we can conclude that the 8^{th} order resonance is driven by space charge, exactly as it was assumed.

Additionally, the simulations show the same order of magnitude in terms of beam loss.

3.3 Conclusion

If the $Q_y = 6.25$ resonance is driven by space charge, its harmonic has to be the same (or a multiple) of the lattice structure one. Since

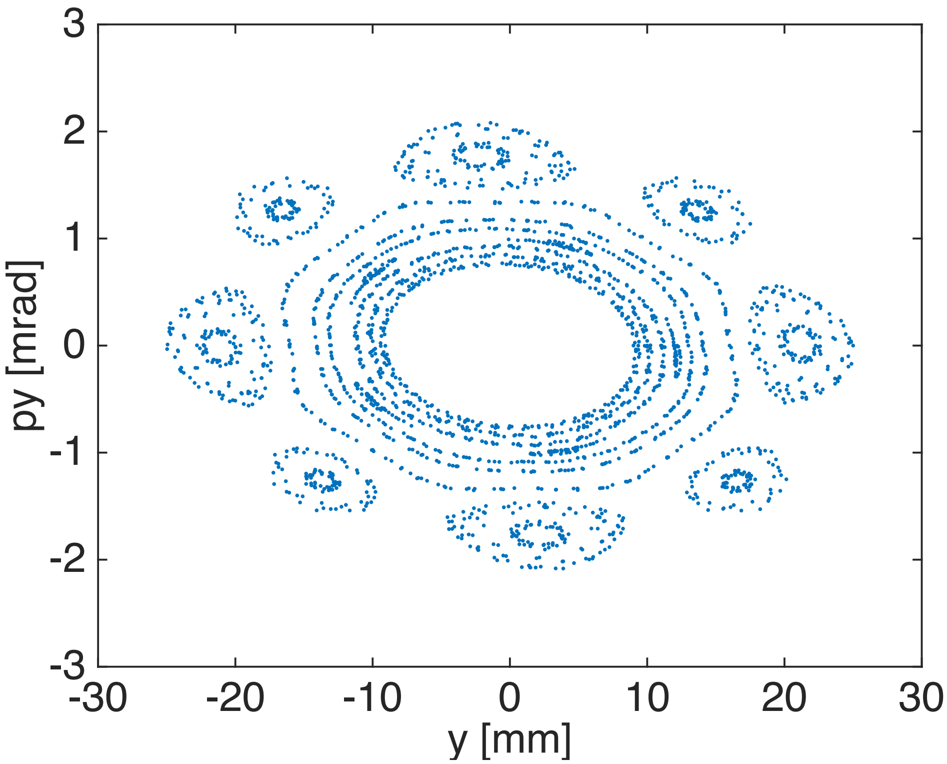

FIGURE 3.13: Vertical phase space for particles at the center of the bunch horizontally and longitudinally, obtained with PTC-ORBIT including indirect space charge effects.

the PS lattice has only the harmonic 50, if the $Q_y = 6.25$ resonance is driven by space charge, it should be an 8^{th} order resonance ($8Q_y = 50$). In which case, the tune per cell is exactly 1 ($8q_y = 1$ for every unit cell "FDDF"), making it a "super-structure" resonance. Space charge simulations showed that in a linear lattice where only space charge is the source of non-linearities, a 8^{th} order topology can be seen in the vertical phase space and it generated a beam-loss of the same order of magnitude as in the measurements. Therefore, we can conclude that $Q_y = 6.25$ is a 8^{th} order super-structure resonance driven by space charge.

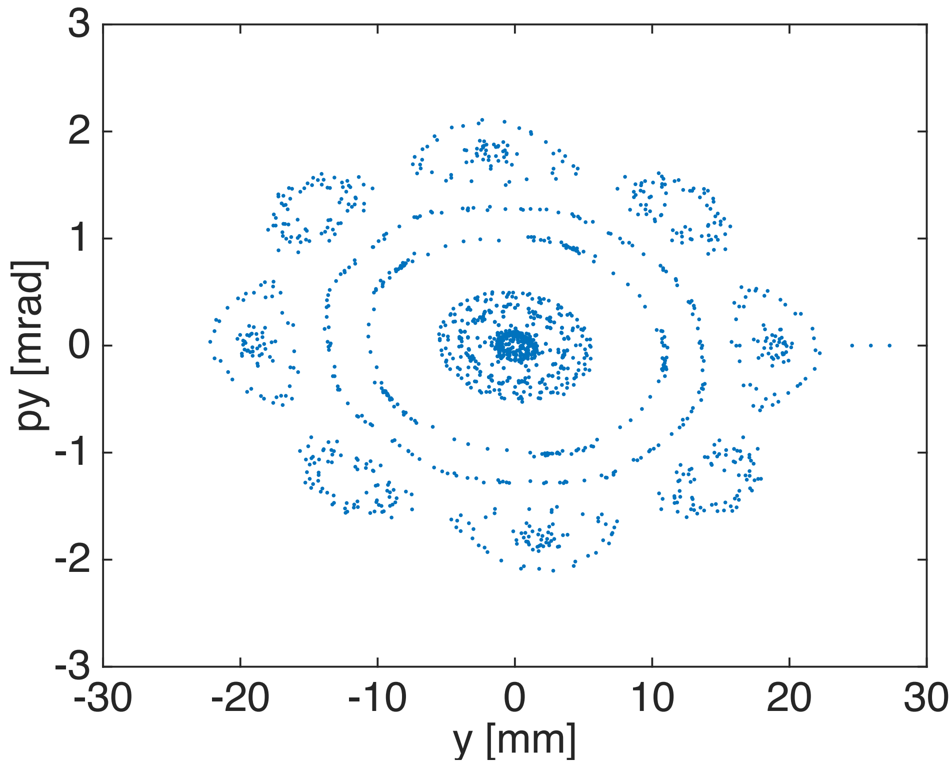

Figure 3.14: Vertical phase space for particles at the center of the bunch horizontally and longitudinally, obtained with IMPACT including indirect space charge effects.

It is interesting to note that this study focused on the vertical resonance line $Q_y = 6.25$ since the beam size is smaller in the vertical plane resulting in a larger vertical space charge detuning and therefore a more strict limitation. The horizontal resonance line is not limiting the performance yet, but it was observed to be harmful to the beam intensity in the study shown in Fig. 2.5, where the crossing of $Q_x = 6.25$ caused significant beam loss. The $Q_x = 6.25$ resonance should also be an 8^{th} order super-structure resonance driven by space charge for the same reasons of symmetry.

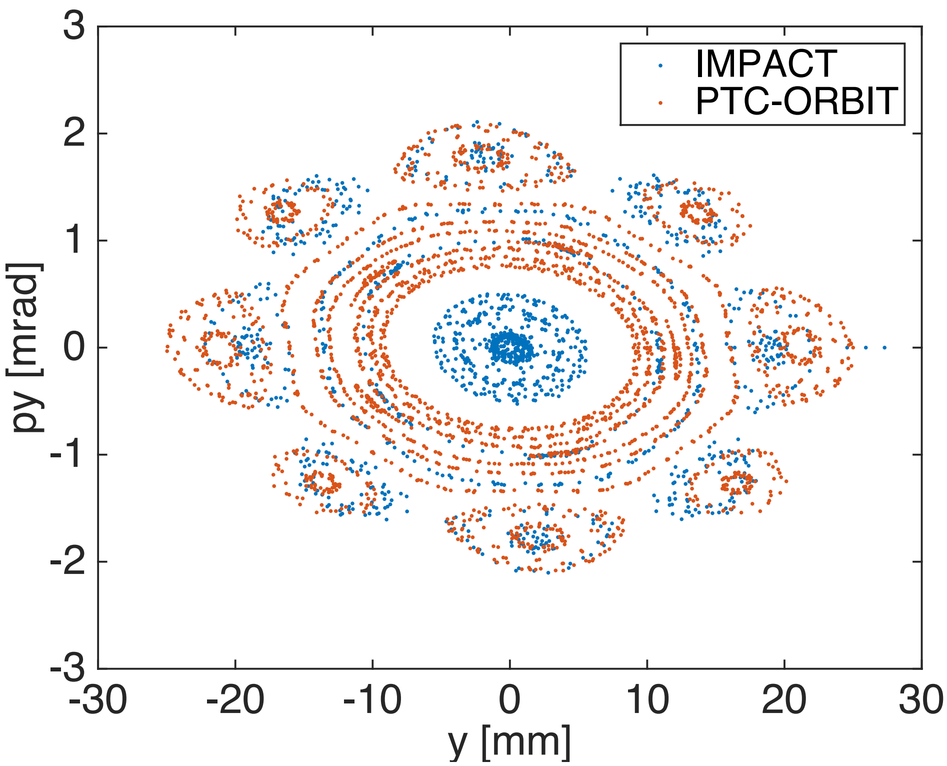

FIGURE 3.15: Vertical phase space for particles at the center of the bunch horizontally and longitudinally, obtained with IMPACT (blue) and PTC-ORBIT (red) including indirect space charge effects.

Chapter 4

Change of tune integers and other possible mitigations

In the previous chapter, we have seen that the $Q_y = 6.25$ resonance is a 8^{th} order super-structure resonance driven by space charge. This resonance is the current limitation for producing higher brightness beams without additional beam loss or emittance growth, since it limits the available resonance-free areas in the tune diagram. It is also important to note that, since its a space charge driven resonance, it becomes stronger when the beam brightness increases.

4.1 Change of tune integers

An idea to mitigate this resonance is to change the betatronic harmonic or in other terms the space charge one, in which case the beam envelope would not have the same harmonic as the structure one. For example, if the vertical tune integer is changed from 6 to 7, the resonance line becomes $8Q_y = 58$ ($4Q_y = 29$), therefore avoiding the structure harmonic 50. Consequently, changing the integer value could be a mitigation of the resonance in order to allow a higher brightness beam. In the case of the PS, the change of the integer is only possible using the pole face windings (PFW) and the figure-eight loop (F8L) [30]. The F8L has the advantage of introducing exclusively a quadrupolar effect and no other magnetic non-linearities, therefore it was chosen to change the integer tune. Its only limitation is that it acts in opposite directions for the two tunes, which means that if the vertical tune is increased by one unit, the horizontal one is reduced by one unit as well, this is due to the geometry of the loop that unbalances the F and D halves of the main magnets.

There are two alternatives to change the integer part of the vertical tune using the F8L, either increasing the vertical tune of one unit (and decreasing the horizontal one), or the opposite. The results of both ways are shown In Tab. 4.1, compared to the machine without any tuning (bare machine). Additionally, one can still tune the machine at low energy using the low-energy quadrupoles (LEQ) and the 4 other circuits of the PFW.

Several relevant values for each optics are given in Table 4.1. First, the current needed in the F8L to change the tune of one unit is roughly 97 A, which is achievable by the existing hardware. The two options are equivalent from the point of view of resonances, the idea is to avoid the $Q_y = 6.25$ line, which is achieved in both case. Scheme 2, where the vertical tune is increased by one unit, seems to be more interesting, particularly for LHC-type beams (small beam size), because

TABLE 4.1: Comparison of relevant parameters for the three different optics

	Bare Machine	Scheme 1	Scheme 2
Q_x	6.21	7.21	5.21
Q_y	6.23	5.23	7.23
F8L [A]	0	-97	97
D_xRMS [m]	3	2.2	4.2
D_xMAX [m]	3.4	3.7	5.2
Average β_x [m]	17.1	15.7	21.9
Average β_y [m]	16.9	29.8	14.7
MAX β_x [m]	22.6	32.2	41.1
MAX β_y [m]	22.5	87.6	22
$\gamma_{transition}$	6.08	7.05	5.12
ΔQ_x	-0.15	-0.15	-0.14
ΔQ_y	-0.19	-0.24	-0.16

the average dispersion is increased by 40 % and the average horizontal beta by 28 %, while the average vertical beta is decreased by only 13 %. Therefore the space charge detuning is lower by roughly 11 % in horizontal and 16 % in vertical. Obviously, the main limitation of such a scheme is the beam size which becomes larger. For example, a beam of $2\,\mu m$ ($1\sigma_{normalized}$) emittance in both planes and $\Delta p/p_{(1\,\sigma)} = 10^{-3}$, the horizontal beam-size is 20 % larger in average. In the case of LHC-type beams, this is an acceptable case since the beam pipe is about 18σ in horizontal and $16\,\sigma$ in vertical (considering the largest beam size, for $2\,\mu m$ emittance and $\Delta p/p_{(1\,\sigma)} = 10^{-3}$). Additionally, Scheme 2 has the advantage of having a smaller mismatch at injection (Table 4.2), which is convenient for testing since the optics of the transfer line between the PS and the PSB is not user-dependent. In Tab. 4.2 the optics functions at the injection point are given as well as an estimation of the increase of the beam size due to the mismatch $\Delta\sigma$. The increase is divided in three components, the increase due to the mismatch in β_x ($\Delta\sigma_{\beta_x}$), the increase due to the mismatch in β_y

($\Delta\sigma_{\beta_y}$) and the increase due to the mismatch in D_x ($\Delta\sigma_{D_x}$). These values were estimated using [25].

Table 4.2: Injection Optics for the three Schemes

	Bare Machine	Scheme 1	Scheme 2
β_x [m]	11.96	9.17	10.36
α_x	-0.1	-0.09	0.02
β_y [m]	22.46	34.6	19.75
α_y	-0.05	0.4	-0.1
D_x [m]	2.55	1.96	3.55
$\Delta\sigma_{\beta_x}$ [%]	-	1	0.6
$\Delta\sigma_{D_x}$ [mm]	-	0.7	0.4
$\Delta\sigma_{\beta_y}$ [%]	-	25	0.4

4.1.1 Simulations with a hypothetical Beam parameters

In order to confirm the mitigation proposed in the previous section with the tune split by 2 integers and motivate an experimental campaign, several simulation studies were carried out. First, a set of simulations was performed using hypothetical beam parameters where the space charge is enhanced in order to have a faster emittance growth rate and therefore faster simulations.

A set of simulations was launched using hypothetical beam parameters using PTC-ORBIT, leading to a vertical tune spread due to space charge of -0.6.

In Fig. 4.1, the simulations show a significant emittance growth in the case of the nominal optics compared to the split integer tune optics, confirming the hypothesis of a structure resonance of harmonic 50 that disappears when the integer changes. These results were an important motivation for the experimental work.

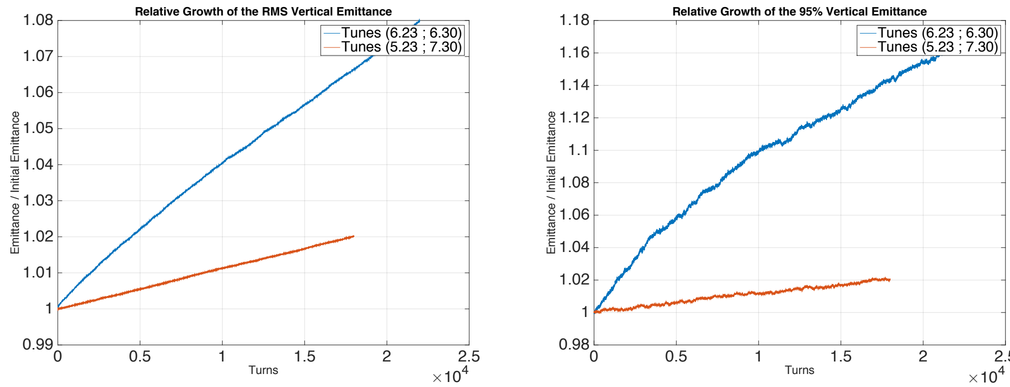

FIGURE 4.1: Relative RMS emittance growth (left) and 95% emittance growth (right), for the nominal optics (blue) and split-tunes optics (red) at a static tune q_y=0.30

4.1.2 Optics Measurements

An optics measurement study was done in the PS in order to verify the change of integer and the new optics functions. The principle of the measurement is to use the closed orbit distortion detected in every pickup and derive the optics given a known phase advance between the pickups [49].

After a series of Machine Development (MD) sessions, the measured optics appeared to be very close to the design one, with less than 20% beta beating. In Fig. 4.2, the measured (in blue) and simulated (in red) β_x (upper left figure), β_y (upper right figure) and D_x (lower figure). This result is a very good indication of the validity of the optics model used and effectiveness of the integer change.

As additional verification of the change of integer, the closed orbit was measured and as it can be seen in Fig. 4.3, there are 5 oscillations in the horizontal plane and 7 in the vertical one, therefore confirming the change of optics to (5 ; 7).

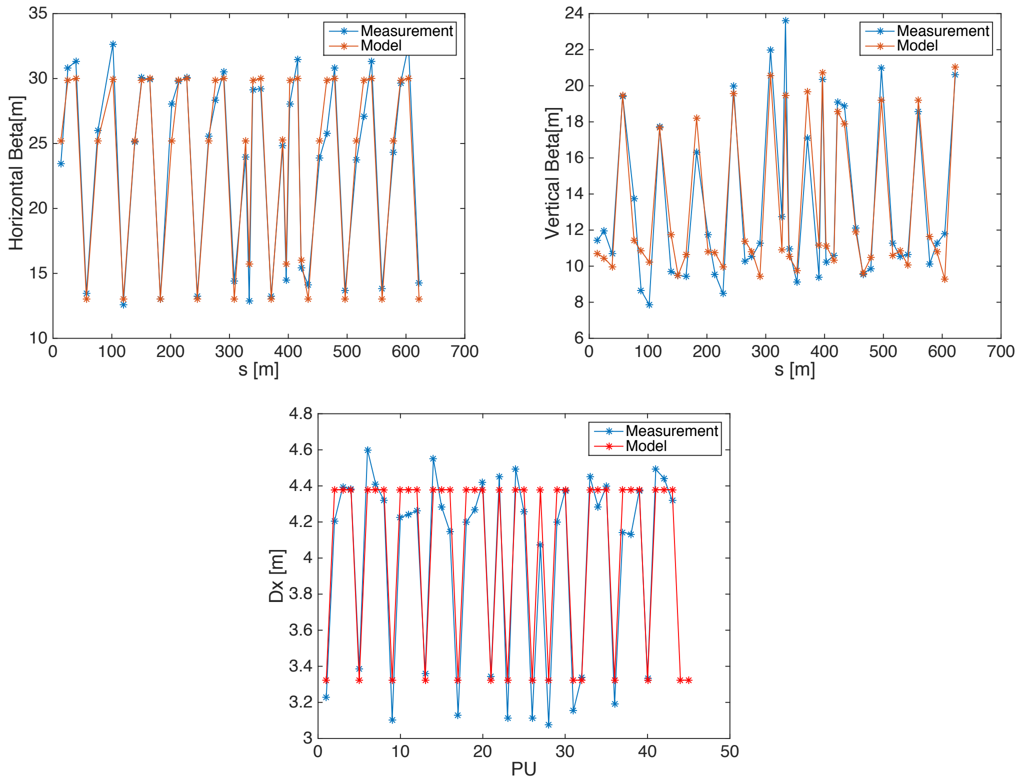

FIGURE 4.2: Measured Optics for the split-tunes scheme. The blue lines are the measured optics and the red ones are the simulated ones. β_x (upper left), β_y (upper right) and D_x (lower).

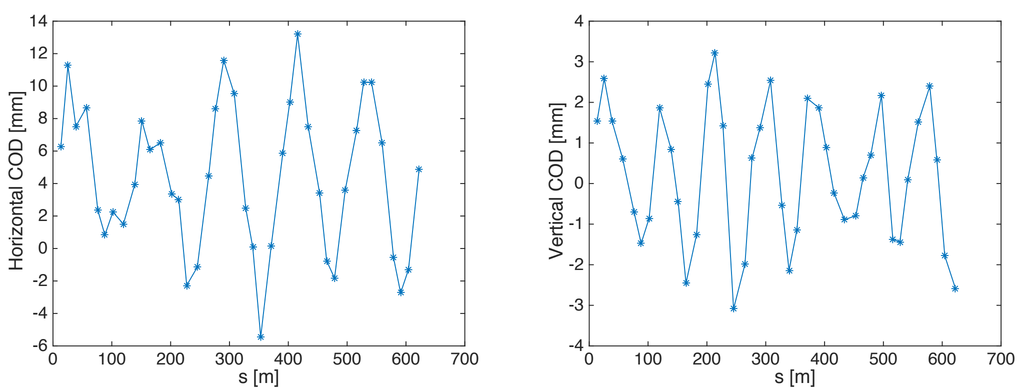

FIGURE 4.3: Measured Horizontal (left) and Vertical (right) closed orbit after change of integer.

4.1.3 Beam Measurements

Several measurement settings were used to show the effect of the 8^{th} order resonance and compare it for the nominal and split-tunes optics cases.

Similar to the measurements of Chap. 4, a tune step was programmed in order to cross the $Q_y = 6.25$ resonance (nominal optics) and $Q_y = 7.25$ (split-tunes optics). For this set of measurements several steps were programmed with several plateau values varying the fractional part from 0.24 to 0.34 as shown in Fig. 4.4.

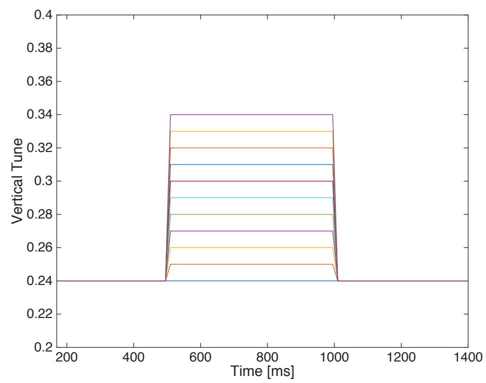

FIGURE 4.4: Vertical Tune step programmed in order to cross the 8^{th} order resonance. The fractional part starts at 0.24 and goes to a plateau value Q then back to 0.24. The plateau value is varied between 0.24 and 0.34.

In the case of the nominal optics, the behavior was similar to the one measured in Chap. 4. Fig. 4.5 shows that the higher the plateau value is, the larger the beam loss is. This is explained by the amount of large amplitude particles crossing the resonance. When the vertical tune is higher, a lower part of the space charge tune-spread necktie overlaps the resonance which means particles with larger amplitude and therefore causing more beam loss.

While in the case of the split-tunes optics (5 ; 7), the beam loss disappeared as seen in Fig. 4.6. The only curve showing significant

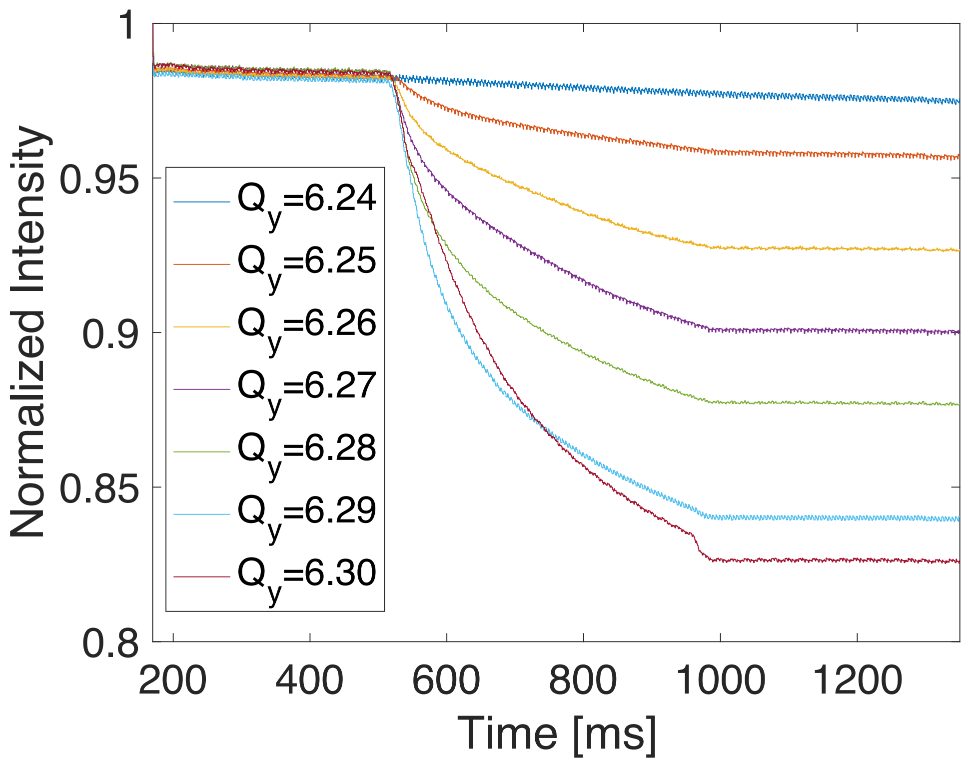

FIGURE 4.5: Relative intensity loss due to resonance crossing for the nominal optics.

losses is the one for $Q_y = 7.34$ as it crosses the 3^{rd} order resonance $3\,Q_y = 22$ which is known to be excited, as seen in Fig. 2.2.

Combining the two figures, we obtain Fig. 4.7 (in this figure the plateau 0.34 was omitted for the split-tunes optics as it is caused by another resonance). The effect of the resonance crossing becomes negligible in the case of the split-tunes optics, this result is extremely interesting as it confirms that the resonance is a structure one (h = 50) that disappears once the harmonic is changed to 58. The change of the integer tune is therefore an efficient mitigation to the $8Q_y = 50$ resonance, consequently allowing for a higher acceptable space charge tune-spread with the same beam loss and emittance growth budgets, which means higher brightness beams. Nevertheless, few issues should

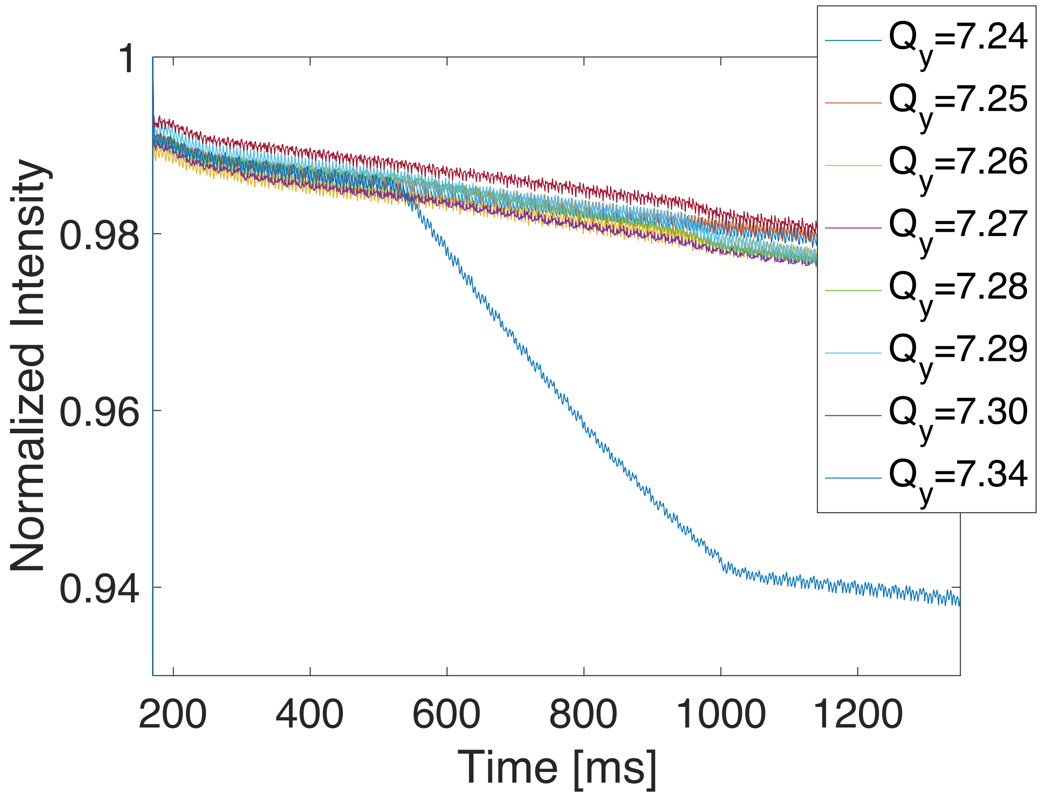

FIGURE 4.6: Relative intensity loss due to resonance crossing for the optics (5;7).

be addressed in order for this scheme to become operational for the LHC-type beams, these issues will be discussed in the following section.

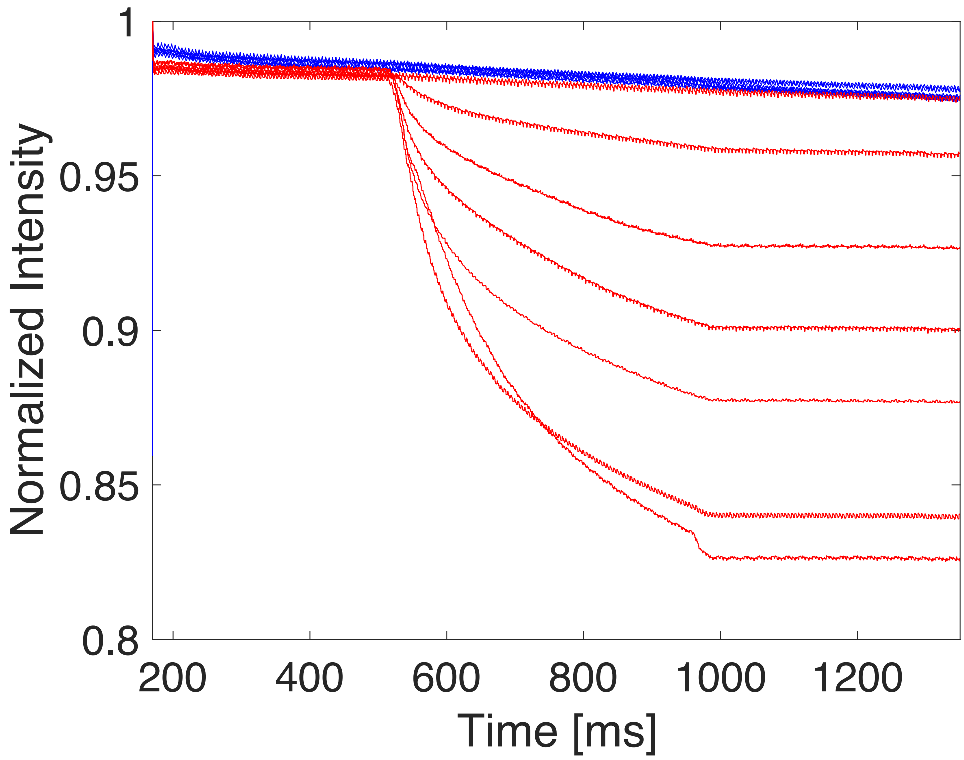

Figure 4.7: Relative intensity loss due to resonance crossing under the nominal optics (red) and split-tunes optics (blue).

4.2 Challenges for an operational split-tunes optics

The change of the integer tune seems to be a very efficient solution in order to avoid the $Q_y = 6.25$ and increase the space charge tune-spread while keeping the emittance growth and beam loss within the allowed budgets. Nevertheless, there are several limitations that should be addressed and mitigated before putting this scheme in operation.

First, the change of integer tune increases the physical beam size, which is acceptable in the case of the LHC-type beams but not for the other users that require a much larger beam. Therefore the use of the new optics should be restricted to the LHC-type beams, which is possible with existing and future hardware. Second, the split-tunes optics affect the transition energy, which impacts all longitudinal gymnastics performed in the PS. It also impacts the transition crossing scheme in terms of betatronic phase and between the quadrupoles used for the $\gamma - jump$ scheme [30] and their strength. A detailed study should be carried out in order to determine the feasibility of all these changes and the compatibility with the nominal transition crossing required for the other users.

As seen in Tab. 4.2, the change of integer tune affects the injection point optics. Currently the transfer line optics between the PSB and the PS cannot be changed from cycle to cycle, which means that matching them to the split-tune optics will affect all other users. This issue will be solved after the Long Shutdown 2, during which the transfer line will be upgraded and one will be able to change its optics from cycle to cycle. During the experimental study of the previous section, Scheme 2 was chosen to minimize the injection mismatch. After the upgrade of the transfer line, Scheme 1 should be a better operational solution than Scheme 2, because Scheme 1 implies the use of a negative current of the F8L. At high energy the required negative current should cancel out with the current intensity used for the working point adjustment. While the Scheme 2 would requires an additional ∼1000 A in the F8L, which cannot be achieved with the current power suppliers.

4.3 Halo cleaning

Currently the LHC beams are injected at the working point (6.23 ; 6.245) and we observe a very small beam loss (3-5%) with almost no emittance growth throughout the injection plateau. The beam profiles seem to be conserved with the exception of a "halo cleaning" in the horizontal plane, where large amplitude particles are lost. The study done in Chap. 2 showed that the beam tune-spread is trapped between the integer and the $Q_y = 6.25$ resonances, the first leading to emittance growth and the latter causing beam loss. Since the working point is 6.245 in the vertical plane, only particles with positive detuning overlap the $Q_y = 6.25$ resonance and are lost. Space charge induces negative detuning, while the positive detuning is caused by the chromaticity $\xi \frac{dp}{p}$, which means that these particles are large amplitude particles in the longitudinal plane (large $\frac{dp}{p}$). The longitudinal distribution isn't significantly correlated to the vertical one (vertical dispersion insignificant), while there is a high correlation in the horizontal one. At large $\frac{dp}{p}$, particles are at large horizontal amplitude ($x = x_0 + D_x\frac{dp}{p}$). Therefore, operating at slightly lower vertical tune than 6.25 helps deplete the horizontal beam tail, and that's what is observed experimentally for the LHC-type beams.

4.4 Resonance compensation

The change of integer tune was shown to be efficient to mitigate the $Q_y = 6.25$ resonance. Once mitigated, the limiting resonances become the $q_y = 0.33$ and $2q_x + q_y = 1$ (q being the fractional part of the tune). These resonances have been shown to be excited in Fig. 2.2 from the recent study [4] and in a previous study in 1987 [50]. These resonances have been proven to be skew sextupolar resonances and they were compensated empirically using 4 skew sextupoles installed in the machine. An experimental study was carried out in order to compensate these resonance using skew sextupoles. The same skew sextupoles were re-installed in the machine but in different sections, because other components are currently installed in the sections where the sextupoles were previously installed.

As shown in Fig. 4.8, 6 tune diagram measurements were performed. The first row of tune diagrams is measured by ramping the horizontal tune and fixing the vertical one, while the second one is measured by ramping the vertical tune and fixing the horizontal one. The two types of diagrams were measured because each direction reveals clearly the opposite resonance, for example a horizontal scan reveals in a very clear way vertical resonances. Three cases are shown, first column is for the bare machine (no multipoles), the second column is with a setting of the skew sextupoles were the $2q_x + q_y = 1$ is compensated. The third column is for a setting where $3q_y$ is compensated. The diagrams show that the resonance compensation has been successful, proving that the resonances are skew sextupolar resonances and they can be compensated using the installed skew sextupoles.

This result shows that combining the change of integer tune and the skew resonance compensation, a quite large resonance-free are could be exploited (potentially double the current one).

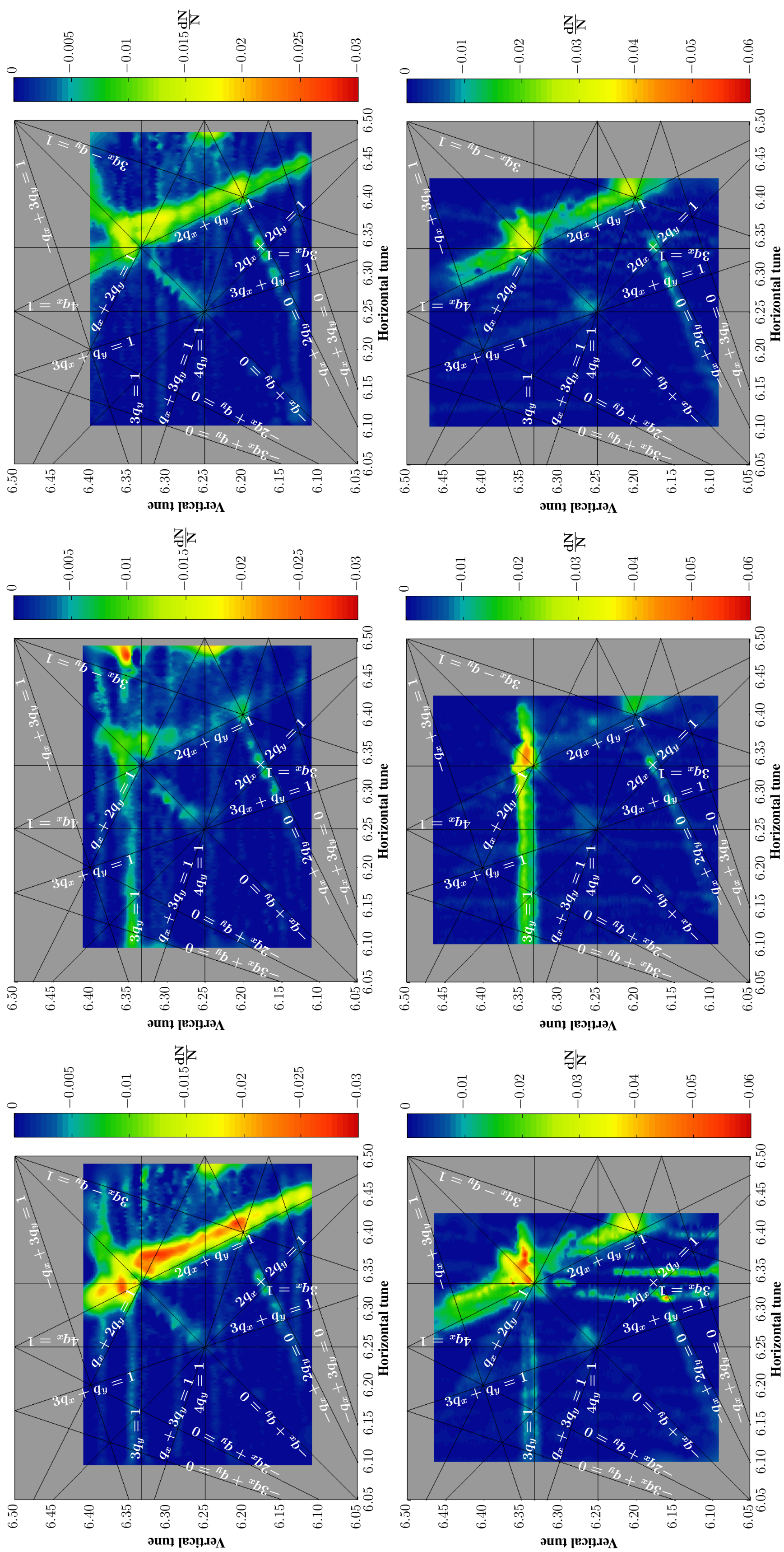

FIGURE 4.8: Tune loss maps for the two different compensation schemes: the first row a horizontal scan of the tune space while the second row is a vertical one. The first column is the scan at 2 GeV, without any compensation. The second column is a scan while compensating the $2q_x + q_y = 19$ resonance, and the third column is a scan while compensating the $3q_y = 19$ resonance.

4.5 Octupolar error measurement using a localized bump

The loss map measurement Fig. 2.2, as well as the chromaticity measurement [32] show that the global octupolar component should be negligible, since none of the octupolar resonances were excited and the tune dependence on $\Delta p/p$ is linear, *i.e.* second and higher order chromaticities are negligible. An additional measurement was performed in order to localize and measure eventual undetected octupolar errors. The measurement idea is to impose a trajectory bump using local dipoles, then measure the tune shift due to the octupole magnetic feed-down. As a proof of principle, a local dipolar bump was induced over 4 sections and reaching its maximum displacement in section 55 where there is an octupole that can be excited. In Fig. 4.9 there are four curves representing the four following cases:

- The bare machine without any additional octupolar excitation
- The octupole of section 55 is powered with +30 A ($k_3 = 37.9\,m^{-3}$).
- The octupole of section 55 is powered with -30 A ($k_3 = -37.9\,m^{-3}$).
- The octupole of section 39 is powered with -30 A. ($k_3 = -37.9\,m^{-3}$)

As expected, Fig. 4.9 shows that with a local bump we are sensitive only to errors within the bump, therefore no dependence appear for the first and last case. On the other hand, an octupolar error in section 55 induced a clear 2^{nd} order dependence between the tune shift and the displacement. By fitting the curves with a polynome, we get that $k_3 = -35.6\,m^{-3}$ for the case where its powered with -30 A, and $k_3 = 37.5\,m^{-3}$ when its powered with 30 A, as predicted by the magnetic model.

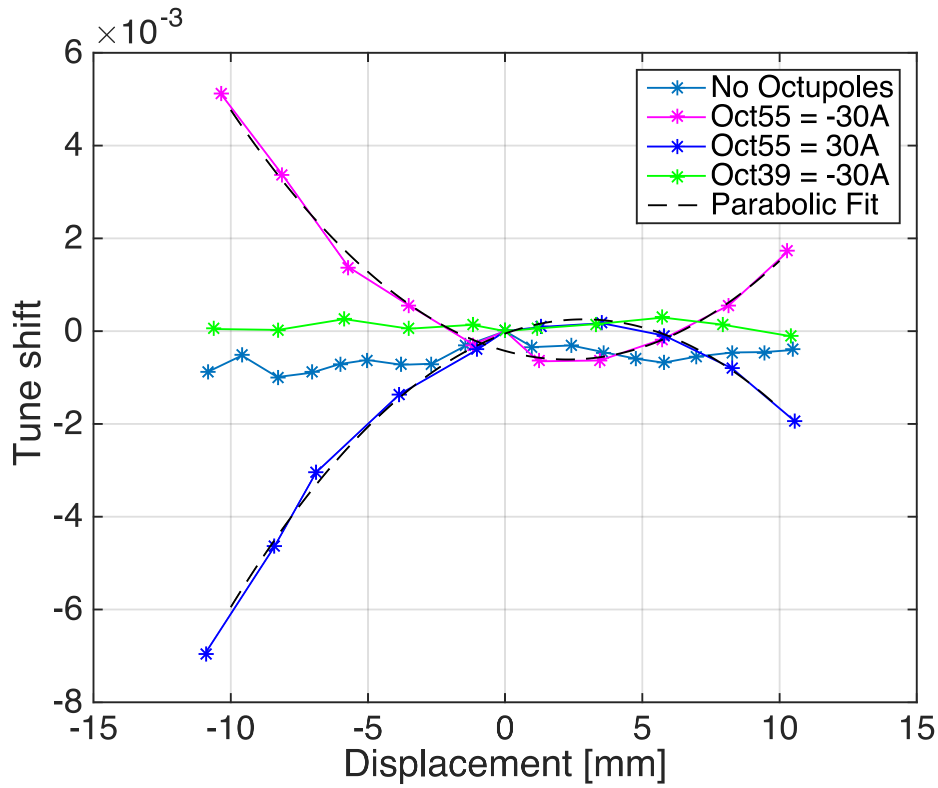

FIGURE 4.9: Tune shift as a function of the the maximum displacement of the trajectory

This agreement confirms the efficiency of the measurement and the absence of octupolar components at injection energy. The absence of octupolar resonance over 4 sections, makes its local presence in 1 section very unlikely. This is another indication that the beam loss caused by $Q_y = 6.25$ resonance are not due to octupolar errors (4^{th} order resonance).

Conclusion & Outlook

In the CERN PS, the production scheme of the LHC beams features a double batch injection, where a first batch of 4 bunches is injected and stored for $1.2\,s$ at $1.4\,\mathrm{GeV}$ kinetic energy, then a second batch of 2 bunches is injected, before the beam go through the RF manipulations and acceleration. Between the 2 injections, and during $1.2\,\mathrm{s}$, the 4 injected bunches are stored and suffer beam loss and emittance growth due to resonance crossings. The beam specifications of the HL-LHC project allocate a maximum beam loss and emittance growth budgets of 5% each, therefore a study of the maximum acceptable space charge tune-spread was carried out in order to determine the maximum tune-spread which respects the allowed budgets. Beam measurements have shown that the maximum beam brightness is ~ 0.3, in order to respect both the beam loss and emittance growth budgets. The measurements of the maximum tune-spread (Fig. 2.6) showed that the beam space charge neck-tie is trapped between two harmful resonances, the $Q_y = 6.0$ and the $Q_y = 6.25$. The choice of working point is the result of a compromise between two effects, the emittance growth due to the resonance crossing of the small amplitude particles overlapping the $Q_y = 6.0$, and the beam loss due to the crossing of the $Q_y = 6.25$ resonance by the large amplitude particles. The higher is the vertical tune, the smaller is the emitance growth caused by the $Q_y = 6.0$ resonance, but the larger is the beam loss due to more particles overlapping the $Q_y = 6.25$ resonance. The lower is the vertical tune, the smaller is the beam loss due to the $Q_y = 6.25$ resonance but the larger is the emittance growth due to more small amplitude particles crossing the $Q_y = 6.0$ resonance. This observation was surprising because in the study of the harmful resonances in the PS, the $Q_y = 6.25$ resonance was not observed as being excited. Since the only difference between the two beam measurements are the beam parameters, and more specifically, the beam brightness, it was thought that the $Q_y = 6.25$ resonance is excited by the beam itself.

The PS lattice structure shows a very strong 50 harmonic, despite of the small perturbations cause by tuning quadrupoles and the difference in length of the straight sections. Given the harmonic 50 of the PS, a space charge induced resonance would very likely be $8Q_y = 50$, which makes it a "super-structure" resonance (the tune is 1 in each of the 50 cells of the PS). Simulations where space charge is the only source of non-linearities showed that the vertical phase space features a clear 8^{th} order resonance topology. Simulations also showed that $Q_y = 6.25$ was sufficient to provoke the same order of magnitude of beam loss as in measurements, without the need of including the magnetic errors and magnet misalignments. The results confirmed the hypothesis of the 8^{th} order resonance and motivated another study which provides a mitigation and additional verification of the initial hypothesis. The proposed mitigation is to change the integer vertical tune to 7, therefore changing the space charge harmonic while keeping the same symmetry of the lattice. Such a modification would make the new resonance line $8Q_y = 58$, which would be a non-structure resonance and therefore it should to be significantly weaker. The measurements and simulations showed a drastic reduction of the beam loss and the resonance strength (Fig. 4.7), confirming the hypothesis and the effectiveness of the proposed mitigation. The main limitation of this mitigation is the increase of the physical beam size, making the solution not compatible with transversely large beams.

To sum up, we can conclude that the $Q_y = 6.25$ resonance is driven by space charge because:

- Simulations, where space charge is the only source of non-linearities, show the effect of the resonance (beam loss and phase space topology).
- Measurements with beams of different brightness show a clear dependence between the resonance strength and the beam brightness.

We can also conclude that the resonance is a super-structure resonance for the following reasons:

- The analysis of the PS lattice shows a very strong harmonic 50, corresponding to $8Q_y = 50$.

- Simulations and measurements show that the resonance disappear when the resonance harmonic (integer) is changed.

Furthermore, the resonance was proven to be an 8^{th} order resonance because:

- Simulations showed that 8 islands structure of the phase space.
- The simulated beam-loss has the same order of magnitude as the measured one, indicating that the 8^{th} order resonance structure is the source of the beam-loss.

All the above confirm that the $Q_y = 6.25$ resonance is a 8^{th} order super-structure resonance driven by space charge.

Further studies and investigations could focus on finding an experimental evidence of the order of the resonance. Several trials were carried out, but due to the nature of the resonance, space charge driven, and the high order, 8^{th} order, the conventional methods were not successful.

This work has discovered and concluded on the nature of the $Q_y = 6.25$ resonance excited by space charge. It is the first experimental observation of such a resonance. The resonance happens to be the consequence and current limitation for higher brightness. An operationally feasible mitigation was proposed for the LHC-type beams, but few challenges remain to be solved in order to operationally implement it.

Acknowledgements

My experience at CERN has been full of ups and downs, moments where things worked exactly the way I wanted and sometime not at all. It is thanks to these “failures” that one appreciats the “sucesses”, and it is during the most difficult moments that you realise and appreciate the support of people around you. Overall, I have very positive and happy memories of the years I spent at CERN and I felt deep sadness when I left CERN. Here is a large group of people who made this journey that amazing and definetly worth taking.

First, I would like to start with my amazing supervisor Simone Gilardoni, who was there for me at every tough moment, professional as well as personal. He challenged me but at the same time defended me. It is well known that employees stay for a boss rather than a Job, and it is 100% true in my case. Thank you Simone for all the help, ideas, the freedom of trying crazy ideas and the support in many situtations.

I want to thank my university supervisor Giuliano Franchetti, for all the help and the freedom of choice he gave me. He heleped me and supported me, even in non-physics related subjects. I want also to thank Prof. Ulrich Ratzinger for his help and support.

I wouldn’t be able to thank Shinji Machida enough in this section, for all the amazing, fruitful and interesting discussions we had, about not only physics but philosophy, psychology...etc. Thank you very much for the help you provided and your deep understanding of space charge induced resonances.

I am extremely thankful to Malte Titze for his help with the German translation of the summary, as I don’t speak German at all. I would like to thank Joschka Wagner and Stefan Sorge for their revision of the summary.

I would also like to thank all my colleagues for their tremendous help in terms of physics but also on the personal level. A special thanks to Alexander Huschauer with who I spent many nights at the CCC. Without the chats and gossiping this PhD would have felt 10 years longer. Cedric Hernalsteens, thanks for all the help when I arrived at CERN, the endless discussions (for example about the coherent-incoherent effects) and all the gossiping obviously.

I would like to thank Elias Metral who supervised my Master thesis and thanks to him I started working at CERN.

A special thanks to Ji Qiang who helped me a lot, providing and adapting his simulation code IMPACT and who hosted me in UC Berkeley for 2 weeks.

I would also like to thank Guido Sterbini, Gianluigi Arduini, Massimo Giovannozzi, Michel Martini, Benoit Salvant, Nicolas Mounet, Nicolo Biancacci and Serena Persichelli.

I am also very grateful to all PS and PSB operators, especially Oliver Hans, Gabriel Metral, Marc Delrieux, Ernesto Ovale, Jean-Michel Nonglaton, Denis Cotte, Piriya Chaichanasiri, Pierre Freyermuth, Jean-charles Dumont, Abdelouahid Akroh, Fabrice Chapuis, and Yu Wu.

Last but definitely not least, I have to thank all my family who supported me (financially and morally) and strongly insisted that I start and finish this PhD. It felt like they wanted it even more than me.

Bibliography

[1] E. Forest, A. Molodozhentsev, A. Shishlo, and J. Holmes. Synopsis of the PTC and ORBIT Integration.

[2] G. Rumolo. LIU baseline for protons. Technical Report Chamonix 2016, CERN, 2016.

[3] H Damerau, A Findlay, S Gilardoni, and S Hancock. RF Manipulations for Higher Brightness LHC-Type Beams. (CERN-ACC-2013-0210):3 p, May 2013. URL https://cds.cern.ch/record/1595719.

[4] A. Huschauer. Working point and resonance studies at the CERN Proton Synchrotron. Master's thesis, Vienna, Tech. U., Sep 2012.

[5] R. Cappi et al. Measurement and Reduction of Transverse Emittance Blow-up Induced by Space Charge Effects. (in Proc. PAC 93, Washington, D.C., USA), 1993.

[6] G. Apollinari, O. Bruning, and L. Rossi. High Luminosity LHC Project Description. Technical Report CERN-ACC-2014-0321, CERN, Geneva, Dec 2014.

[7] H. Damerau et al. LHC Injectors Upgrade, Technical Design Report, Vol. I: Protons. (CERN-ACC-2014-0337), 2014.

[8] G. Franchetti et al. Space charge and octupole driven resonance trapping observed at the cern proton synchrotron. (PHYSICAL REVIEW SPECIAL TOPICS - ACCELERATORS AND BEAMS,VOLUME 6, 124201), 2003.

[9] E. Metral, G. Franchetti, M. Giovannozzi, I. Hofmann, M. Martini, and R. Steerenberg. Observation of octupole driven resonance phenomena with space charge at the cern proton synchrotron. (Nuclear Instruments and Methods in Physics Research A 561, (2006), 257-265), 2006.

[10] G. Franchetti and Ingo Hofmann. Particle trapping by nonlinear resonances and space charge. (Nuclear Instruments and Methods in Physics Research A 561, (2006), 195-202), 2006.

[11] S. Machida. Space-charge-induced resonances in a synchrotron. (Nuclear Instruments and Methods in Physics Research A 384 (1997) 316-321), 1997.

[12] S.Y. Lee, G. Franchetti, I. Hofmann, F. Wang, and L. Yang. Fundamental limit of nonscaling fixed-field alternating gradient accelerators. (New Journal of Physics 8 (2006) 291 and Phys. Rev. Lett. 97, 104801), 2006.

[13] S. Cousineau, S. Y. Lee, J. A. Holmes, V. Danilov, and A. Fedotov. Space charge induced resonance excitation in high intensity rings. (Phys Rev. ST Accel. and Beams 6, 034205), 2003.

[14] P. Freyermuth, D. Cotte, M. Delrieux, H. Genoud, S. Gilardoni, K. Hanke, O. Hans, S. Mataguez, G. Metral, F. Peters,

R. Steerenberg, and B. Vandorpe. Cern proton synchrotron working point matrix for extended pole face winding powering scheme. (CERN-ATS-2010-180), 2010.

[15] Ji Qiang. IMPACT. URL http://amac.lbl.gov/~jiqiang/IMPACT/index.html.

[16] pyORBIT. URL http://code.google.com/p/py-orbit/.

[17] M. Juchno. *Magnetic Model of the CERN Proton Synchrotron*. PhD thesis, EPFL, 2013.

[18] O. Bruning, P. Collier, P. Lebrun, S. Myers, R. Ostojic, J. Poole, and P. Proudlock. *LHC Design Report, Volume I*. CERN, Geneva, 2004.

[19] G. Aad et al. Observation of a New Particle in the Search for the Standard Model Higgs Boson with the ATLAS Detector at the LHC. (Physics Letters B 716, 1, issn: 0370-2693), 2012.

[20] L. Ventura. *Study of longitudinal multibunch instabilities for LHC-type beams at the CERN Proton Synchrotron*. PhD thesis, Sapienza Universita Di Roma, 2013.

[21] E. Shaposhnikova, E. Ciapala, and E. Montesinos. UPGRADE OF THE 200 MHz RF SYSTEM IN THE CERN SPS. Technical Report IPAC2011, MOPC058, CERN, San Sebastian, Spain, 2011.

[22] R. Garoby. Private communication.

[23] S. Gilardoni, G. Arduini, H. Bartosik, E. Benedetto, H. Damerau, V. Forte, M. Giovannozzi, B. Goddard, S. Hancock, K. Hanke, A. Huschauer, M. Kowalska, M. J. McAteer, M. Meddahi, E. Metral, B. Mikulec, Y. Papaphilippou, G. Rumolo, E. Shaposhnikova, G. Sterbini, and R. Wasef. LONG-TERM BEAM LOSSES IN THE CERN INJECTOR CHAIN. Technical Report HB2014, THO1LR01, CERN, East-Lansing, MI, USA, 2014.

[24] S Y Lee. *Accelerator Physics*. third edition (World Scientific 2012), 2012.

[25] A. Chao and M. Tigner. *Handbook of Accelerator Physics and Engineering*. World Scientific, Singapore, 1999.

[26] V. Forte. *Performance of the CERN PSB at 160 MeV with H- charge exchange injection*. PhD thesis, UNIVERSITE BLAISE PASCAL, June 2016.

[27] K. Schindl et al. Space Charge. (CERN/PS 99-012(DI)), 1999.

[28] S. Machida. Space-charge-induced resonances in a synchrotron. (Nuclear Instruments and Methods in Physics Research A 309 (1991) 43), 1991.

[29] S. Sorge, G. Franchetti, and A. Parfenova. Measurement of the acceptance by means of transverse beam excitation with noise. (PHYSICAL REVIEW SPECIAL TOPICS - ACCELERATORS AND BEAMS 14, 052802 (2011)), 2011.

[30] S. Gilardoni et al. *Fifty years of the CERN Proton Synchrotron : Volume 1*. CERN, Geneva, 2011.

[31] S. Gilardoni et al. *Fifty years of the CERN Proton Synchrotron : Volume 2*. CERN, Geneva, 2013.

[32] A. Huschauer. *Beam Dynamics Studies for High-Intensity Beams in the CERN Proton Synchrotron*. PhD thesis, Vienna Tech. U., May 2016.

[33] D. Möhl. Compensation of space charge effects at transition by an asymmetric Q-Jump: a theoretical study. (CERN-ISR/300/GS/69-62), 1969.

[34] S. Aumon. *High Intensity Beam Issues in the CERN Proton Synchrotron*. PhD thesis, EPFL, Lausanne, May 2012.

[35] G. Gelato. Beam current and charge measurements. 1994.

[36] http://http://jeroen.web.cern.ch/jeroen/.

[37] M. Gasior and R. Jones. The principle and first results of betatron tune measurement by direct diode detection. (CERN-LHC-Project-Report-853 (Geneva, Aug. 2005)).

[38] S. Hancock et al. Tomographic Measurements of Longitudinal Phase Space Density. (Computer Physics Communications 121-122, 648, ISSN: 0010-4655), 1999.

[39] V. Kapin and F. Schmidt. MADX-SC Flag Description. (CERN–ACC–NOTE–2013–0036). URL http://frs.web.cern.ch/frs/Source/space_charge/Literature/manuals/MADX-SC.pdf.

[40] MADX Web Page. URL http://mad.web.cern.ch/mad.

[41] H. Grote, F. Schmidt, L. Deniau, and G. Roy. User's Reference Manual. URL http://madx.web.cern.ch/madx/releases/last-dev/madxuguide.pdf.

[42] F. Schmidt, E. Forest, and E. McIntosh. Introduction to the Polymorphic Tracking Code: Fibre Bundles, Polymorphic Taylor Types and "Exact Tracking". URL https://cds.cern.ch/record/573082.

[43] J. Holmes, S. Cousineau, V. Danilov, S. Henderson, A. Shishlo, Y. Sato, W. Chou, L. Michelotti, and F. Ostiguy. ORBIT: Beam Dynamics Calculations for High-Intensity Rings. (in ICFA Beam Dynamics Newsletter No. 30, edited by J. Wei and L. Merminga (2003), p. 100). URL http://icfa-usa.jlab.org/archive/newsletter/icfa_bd_nl_30.pdf.

[44] Frederik Kesting. *Numerical Noise in Particle-in-Cell Tracking - Generation and Propagation*. PhD thesis, Universität Frankfurt, 2017.

[45] F. Kesting and G. Franchetti. Propagation of numerical noise in particle-in-cell tracking. (PHYSICAL REVIEW SPECIAL TOPICS—ACCELERATORS AND BEAMS 18, 114201), 2015.

[46] H. Damerau, A. Funken, R. Garoby, S. Gilardoni, B. Goddard, K. Hanke, A. Lombardi, D. Manglunki, M. Meddahi, B. Mikulec, G. Rumolo, E. Shaposhnikova, M. Vretenar, and J. Coupard. LHC Injectors Upgrade, Technical Design Report, Vol. I: Protons. Technical Report CERN-ACC-2014-0337, CERN, 2014.

[47] http://hilumilhc.web.cern.ch/.

[48] M. Giovannozzi and P. Scaramuzzi. Nonlinear dynamics studies at the CERN Proton Synchrotron: Precise measurements of islands parameters for the novel multi-turn extraction. (CERN-AB-2004-059 EPAC-2004-WEPLT018), 2004.

[49] T. Bach and R. Tomas. Improvements for Optics Measurement and Corrections software. Technical Report CERN-ACC-NOTE-2013-0010, CERN, 2016.

[50] Y. Baconnier. Tune Shifts and Stop Bands at Injection in the CERN Proton Synchrotron. (CERN/PS 87-89(PSR)), 1987.